UNIVERSIDAD AUTÓNOMA DE BAJA CALIFORNIA
FACULTAD DE CIENCIAS MARINAS
INSTITUTO DE INVESTIGACIONES OCEANOLÓGICAS

STUDY OF CRUSTAL DEFORMATION IN THE SOUTHERN GULF OF CALIFORNIA, FROM 2D SEISMIC REFLECTION DATA

Estudio de la deformación de la corteza en la porción sur del Golfo de California, a partir de datos de sísmica de reflexión en 2D

TESIS

QUE PARA CUBRIR PARCIALMENTE LOS REQUISITOS NECESARIOS PARA OBTENER EL GRADO DE

DOCTOR EN CIENCIAS EN OCEANOGRAFÍA COSTERA

PRESENTA

MARC JULIÀ MIRALLES

ENSENADA, BAJA CALIFORNIA, MÉXICO JUNIO 2024

FACULTAD DE CIENCIAS MARINAS
INSTITUTO DE INVESTIGACIONES OCEANOLóGICAS
POSGRADO EN OCEANOGRAFIA COSTERA

STUDY OF CRUSTAL DEFORMATION IN THE SOUTHERN GULF OF CALIFORNIA, FROM 2D SEISMIC REFLECTION DATA

Estudio de la deformación de la corteza en la porción sur del Golfo de California, a partir de datos de sísmica de reflexión en 2D

T E S I S
QUE PARA CUBRIR PARCIALMENTE LOS REQUISITOS NECESARIOS PARA OBTENER EL GRADO DE

DOCTOR EN CIENCIAS EN OCEANOGRAFÍA COSTERA

PRESENTA

MARC JULIÀ MIRALLES

Aprobada por:

Dr. Usama Ismael Yarbuh Lugo
Director de tesis

Dra. Raquel Negrete Aranda
Codirectora de tesis

Dr. Ronald M. Spelz Madero
Sinodal

Dr. Juan Contreras Pérez
Sinodal

Dr. Antonio González Fernández
Sinodal

Dr. Robert Zierengberg
Sinodal externo

Asunto: Voto aprobatorio sobre trabajo
de tesis de grado de Doctorado

Dra. Ivone Giffard Mena
Coordinadora de Investigación y
Posgrado, F.C.M.
Presente

Estimada Dra. Giffard

Me dirijo a usted en mi calidad de **Director de Tesis** encargado de revisar la tesis de Doctorado presentada por el estudiante **Marc Julia Miralles,** como parte de los requisitos para obtener el grado de **Doctor en Ciencias** en Oceanografía Costera.

Tras llevar a cabo una revisión minuciosa y exhaustiva del trabajo mencionado, es mi deber informarle que he emitido mi **voto Aprobatorio** sobre la tesis titulada:

Estudio de la deformación de la corteza en la porción sur del Golfo de California, a partir de datos de sísmica de reflexión en 2D.

He realizado esta revisión con el compromiso de asegurar que el trabajo cumple con los estándares de calidad y excelencia académica requeridos por nuestro programa de posgrado. Después de un análisis detenido, he llegado a la conclusión de que el trabajo de tesis satisface plenamente estos criterios y representa una contribución valiosa al campo de la Oceanografía Costera.

El trabajo exhibe una sólida base teórica, una metodología rigurosa y una presentación coherente de los hallazgos. Las referencias bibliográficas están actualizadas y pertinentes, y las figuras y tablas son claras y respaldan eficazmente los argumentos del texto. La sección de conclusiones proporciona un resumen sólido de los resultados y sus implicaciones, la referencias y citas están actualizadas y son pertinentes.

Ensenada, B. C., a 17 de junio de 2024

A t e n t a m e n t e,

Dr. Usama Ismael Yarbuh Lugo
Director de tesis

c.c.p. Expediente

Asunto: Voto aprobatorio sobre trabajo
de tesis de grado de Doctorado

Dra. Ivone Giffard Mena
Coordinadora de Investigación y
Posgrado, F.C.M.
Presente

Estimada Dra. Giffard:

Me dirijo a usted en mi calidad de **Co-Directora de Tesis** encargada de revisar la tesis de Doctorado presentada por el estudiante **Marc Julia Miralles,** como parte de los requisitos para obtener el grado de **Doctor en Ciencias** en Oceanografía Costera.

Tras llevar a cabo una revisión minuciosa y exhaustiva del trabajo mencionado, es mi deber informarle que he emitido mi **voto Aprobatorio** sobre la tesis titulada:

Estudio de la deformación de la corteza en la porción sur del Golfo de California, a partir de datos de sísmica de reflexión en 2D.

He realizado esta revisión con el compromiso de asegurar que el trabajo cumple con los estándares de calidad y excelencia académica requeridos por nuestro programa de posgrado. Después de un análisis detenido, he llegado a la conclusión de que el trabajo de tesis satisface plenamente estos criterios y representa una contribución valiosa al campo de la Oceanografía Costera.

El trabajo exhibe una sólida base teórica, una metodología rigurosa y una presentación coherente de los hallazgos. Las referencias bibliográficas están actualizadas y pertinentes, y las figuras y tablas son claras y respaldan eficazmente los argumentos del texto. La sección de conclusiones proporciona un resumen sólido de los resultados y sus implicaciones, la referencias y citas están actualizadas y son pertinentes.

Ensenada, B. C., a 17 de junio de 2024

A t e n t a m e n t e,

Dra. Raquel Negrete Aranda
Co-Director de tesis

c.c.p. Expediente

Asunto: Voto aprobatorio sobre trabajo
de tesis de grado de Doctorado

Dra. Ivone Giffard Mena
Coordinadora de Investigación y
Posgrado, F.C.M.
Presente

Estimada Dra. Giffard:

Me dirijo a usted en mi calidad de **Sinodal** encargado de revisar la tesis de Doctorado presentada por el estudiante **Marc Julia Miralles,** como parte de los requisitos para obtener el grado de **Doctor en Ciencias** en Oceanografía Costera.

Tras llevar a cabo una revisión minuciosa y exhaustiva del trabajo mencionado, es mi deber informarle que he emitido mi **voto Aprobatorio** sobre la tesis titulada:

Estudio de la deformación de la corteza en la porción sur del Golfo de California, a partir de datos de sísmica de reflexión en 2D.

He realizado esta revisión con el compromiso de asegurar que el trabajo cumple con los estándares de calidad y excelencia académica requeridos por nuestro programa de posgrado. Después de un análisis detenido, he llegado a la conclusión de que el trabajo de tesis satisface plenamente estos criterios y representa una contribución valiosa al campo de la Oceanografía Costera.

El trabajo exhibe una sólida base teórica, una metodología rigurosa y una presentación coherente de los hallazgos. Las referencias bibliográficas están actualizadas y pertinentes, y las figuras y tablas son claras y respaldan eficazmente los argumentos del texto. La sección de conclusiones proporciona un resumen sólido de los resultados y sus implicaciones, la referencias y citas están actualizadas y son pertinentes.

Ensenada, B. C., a 17 de junio de 2024

A t e n t a m e n t e,

Dr. Ronald M. Spelz Madero
Sinodal

c.c.p. Expediente

Asunto: Voto aprobatorio sobre trabajo
de tesis de grado de Doctorado

Dra. Ivone Giffard Mena
Coordinadora de Investigación y
Posgrado, F.C.M.
Presente

Estimada Dra. Giffard:

Me dirijo a usted en mi calidad de **Sinodal** encargado de revisar la tesis de Doctorado presentada por el estudiante **Marc Julia Miralles,** como parte de los requisitos para obtener el grado de **Doctor en Ciencias** en Oceanografía Costera.

Tras llevar a cabo una revisión minuciosa y exhaustiva del trabajo mencionado, es mi deber informarle que he emitido mi **voto Aprobatorio** sobre la tesis titulada:

Estudio de la deformación de la corteza en la porción sur del Golfo de California, a partir de datos de sísmica de reflexión en 2D.

He realizado esta revisión con el compromiso de asegurar que el trabajo cumple con los estándares de calidad y excelencia académica requeridos por nuestro programa de posgrado. Después de un análisis detenido, he llegado a la conclusión de que el trabajo de tesis satisface plenamente estos criterios y representa una contribución valiosa al campo de la Oceanografía Costera.

El trabajo exhibe una sólida base teórica, una metodología rigurosa y una presentación coherente de los hallazgos. Las referencias bibliográficas están actualizadas y pertinentes, y las figuras y tablas son claras y respaldan eficazmente los argumentos del texto. La sección de conclusiones proporciona un resumen sólido de los resultados y sus implicaciones, la referencias y citas están actualizadas y son pertinentes.

Ensenada, B. C., a 17 de junio de 2024

A t e n t a m e n t e,

Dr. Juan Contreras Pérez
Sinodal

c.c.p. Expediente

Asunto: Voto aprobatorio sobre trabajo
de tesis de grado de Doctorado

Dra. Ivone Giffard Mena
Coordinadora de Investigación y
Posgrado, F.C.M.
Presente

Estimada Dra. Giffard:

Me dirijo a usted en mi calidad de **Sinodal** encargado de revisar la tesis de Doctorado presentada por el estudiante **Marc Julia Miralles,** como parte de los requisitos para obtener el grado de **Doctor en Ciencias** en Oceanografía Costera.

Tras llevar a cabo una revisión minuciosa y exhaustiva del trabajo mencionado, es mi deber informarle que he emitido mi **voto Aprobatorio** sobre la tesis titulada:

Estudio de la deformación de la corteza en la porción sur del Golfo de California, a partir de datos de sísmica de reflexión en 2D.

He realizado esta revisión con el compromiso de asegurar que el trabajo cumple con los estándares de calidad y excelencia académica requeridos por nuestro programa de posgrado. Después de un análisis detenido, he llegado a la conclusión de que el trabajo de tesis satisface plenamente estos criterios y representa una contribución valiosa al campo de la Oceanografía Costera.

El trabajo exhibe una sólida base teórica, una metodología rigurosa y una presentación coherente de los hallazgos. Las referencias bibliográficas están actualizadas y pertinentes, y las figuras y tablas son claras y respaldan eficazmente los argumentos del texto. La sección de conclusiones proporciona un resumen sólido de los resultados y sus implicaciones, la referencias y citas están actualizadas y son pertinentes.

Ensenada, B. C., a 17 de junio de 2024

A t e n t a m e n t e,

Dr. Antonio González Fernández
Sinodal

c.c.p. Expediente

Abstract

In this study, we integrate a regional geological framework of the southern part of the Gulf of California (GC) to advance the current knowledge about the lithospheric opening process, as well as to understand crustal deformation, magmatism, and associated venting of geothermal fluids. This approach was carried out using 2D multi-channel seismic reflection data collected in 2006 throughout the Carmen and Farallon Basins aboard the R/V Francisco de Ulloa during a collaborative effort involving Centro de Investigación Científica y de Educación Superior de Ensenada, Baja California (CICESE), and Scripps Institution of Oceanography at the University of California, San Diego (UCSD). Our results provide new insights into the tectonic evolution of the Carmen Basin (CB) in the southern Gulf of California (GC) from high-resolution bathymetry and two-dimensional seismic reflection data. Our goal is to document the seafloor morphology and subsurface acoustic characteristics to understand the structure and crustal lithology across the CB. We identify three sub-basins with distinct geometries and evolutionary histories, with basement structures displaying a strong affinity with highly reflective, sigmoidal-shaped layers and the emplacement of high-amplitude tabular material underlying sediments with varying stratigraphic thicknesses. From the extent of new oceanic crust accreted along the CB, we estimate the age of the basin using a seafloor spreading rate of 52 mm/yr, which is the average velocity of the relative plate motion between the Baja California microplate and the North American plate, as documented by previous authors. The southern and central sub-basins of the CB are mainly abandoned, while the northernmost is currently the locus of seafloor spreading. This is evidenced by the juxtaposition of oceanic crust younger than ~1.9

Ma against older oceanic crust correlating in age with the adjacent Guaymas (6.1 Ma) and Farallon (4.2 Ma) basins to the northeast and southwest, respectively. We propose that mantle upwelling beneath the CB is a northward continuation of the East Pacific Rise, resulting in a fast-evolving system with sharp variations in strain localization within the seafloor spreading centers of the CB. The southern part of the GC is characterized by deep-water, narrow, sediment-starved basins developed on transitional and oceanic crust. We propose that as the lithosphere thins, decompression melting of underlying asthenosphere leads to elevated heat-flow and lithospheric break up, facilitating volcanic activity via dynamic mantle upwelling. Assessing the thermal state of the Baja California peninsula, particularly the GC, is strategically of importance for Mexico due to significant geothermal anomalies. The crustal thinning associated with the GC opening provides favorable conditions for geothermal system development. High-resolution seismic data reveal magmatic intrusions and hydrothermal circulation within the Farallon Basin, highlighting its geothermal potential. Magmatic bodies such as sills, specific to the oceanic crust, along with the active axial graben and abandoned spreading centers. This is indicative of a well-developed oceanic basin, with dual depocenters and cross basin faults that reveals a transtensional deformation. The Farallon Basin features distinct transitions between continental and oceanic crust, marked by varying seismic characteristics that signify a continental-oceanic transition.

Keywords: High-resolution bathymetry, Seismic reflection profiles, Basin structure, Crustal lithology, Fault kinematics.

Resumen

En este estudio, integramos un marco geológico regional de la parte sur del Golfo de California (GC) para proporcionar información al conocimiento actual sobre el proceso de apertura litosférica, así como para entender la deformación de la corteza y el magmatismo asociado con la formación de fluidos geotérmicos. Este enfoque se llevó a cabo utilizando datos de reflexión sísmica multicanal 2D recogidos en 2006 a lo largo de la Cuenca Carmen y la Cuenca Farallón a bordo del R/V Francisco de Ulloa durante un esfuerzo de colaboración entre el Centro de Investigación Científica y de Educación Superior de Ensenada, Baja California (CICESE), y la Institución de Oceanografía Scripps de la Universidad de California, San Diego (UCSD). Ofrecemos una nueva perspectiva sobre la evolución tectónica de la Cuenca Carmen (CB) en el sur del Golfo de California (GC) a partir de batimetría de alta resolución y datos de reflexión sísmica bidimensional. Nuestro objetivo es documentar la morfología del fondo marino y las características acústicas del subsuelo para entender la estructura y la litología cortical a través de la CB. Identificamos tres subcuencas con geometrías e historias evolutivas distintas, con estructuras de basamento que muestran una fuerte afinidad con capas sigmoides altamente reflectantes y la colocación de material tabular de alta amplitud subyacente a sedimentos con espesores estratigráficos variables. A partir de la extensión de la nueva corteza oceánica acrecida a lo largo de la CB, estimamos la edad de la cuenca utilizando una tasa de expansión del fondo marino de 52 mm/año, que es la velocidad promedio del movimiento relativo de placas entre la microplaca de Baja California y la placa Norteamericana, como ha sido documentado por autores previos. Las subcuencas sur y central de la CB están principalmente abandonadas, mientras que la del norte es actualmente el lugar de la expansión del fondo marino. Esto se evidencia por la yuxtaposición de corteza oceánica más joven que

~1.9 Ma contra corteza oceánica más antigua, correlacionando en edad con las cuencas adyacentes de Guaymas y Farallón al noreste y suroeste, respectivamente. Proponemos que la surgencia del manto debajo de la CB es una continuación hacia el norte de la Elevación del Pacífico Oriental, resultando en un sistema de rápida evolución con variaciones abruptas en la localización del esfuerzo dentro de los centros de expansión del fondo marino de la CB. La parte sur del GC se caracteriza por cuencas estrechas, de aguas profundas y pobres en sedimentos, desarrolladas sobre corteza transicional y oceánica. A medida que la litosfera se adelgaza, la disminución de la presión en la astenosfera subyacente induce la fusión parcial del manto, lo que conduce a un elevado flujo de calor y la ruptura litosférica, facilitando la actividad volcánica a través de la surgencia dinámica del manto. Evaluar el estado térmico de la península de Baja California, particularmente el GC, es estratégicamente importante para México debido a las significativas anomalías geotérmicas. El adelgazamiento cortical asociado con la apertura del GC proporciona condiciones favorables para el desarrollo de sistemas geotérmicos. Datos sísmicos de alta resolución revelan intrusiones magmáticas y circulación hidrotermal dentro de la Cuenca de Farallón, destacando su potencial geotérmico. Cuerpos magmáticos como los *sills*, específicos de la corteza oceánica, junto con el graben axial activo y los centros de expansión abandonados. Esto es indicativo de una cuenca oceánica bien desarrollada, con dos depocentros y fallas transversales que revelan una deformación transtensional. La Cuenca de Farallón presenta transiciones distintivas entre la corteza continental y oceánica, marcadas por características sísmicas variables que significan una transición continental-oceánica.

Palabras clave: Batimetría de alta resolución, Perfiles de reflexión sísmica, Estructura de cuencas, Litología de la corteza, Cinemática de fallas.

Dedication

This work is dedicated to…

the memory of my father Ignacio González Rodríguez

my mother Anna Julià Miralles

my grandfather Salvador Julià Forgas

Acknowledgements

I am very grateful to Universidad Autónoma de Baja California (UABC) and the Facultad de Ciencias Marina (FCCM) for accepting me into the doctoral program in Coastal Oceanography. Thank you for this amazing opportunity.

I am profoundly grateful to my advisor, Dr. Usama Ismael Yarbuh, for his invaluable guidance and support throughout my doctoral research, as well as my thesis committee members Raquel Negrete Aranda, Ronald Michael Spelz Madero, Juan Contreras Pérez, Antonio González Fernández, and Robert Zierenberg for their support and advice throughout my doctorate.

I want to thank CONAHCYT for providing me with the scholarship No. 1011828 for my Ph.D. project. Additional funding was received from CONAHCYT project No. 319430 awarded to Ismael Yarbuh, and UABC project No. 401/1/C/13/23 awarded to Ronald M. Spelz.

I appreciate the Schmidt Ocean Institute and the *R/V Falkor* crew, especially Lead Tech John Fulmer and MTs Veit Huehnerbach and Kaarel Kaspar Rais, for their support during expedition FK210922 (https://schmidtocean.org/cruise/interdisciplinary-investigation-of-the-pescadero-basin/).

My gratitude goes to Isabela Macias, Juan Manual Wagner, for their contributions to seismic and illustration software management. I am also grateful to Jared Kluesner for his valuable suggestions that improved the scientific manuscript.

Table of Contents

ABSTRACT **I**

DEDICATION **V**

ACKNOWLEDGEMENTS **VI**

LIST OF FIGURES **IX**

LIST OF TABLES **XVII**

I. INTRODUCTION **1**

I.1. Crustal deformation and development of marine basins **1**

I.2. Geologic background of the Gulf of California **5**

I.3. OBJECTIVES **9**
I.3.1. General Objective 9
I.3.2. Specific Objectives 9

I.4. METHODOLOGY **10**

I.4.1. Multichannel seismic reflection data processing **10**

II. STRAIN LOCALIZATION INSTABILITIES AND THE GENESIS OF MULTIPLE AXES OF SEAFLOOR SPREADING IN THE CARMEN BASIN, SOUTHERN GULF OF CALIFORNIA **20**

II.1. Introduction **20**

II.2. Tectonic evolution of the Gulf of California **24**

II.3. Methods **25**

II.4. Results **27**
II.4.1. Geomorphology and 2D architecture of the Carmen Basin 27
II.4.2. Seismic interpretation of the Carmen Basin 31

II.5. Discussion **41**
II.5.1. Geometry and timing of rifting in the Carmen Basin 41
II.5.2. Crustal lithology and the transition from old to young oceanic crust 45

II.5.3. Kinematics of transform faults and spreading center instabilities in the Carmen basin 48

II.6. Conclusions **51**

III. CRUSTAL STRUCTURE AND TECTONIC HISTORY OF FARALLON BASIN, SOUTHERN GULF OF CALIFORNIA **54**

III.1. Introduction **54**

III.2. Geological setting **59**

III.3. Methodology **60**
III.3.1. Seismic Data processing 60
III.3.2. Seismic Interpretation 60

III.4. Results and discussion **61**
III.4.1. Geomorphology and 2D architecture of Farallon Basin 61
III.4.2. Seismic interpretation of the Farallon Basin 64
III.4.3. Rifted Margins and Continent-Ocean transitions 77
III.4.4. Comparative analysis of basin geomorphology in the southern Gulf of California 79

III. 5. Conclusions **81**

REFERENCES **83**

List of figures

Figs		Page
1	a) Conceptual model showing the evolution of the rift–drift basin suite in terms of increasing stretch factor and extensional strain rate. b) Models of strain geometry in rifts. (a) Pure shear geometry features an upper brittle layer over a lower ductile layer, creating a symmetrical lithospheric cross-section. (b) Simple shear geometry involves a low-angle detachment fault that divides the lithosphere into an upper plate (hanging wall) and a lower plate (footwall). (c) Hybrid model combines simple shear in the upper crust, using listric or planar faults, with pure shear in the ductile lower crust and mantle lithosphere. From Allen and Allen (2013).	**2**
2	General characteristics of a pull-apart basin in a dextral side-stepping fault system. The pull-apart basin is defined to develop in pure strike-slip when $\alpha = 0^{\circ}$ and in transtension when $0^{\circ} < \alpha \leq 45^{\circ}$. From Wu et al., (2009).	**3**
3	Schematic model (plan view) of the basin geometries observed in extensional systems. The geometries of the strike-slip fault traces are shown with black lines in each of the panels. The areas colored in grayscale indicate the increase in depth as the fault traces overlap (darker tones, greater depth). The arrows indicate the direction of shearing. (Adapted from Van Wijk, 2017; modified from Mann, 1983).	**4**
4	Regional tectonic map of the Gulf of California (GC). Abbreviations: EPR = East Pacific Rise; TF = Tosco fault; SM-SLF = Santa Margarita-San L´azaro faults, AF = Abreojos fault; GN = Guerrero Negro fault; OL = Ojo de Liebre fault; C = Cedros fault; SC-SI = Santa Catalina-San Isidro faults. Modified from Ramírez-Zerpa et al. (2022).	**6**
5	**a)** Schematic cross section of the paleotrench illustrating the slab break-off process under Baja California. The diagrams show: A) An active subduction setting. B) The formation of a slab window after subduction ends, transitioning to a transform boundary where the upper part of the slab resists subduction while the lower end is pulled down. C) The lower slab continues descending until the slab stretches, deforms, and finally breaks off, sinking into the mantle. **b)** A), B), C) Cartoon illustrating the kinematic model for shearing around the Baja California microplate represents the single-phase development of two	**8**

deformation zones simultaneously, since ~12 Ma Modified from Fletcher et al. (2007).

6 Regional tectonic map of the Carmen Basin and Farallon Basin, with labeled master transform faults (black). Multichannel seismic profiles are indicated by yellow lines. Base map sourced from GeoMapApp (http://www.geomapapp.org). **9**

7 Pre-stacking processing transformed data from SEG-Y to SU format for Seismic Unix compatibility. Of the 52 recorded traces, 48 data channels were retained, and 4 were discarded.. a) The seismic reflection profile initially showed chaotic amplitude and frequency distributions. b) Spectral analysis identified coherent reflection energy within 30-35 Hz and 135-145 Hz. Noisy frequencies were discarded. c) The f-k filter removed linear trend coherent noise, enhancing shallow reflections. d) Spherical Divergence correction mitigated amplitude loss, applying an initial velocity correction of 1500 m/s. Deconvolution improved temporal resolution by isolating signal components. Selective deconvolution eliminated source reverberations while retaining multiples due to their minimal interference with the main signal. **14**

8 Stacking processing enhances signal quality by summing traces with the same reflection point, attenuating non-coherent noise and significant portions of coherent noise, such as multiples. a) Traces are grouped by CDPs, representing the vertical projection of the CMP. Summing these traces improves the signal-to-noise ratio. b) Velocity analysis, using the semblance spectrum method, identifies subsurface velocities for NMO correction. c) NMO correction aligns traces horizontally, making it easier to combine traces within the same CDP and reducing multiple interference. The stacking process sums traces to amplify coherent signals, yielding the initial seismic section with zero offset reflectors. **16**

9 Post-stacking processing represents the final phase of data processing, primarily centered on migration. a) Migration effects include increased horizon dip, shortened length, and upward movement opposite to the dip, as well as syncline narrowing and diffraction hyperbola collapse. Typically, migration uses velocities approximately 10% lower than NMO velocities to avoid over-migration artifacts. b) Vertical resolution is calculated using R=(T/4)*V, while horizontal resolution is defined by the Fresnel Zone formula. c) After processing, seismic interpretation analyzes reflectors' continuity and geometry, identifying features like faults, folds, and sedimentary sequences. Horizontal distance conversion from CDP to meters is based on 6.25 meters per CDP. **19**

10 Regional Tectonic map of the southern Gulf of California showing plate motion (black arrows), transform fault system (black lines), pull-apart basins, and spreading centers (red lines). The Carmen Basin is indicated by the black box (Figure 2). The location of the paleo-trench and the partially subducted Magdalena microplate derived from the Farallon plate is marked by a black dashed line along the western margin of the Baja peninsula. The abbreviation EPR is used for the East Pacific Rise. Base map sourced from GeoMapApp (http://www.geomapapp.org). **21**

11 a) Regional tectonic map of the Carmen Basin (CB), with labeled master transform faults (black). Multichannel seismic profiles are indicated by yellow lines. The black box corresponds to the CB shown in Figure 3. Base map sourced from GeoMapApp (http://www.geomapapp.org). b), c), d, 2D multichannel seismic reflection data across the CB. Seismic lines are divided by vertical black lines corresponding to Figures 4-9. **23**

12 a) Structural map of the Carmen Basin (CB) illustrating the two-dimensional architecture and geometry. High-resolution (40-m) bathymetry is overlaid on faded Global Multi-Resolution Topography (GMRT) bathymetry. The map reveals a series of depocenters within the CB, with increasing depth from south to north. These sub-basins are bounded by two master strike-slip transform faults (red lines), connected by an array of cross-basin faults (yellow lines). The current seafloor-spreading center is located in the northern part of the CB. b) Raw image displaying the high-resolution bathymetry of the CB, and the locations of other referenced figures. **28**

13 Seismic profile A-A' across the southern Carmen Basin (SCB). a) Perspective 3D view of the 40-meter resolution bathymetry of the SCB, generated in Canvas Xgeo (https://www.canvasgfx.com). Abbreviation: VE = vertical exaggeration. The flare (acoustically imaged gas bubble plume) emerging from the seafloor was imaged using the Interactive Visualization Systems (IVS) Fledermaus 8.4.2 software package (www.qps.nl). b) Raw seismic image. c. Structural and stratigraphic seismic interpretation. d. Interpreted geologic cross-section. Depth in panel d was converted from Two Way Travel Time to meters assuming a seismic velocity of 1500 m s-1. The seismic image reveals a wide, symmetrical graben bounded by two primary normal faults, identified as cross-basin structures (Figure 12). The subsidence created by these faults provides **33**

accommodation space for 0.73 s of TWTT (~550 m) of sedimentary sequences deposited above an acoustic basement interpreted as a young oceanic crust. Panel c) highlights high-amplitude reflections at a depth of 4.15 s, possibly indicating an ancient spreading center near abandoned nested normal faults. The dashed red line shows the location of magmatic intrusion interpreted as saucer-shaped sills. Low-amplitude facies in the seismic data may indicate fluid or gas migration toward the seafloor, as shown in the flare in panel a.

14 Seismic profile B-B' across the central Carmen Basin (CCB). a) Perspective 3D view of the 40-meter resolution bathymetry of the CCB, generated in Canvas Xgeo (https://www.canvasgfx.com). b) Raw seismic image. c) Structural and stratigraphic seismic interpretation. d) Interpreted geologic cross-section. The image reveals an asymmetrical half-graben structure bounded by NW-striking normal faults accommodating 0.40 s (~300 m) of syn-tectonic sedimentation. In panel c, at a depth of 3.73 s, tabular high-amplitude reflections suggest the presence of an ancient spreading center, similar to Figure 13. **35**

15 Seismic profile C-C' across the northern Carmen Basin (NCB). a) Perspective 3D view of the 40-meter resolution bathymetry of the NCB, generated in Canvas Xgeo (https://www.canvasgfx.com). Abbreviations: ROV = remotely operated vehicle; VE = vertical exaggeration. b) Raw seismic image. c) Structural and stratigraphic seismic interpretation. d) Interpreted geologic cross-section. The profile intersects the axial graben of the northern CB. The spreading center is interpreted as asthenospheric mantle reaching near the seafloor to generate new ocean crust. **36**

16 Seismic profile D-D' spans the northernmost part of the Carmen Basin (CB) a) Perspective 3D view of the 40-meter resolution bathymetry, generated in Canvas Xgeo (https://www.canvasgfx.com). b) Raw seismic image. c) Structural and stratigraphic seismic interpretation. d) Interpreted geologic cross-section. The seismic data reveals buried faults beneath sediments, indicating their potential older age compared to the normal faults in the CB. The basement extends along the entire seismic profile at depths between 2.27 and 3.1 s of TWTT (~1700 and 2100 mbsl). It is interpreted that this material is of volcanic origin, evident from seismic reflections exhibiting good lateral continuity and ropey-like high-amplitude features. Notably, a significant seismic feature is a submarine hill toward the NW (Figure 12), suggesting it is the youngest feature of the section. **38**

17 Seismic profile E-E' spans the axial graben of the southern Carmen Basin (SCB). a) Perspective 3D view of the 40-meter resolution bathymetry of the **39**

SCB, generated in Canvas Xgeo (https://www.canvasgfx.com). Abbreviations: PDZ = principal displacement zone; VE = vertical exaggeration. The flare emerging from the seafloor was imaged using the Interactive Visualization Systems (IVS) Fledermaus 8.4.2 software package (www.qps.nl). b) Raw seismic image. c) Structural and stratigraphic seismic interpretation. d) Interpreted geologic cross-section. The seismic data reveals a steeply dipping Farallon transform fault (Figure 12), which accommodates 0.73 s of syn-tectonic sedimentation. Toward the basin center, sedimentation decreases to 0.67 s-thick (Figure 13). Notably, an uplifted footwall exhibits a tabular-shaped high-amplitude seismic feature spanning ~2 km. This feature is interpreted as a saucer-shaped sill magmatic layer, leading to folding structures within the upper stratigraphic successions (Kluesner, 2011).

18 Seismic profile F-F' illustrates the eastern part of the southern Carmen Basin (SCB). a) Perspective 3D view of the 40-meter resolution bathymetry of the SCB, generated in Canvas Xgeo (https://www.canvasgfx.com). The flare emerging from the seafloor was imaged using the Interactive Visualization Systems (IVS) Fledermaus 8.4.2 software package (www.qps.nl). b) Raw seismic image. c) Structural and stratigraphic seismic interpretation. d) Interpreted geologic cross-section. The image displays a domino faulting system striking to the SE, accommodating 1.1 s of syn-tectonic strata at the depocenter. In b) and c), the sedimentary pattern reveals distinct seismic facies with inclined cross-bedding and erosion surfaces indicating southeastward deposition. These sedimentary packages potentially represent different facies compared to the sedimentary fills of the Carmen sub-basins, suggesting the presence of submarine fan deposits. **40**

19 Geometry models of southern basins in the Gulf of California. a) Guaymas basin (GB). b) Farallon basin (FB). c) Carmen Basin (CB). d) Alarcon Basin (CB). e) Northern Pescadero basin (NPB). f) Southern Pescadero basin (SPB). g) Northern, Central, and southern sub-basins of the CB. The smaller structures, like the northern CB and NPB, exhibit a rhomboidal geometry, while the larger structures, such as GB and FB, display a rectangular geometry. **41**

20 Plot showing the relationship between the onset of seafloor spreading and the length of the accreted oceanic crust in different pull-apart basins in the southern Gulf of California (Lizarralde et al., 2007; DeMets et al., 2010; Umhoefer 2011). The plot clearly shows that the time scales linearly correlates to the lenght of the basins (Table 1). Abbreviations: GB = Guaymas basin; FB = Farallon basin; CB **45**

= Carmen Basin; NPB = Northern Pescadero Basin; SPB = Southern Pescadero Basin; NCB = Northern Carmen Basin; CCB = Central Carmen Basin; SCB = Southern Carmen Basin.

21 Regional map illustrating the crustal boundaries of the Guaymas, Carmen, and Farallon basins. The oceanic crust of the Guaymas basin is highlighted in light green, while the CB is represented by the bathymetric data from the multi-beam survey (40-m resolution; Figure 3). The Farallon basin is highlighted in light yellow. The dotted yellow line indicates the transition from old oceanic crust (late Miocene for the Guaymas basin and early Pliocene for the Farallon basin; Lizarralde et al., 2007; DeMets et al., 2010; Umhoefer, 2011) to young oceanic crust (early Pleistocene for the Carmen basin; Table 1). The purple line marks the boundary between continental and oceanic crust. Abbreviations: CBOC = Carmen basin oceanic crust; COT = Continental-oceanic transition; FBOC = Farallon basin oceanic crust; GBOC = Guaymas basin oceanic crust; OOT = Oceanic-oceanic transition. The schematic cross-section model is based on interpretations by Gregg et al. (2007), Wang et al. (2009) and Di Luccio et al. (2014). The schematic diagram depicts the dynamic upwelling of the mantle at the mouth of the Gulf of California as an extension of the East Pacific Rise (EPR), which facilitates the formation of new oceanic floor. **47**

22 Conjugate margins based on deep seismic data (from Allen and Allen, 2013). a) Symmetric margin (pure shear), and b) asymmetric margin (simple shear) with a lithospheric detachment fault. COB stands for continent-ocean boundary. **56**

23 a) Structural map of the Farallon basin illustrating the two-dimensional architecture and geometry (http://www.geomapapp.org).
b) High-resolution (40-m) bathymetry is imaged using the Interactive Visualization Systems (IVS) Fledermaus 8.4.2 software package (www.qps.nl). **62**

24 Seismic profile G-G' collected parallel of Farallon Transform fault on the northwestern Farallon basin. a) Raw seismic image and structural, stratigraphic seismic interpretation . b) Interpreted geologic cross section. **66**

25 Seismic profile I-I' surveyed near profile G-G' subparallel to the Farallon Transform fault on the northwestern Farallon basin. a) Raw seismic image and structural, stratigraphic seismic interpretation. b) Interpreted geologic cross section. Profile H-H' illuminates off-axis magmatic intrusions, including saucer-shaped sills. **67**

26 Seismic profile I-I' surveyed parallel to the Farallon transform and subparallel to profiles G-G' and H-H'. a) Raw seismic image and structural, stratigraphic seismic interpretation. b) Interpreted geologic cross section. Profile I-I' illuminates off-axis magmatic intrusions, including saucer-shaped sills. **68**

27 Seismic profile J-J' surveyed on the northwestern side of the Farallon basin across the continental - oceanic transition of the BC microplate and the south Farallon Massif at the southeastern end. a) Raw seismic image and structural, stratigraphic seismic interpretation. b) Interpreted geologic cross section. Profile J-J' illuminates off-axis magmatic intrusions, including saucer-shaped sills. Note that the acoustic basement exhibits high amplitude continuous layers toward the southeast, while such reflections are absent toward the northwest. This observation may indicate the transition from oceanic to continental crust. **70**

28 Seismic profile K-K' subparallel of profile J-J', collected on the northwestern side of Farallon basin across the continental - oceanic transition of BC microplate until Farallon-south Massif at the southeastern side. a) Raw seismic image and structural, stratigraphic seismic interpretation. b) Interpreted geologic cross section. Profile K-K' illuminates off-axis magmatic intrusions, including saucer-shaped sills. Note that the acoustic basement exhibits high amplitude continuous layers toward the southeast, while such reflections are absent toward the northwest. This observation may indicate the transition from oceanic to continental crust. **71**

29 Seismic profile L-L' across northeastern Farallon Basin, crossing Farallon Transform. a) Raw seismic image and structural, stratigraphic seismic interpretation. b) Interpreted geologic cross section. Profile L-L' illuminates off-axis magmatic intrusions, including saucer-shaped sills. **73**

30 Seismic profile M-M' surveyed across the northwestern side of Farallon basin across the Sobrero basin (Figure 23). a) Raw seismic image and structural, stratigraphic seismic interpretation. b) Interpreted geologic cross section. Profile M-M' shows off-axis magmatic intrusions, including saucer-shaped sills. **74**

31 Seismic profile N-N' collected on the southeastern side of Farallon basin across the main axis of Farallon basin. a) Raw seismic image and structural, stratigraphic seismic interpretation. b) Interpreted geologic cross section. Profile N-N' shows Farallon basin axis magmatic intrusions, including saucer-shaped sills. **76**

32 Seismic profile O-O' across Farallon Transform on the southeastern Farallon Basin. a) Raw seismic image and structural, stratigraphic seismic interpretation. **77**

b) Interpreted geologic cross section. Profile O-O' shows the continental - oceanic transition on the Mexico midland continental shelf. Note, that the acoustic basement exhibits high amplitude continuous layers toward the southwest, while such reflections are absent toward the northeast. This observation may indicate the transition from oceanic to continental crust.

List of tables

Table		Page
1	Seismic data acquisition parameters in the Carmen basin, southern Gulf of California, Mexico.	**11**
2	Basin age inferred from length of accreted ocean floor in the southern Gulf of California assuming a spreading rate of 52 mm/yr (DeMets and Dixon, 1999).	**44**

I. INTRODUCTION

I.1. Crustal deformation and development of marine basins

In deep-water extensional systems, the process of crustal deformation to create spreading centers and the generation of new oceanic crust is related to a strong component of horizontal extension. The main factors controlling the timescale of continental rifting include crustal thickness, lithospheric rheology, thermal structure, and the magnitude of stresses applied to the lithosphere (Allen and Allen, 2013). During early stages of crustal extension, lithospheric rupture is slow and can range from 25 to 80 Ma (Bohannon et al., 1989; Menzies et al., 1997; Abbate et al., 2001; Ziegler and Cloetingh, 2004; Omar and Steckler, 1995; Pik et al., 2008; Corti, 2009; Duque-Trujillo et al., 2015; Brune et al., 2016). However, during advanced phases, extensional velocity abruptly increases, leading to accelerated extension and the opening of a marine basin (Brune et al., 2016). In this tectonic extensional regime, crustal deformation can be accommodated through two mechanisms (Figure 1): (1) pure shear (McKenzie, 1978), where the lower crust is thinned by plastic deformation and decoupled from the upper crust by brittle deformation, forming symmetric rift systems where horizontal extension is balanced against vertical thinning; and (2) simple shear (Wernicke, 1981, 1985), where deformation is controlled by a detachment fault system that cuts through the crust, leading to rotational deformation in the hanging wall, forming an asymmetric rift zone (Allen and Allen, 2013).

Pull-apart basins are extensional structures that naturally occur due to the interaction of a series of sub-parallel strike-slip master faults, which are topographic depressions formed in an extensional overlap or releasing bend or a strike-slip fault or fault zone(Mann et al., 1983; Christie-Blick and Biddle, 1985; Dooley and McClay, 1997; van Wijk et al., 2017). These

structures develop in zones of strike-slip deformation typically formed by localized extension across master fault systems. Thus, pull-apart basins develop in an extensive range of geodynamic settings, such as oceanic and continental environments.

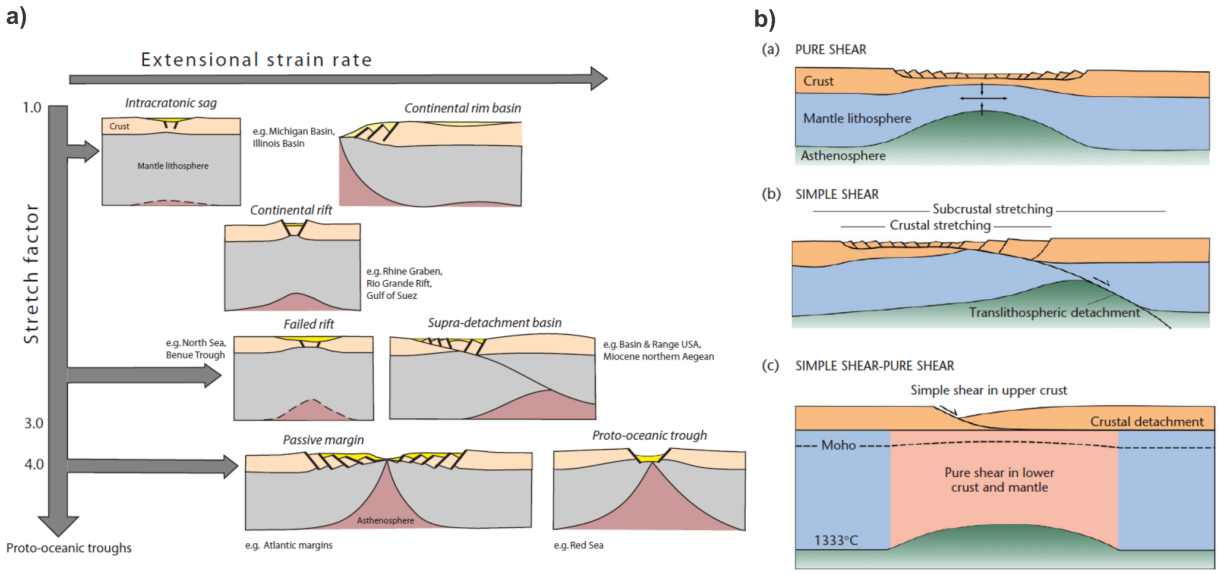

Figure 1. a) Conceptual model showing the evolution of the rift–drift basin suite in terms of increasing stretch factor and extensional strain rate. **b)** Models of strain geometry in rifts. (a) Pure shear geometry features an upper brittle layer over a lower ductile layer, creating a symmetrical lithospheric cross-section. (b) Simple shear geometry involves a low-angle detachment fault that divides the lithosphere into an upper plate (hanging wall) and a lower plate (footwall). (c) Hybrid model combines simple shear in the upper crust, using listric or planar faults, with pure shear in the ductile lower crust and mantle lithosphere. From Allen and Allen (2013).

Strike-slip faults have linear to curvilinear geometry in plan view and generally possess a Principal Displacement Zone (PDZ), where the bulk shear strain is accommodated and secondary structures develop, such as Riedel shear and P-shear fractures (Christie-Blick and Biddle, 1985; Allen and Allen, 2013; Fossen, 2010). The relative motion of the crustal blocks involved in pull-apart systems can be either parallel to the bounding PDZs (pure strike-slip) or oblique/divergent to the PDZs (transtensional) (Figure 2). In cross-section, the PDZ commonly

branches upwards into a splaying system of faults, producing either positive or negative flower structures (Allen and Allen, 2013).

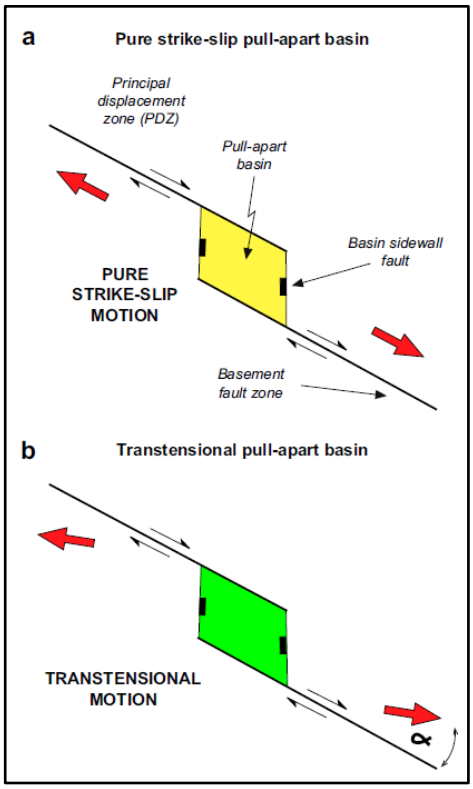

Figure 2. General characteristics of a pull-apart basin in a dextral side-stepping fault system. The pull-apart basin is defined to develop in pure strike-slip when $\alpha = 0^{\circ}$ and in transtension when $0^{\circ} < \alpha \leq 45^{\circ}$. From Wu et al., (2009).

Pull-apart basins are different from other types of depressions as they typically have a rhomboidal shape. The geometry of the pull-apart basins results from their length-to-width ratio and is controlled by the amount of fault overlap or underlap of the master transforms (Man et al., 1983; Wu et al., 2009; van Wijk et al., 2017). The growth of these structures is closely related to the spatial-temporal propagation of the strike-slip faults (Figure 3). According to Wu et al. (2009), transtensional pull-apart basins exhibit margins dominated by en-échelon oblique-extensional faulting and often develop dual depocenters separated by an intra-basinal high, which are formed by cross-basin faults . Examples of tectonic environments where pull-apart

basins develop include the Gulf of California (van Wijk et al., 2017), the Vienna basin, Dead Sea basin, and the Gulf of Eilat in the Red Sea (Wu et al., 2009).

Strike-slip fault systems are discontinuous on many scales, and parameters such as fault separation and the length of overlap of the master fault segments are essential for the shape and development of pull-apart basins (Gürbüz, 2010). Several pull-apart basin geometries have been recognized and range from spindle shape to elongated rhomboidal lazy S or Z shape (van Wijk et al., 2017). An evaluation of the length, width, depth (sediment thickness), and acute angle are the geometric properties to consider the kinematics and geological evolution of pull-apart basins (Gürbüz, 2010). Aydin and Nur (1982) suggested that pull-apart basins have a characteristic length-to-width ratio of approximately 3:1 in a 2-D plan view. The low length-to-width ratio of pull-apart basins is a consequence of their short lives and rapidly changing strike-slip zones (Man et al., 1983; Gürbüz, 2010).

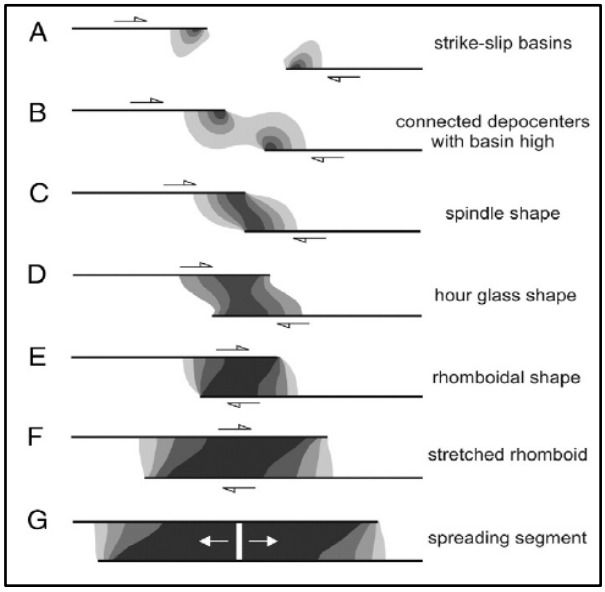

Figure 3. Schematic model (plan view) of the basin geometries observed in extensional systems. The geometries of the strike-slip fault traces are shown with black lines in each of the panels. The areas colored in grayscale indicate the increase in depth as the fault traces overlap (darker tones, greater depth). The arrows indicate the direction of shearing. (Adapted from Van Wijk, 2017; modified from Mann, 1983).

I.2. Geologic background of the Gulf of California

The Gulf of California (GC) (Figure 4) is a structural basin characterized by NW-SE oriented right-lateral transtensional deformation system, spanning approximately 1500 km in length and 200 km in width. Since the Late to Recent Miocene, a series of pull-apart basins have formed within the GC (Lonsdale, 1989; Stock and Hodges, 1989; Bohannon and Parsons, 1995; Aragón Arreola and Martín-Barajas, 2007; Umhoefer, 2011; Contreras-Pérez et al., 2012; Duque-Trujillo et al., 2015). These basins encompass environments ranging from transitional and neritic to pelagic settings (Helenes et al., 2009). The northern region of the GC illustrates the effects of substantial sedimentation during lithospheric mantle thinning and rifting processes (Martín-Barajas et al., 2013). This area is characterized by active basins to the west (Delfin, Consag, Wagner, Cerro Prieto, and Salton), and abandoned basins to the east (Tiburón and Aldair-Tepoca), encompassing broad and shallow basins with sedimentary packages reaching up to 6 km in thickness. These sediments originate from the Colorado River, deposited since the Late to Recent Miocene (Wagner, Consag, Delfín, and Tiburón basins; Aragón-Arreola et al., 2005; González-Fernández et al., 2005; Aragón-Arreola and Martín-Barajas, 2007; Contreras-Pérez et al., 2012; Martin-Barajas et al., 2013). In contrast, the central and southern parts of the GC are characterized by deep water depths, narrow, elongated basins with sedimentary thicknesses up to 1 km, and interconnected by a well-defined array of right-lateral, right-stepping transform faults developed over transitional and oceanic crust (Guaymas, Carmen, Farallon, and Pescadero basins; Lonsdale, 1989; Fenby and Gastil, 1991). Further south, the Alarcón Basin is part of a distinct system where the formation of new oceanic crust has been documented since approximately 3.5 Ma (Lonsdale, 1989; DeMets, 1995; Mar-Hernández et

al., 2012). This basin has a spreading rate of approximately 52 mm/year and well-defined magnetic anomalies extending towards the East Pacific Rise (Figure 4) (DeMets, 1995; Lizarralde et al., 2007; Umhoefer et al., 2007).

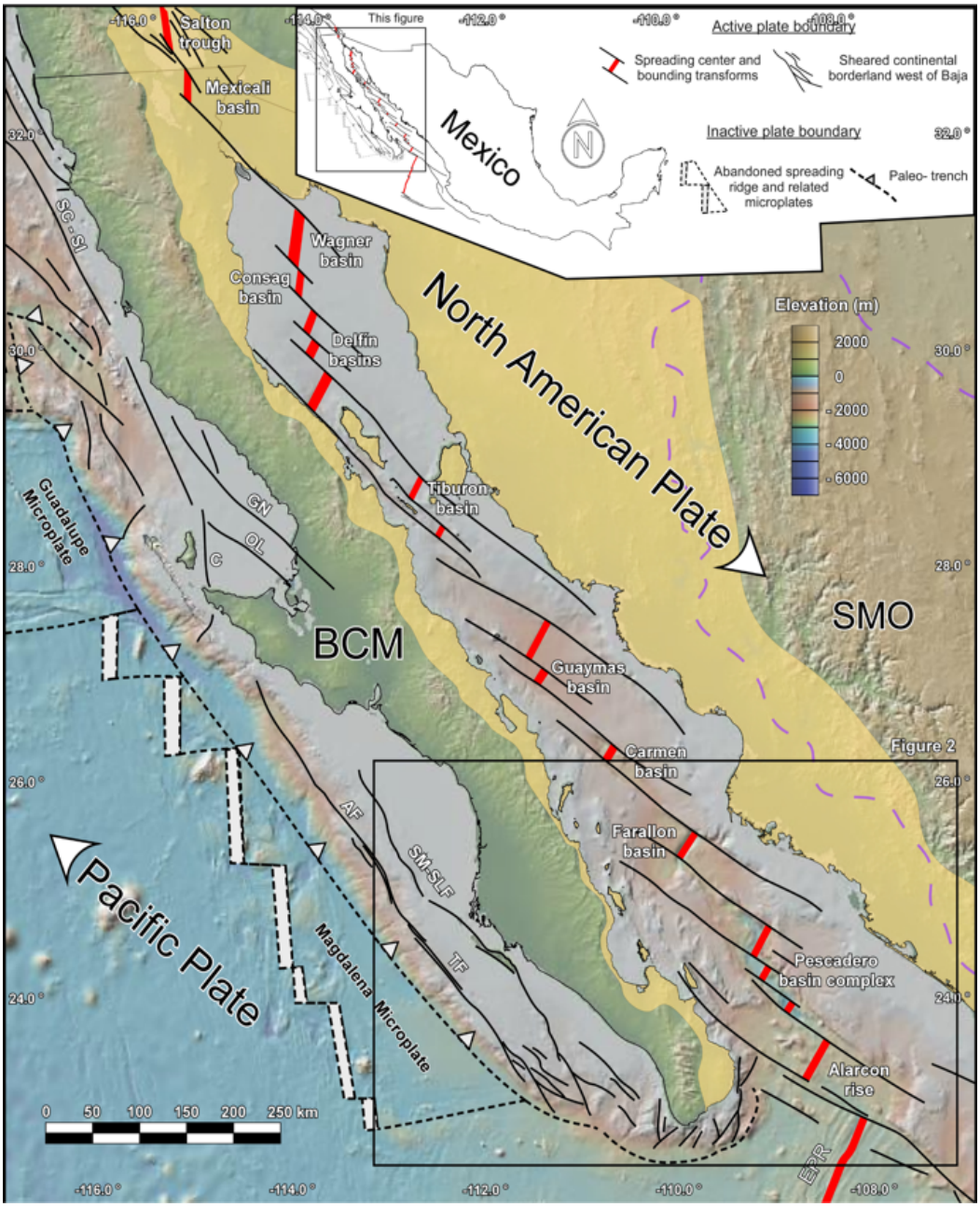

Figure 4. Regional tectonic map of the Gulf of California (GC). Abbreviations: EPR = East Pacific Rise; TF = Tosco fault; SM-SLF = Santa Margarita-San L´azaro faults, AF = Abreojos fault; GN = Guerrero Negro fault; OL = Ojo de Liebre fault; C = Cedros fault; SC-SI = Santa Catalina-San Isidro faults. From Ramírez-Zerpa et al. (2022).

In extensional systems such as the GC (Figure 4), the mechanisms of crustal deformation and its geological history are complex. The magmatic provinces of the Baja California Peninsula and northwest Mexico record the tectonic history of the subducted Farallon plate beneath the North American plate during the Mesozoic era (Gastil, 1993; Fletcher et al., 2007). As a result of this contractional system, regional metamorphism and subduction-related magmatism resulted in the formation of a peninsular batholith, primarily composed of igneous intrusions (Silver and Chappell, 1988; Walawender et al., 1990; Duque-Trujiullo et al., 2015; Bot et al., 2016), while during the Cenozoic, volcanic arc deposits dominated throughout the peninsula (Gastil et al., 1979; Hausback, 1984; Stock and Lee, 1994; Martín-Barajas et al., 1997; Fletcher and Munguía, 2000; Martín-Barajas, 2000). The Farallon plate was consumed beneath the North American plate during the Cenozoic. Part of the North American Plate became coupled to the Pacific plate and has since been dragged northwestward, initiating the process of continental rifting (Ferrari et al., 2018). This event marked the onset of early extension in the late Oligocene to early Miocene (Gans, 1997; McDowell et al., 1997; Wong et al., 2010; Ferrari et al., 2013; Balestrieri et al., 2017). The Farallon Plate completed the subduction process by the end of the middle Miocene, and the first formation of oceanic crust occurred in the early Pliocene (Atwater and Severinghaus, 1989; Lonsdale, 1991; Ferrari et al., 2018). Additionally, lithospheric rupture is believed to have occurred within only 6-10 Ma, forming an anomalously rapid basin system (Umhoefer, 2011; Duque-Trujillo et al., 2015). The axis of the GC is characterized by a right-stepped array of strike-slip faults with right-lateral shear connecting a series of pull-apart basins, which collectively accommodate a transtensional deformation with an NW-SE orientation from the late Middle to Late Miocene (Figure 5).

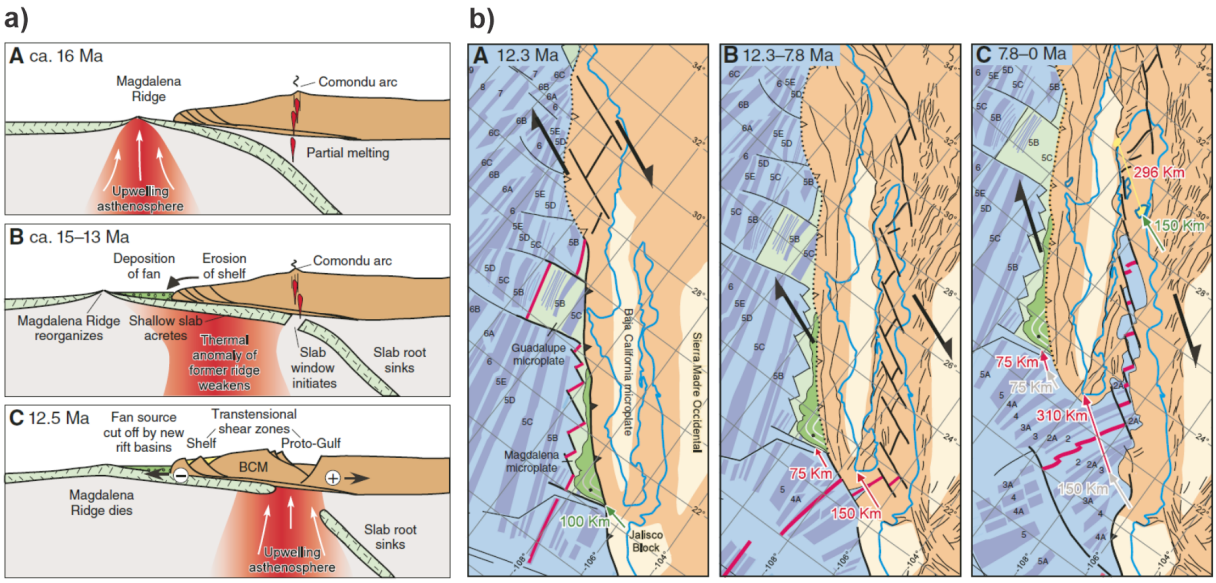

Figure 5. a) Schematic cross section of the paleotrench illustrating the slab break-off process under Baja California. The diagrams show: A) An active subduction setting. B) The formation of a slab window after subduction ends, transitioning to a transform boundary where the upper part of the slab resists subduction while the lower end is pulled down. C) The lower slab continues descending until the slab stretches, deforms, and finally breaks off, sinking into the mantle. **b)** A), B), C) Cartoon illustrating the kinematic model for shearing around the Baja California microplate represents the single-phase development of two deformation zones simultaneously, since ~12 Ma Modified from Fletcher et al. (2007).

In the present thesis work, we focus on the problem of crustal deformation and its relationship with the formation of pull-apart basins in the southern portion of the GC, aiming to propose a tectonic evolution history based on contrasting structural mechanisms (see McKenzie, 1978; Wernicke, 1981, 1985). The main objective is to construct a kinematic model of the Carmen and Farallon basins using 2D seismic reflection data (Figure 6). To achieve this objective, we characterize the geometry and structure of this portion of the GC, to identify different styles of crustal deformation, conduct a structural analysis of the extensional system, and to define the mode of crustal extension and rift formation.

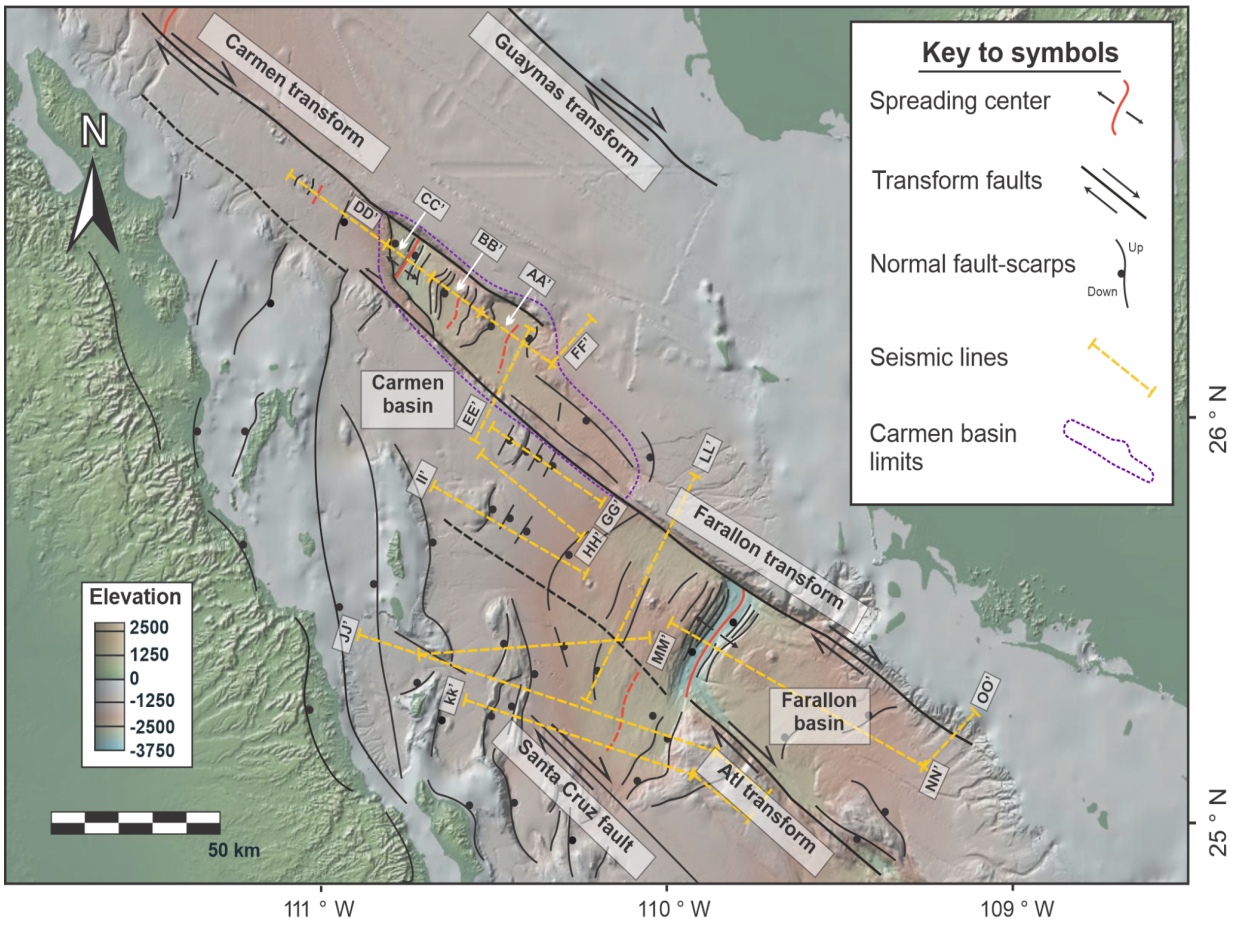

Figure 6. Regional tectonic map of the Carmen Basin and Farallon Basin, with labeled master transform faults (black). Multichannel seismic profiles are indicated by yellow lines. Base map sourced from GeoMapApp (http://www.geomapapp.org).

I.3. OBJECTIVES

I.3.1. General Objective

- Construct a regional geological framework of the southern part of the Gulf of California using 2D seismic reflection data collected through the Carmen and Farallon basins.

I.3.2. Specific Objectives

- Characterize the geometry and structure of the southern Gulf of California rift system to identify the different stages of crustal deformation.

- Elaborate kinematic evolution models for different crustal deformation stages.
- Characterize the seismic-stratigraphy and magmatism associated with the formation of geothermal fluids.

I.4. METHODOLOGY

I.4.1. Multichannel seismic reflection data processing

Seismic surveying is a valuable technique for providing information about the structure and elastic properties of the subsurface. It utilizes artificially generated elastic waves to analyze ground features, giving information about its composition and internal geometry for a variety of industrial and scientific applications (Yilmaz, 2001). Seismic exploration involves the controlled generation of seismic waves at the earth's surface or seafloor, employing acoustic energy sources such as explosions or vibrators. These waves propagate through the ground in the form of compressional and shear waves, interacting with geological layers and producing reflections, refractions, and diffractions at interfaces between different materials (Sheriff and Geldart, 1995). Seismic data are recorded by sensors called geophones or hydrophones, which detect reflected and refracted seismic waves. This data is processed and analyzed to construct models of the subsurface structure, revealing the distribution of geological layers, faults, salt domes, and other features of geophysical interest (Yilmaz, 1991). This geophysical method has numerous applications in various industries, from prospecting for natural resources such as oil, gas, and minerals to evaluating ground stability for infrastructure construction. For instance, in basin analysis, it provides detailed images of the geometry and stratigraphy of sedimentary basins, allowing for the reconstruction of the basin's evolutionary history, including sediment deposition, sea-level changes, and tectonic deformation (Yilmaz, 2001).

In the southern GC, seismic data recording was carried out during September 2006, aboard the R/V Francisco de Ulloa, owned by the Centro de Investigación Científica y de Educación Superior de Ensenada (CICESE) in collaboration with Scripps Institution of Oceanography of San Diego (UCSD). During the campaign, seismic data were collected along more than 2000 linear km, of which ~160 km were processed for this work along the Carmen basin axis and perpendicular to the main structures that delimit the basin and ~295 km were processed for this work along the Farallon basin axis and perpendicular to the Farallon transform fault that delimit the basin on the northwestern side. Moreover, we show ~314 km of seismic profiles from (Piñero-Lajas, 2008) across the Baja California microplate submerged continental crust and parallel to the Farallon transform (Figure 6). The data are freely available through the institutional repository at http://cicese.repositorioinstitucional.mx/jspui/handle/1007/3659. Details of data acquisition are presented in Table 1.

Table I. Seismic data acquisition parameters in the Carmen basin, southern Gulf of California, Mexico.

	Values
Power Source	Air cannon delivering 150 cubic inches per shot
	Operating pressure: 2000 psi (13.8 MPa)
Recording Cable	Length: 600 m
	Channels: 48 (hydrophones)
	Channel spacing: 12.5 m (40 ft)
Data Recording Period	6 seconds
Sampling Interval	1 ms
Total Samples per Trace	6000
Inter-Source Distance	37.5 m
Recording time	6000 ms
Redundancy	800%
Air Gun	Sercel GI (generation-injection) gun
Signal Conversion	Analog to digital conversion
	Multiple numerical measurements per unit of time (samples)

The seismic reflection data were processed using the open-source Seismic Unix software (https://wiki.seismic-unix.org/start). The process was performed in three (3) stages: pre-stacking (Figure 7), stacking (Figure 8) and post-stacking (Figure 9) (Sheriff and Geldart, 1995; Yilmaz, 2001). In the first stage, data are adjusted to a geographic coordinate reference system, high noise traces are removed, and band-pass filtering is applied to retain frequencies of interest. Deconvolution is then performed to recover high frequencies and equalize signal amplitudes. The second stage involves grouping traces by Common Depth Points (CDPs) and applying velocity analysis, including Normal Move Out (NMO) correction, to align traces to zero offset. Summation of traces from different seismic records enhances the signal-to-noise ratio. The third stage focuses on migration to eliminate diffractions and accurately relocate reflectors. Additional techniques, such as predictive deconvolution and amplitude gain methods, enhance image resolution and visualization. The resulting seismic images provide a detailed representation of the subsurface, with the vertical scale presented in Two Way Travel Time (TWTT).

I.4.1.1. Pre-stacking processing

The pre-stacking processing, detailed in Figure 7, involved the transformation of data from SEG-Y to SU format for compatibility with Seismic Unix software. Out of the 52 recorded traces, 48 belonging to data channels were retained, while the remaining 4 were discarded, which were operational control traces. The resulting seismic reflection profile (Figure 7a) initially exhibited chaotic amplitude and frequency distributions. Prior to frequency filtering, spectral analysis (Figure 7b) was imperative. Coherent reflection energy was identified within frequency ranges of 30-35 Hz and 135-145 Hz, while noisy frequencies, such as environmental and equipment-induced noise, were discarded. The f-k filter (Figure 7c), also known as a

velocity or slope filter, was utilized to eliminate linear trend coherent noise. This filter aids in discerning events aligned along straight lines with different velocities, effectively attenuating guided waves, refractions, and spatial aliasing (Yilmaz, 2001). Filter slopes were calculated from the origin of the f-k spectrum, allowing for the removal of spatial aliasing effects and enhancing the definition of shallower reflections (Yilmaz, 1987). However, this filter introduced high-frequency noise requiring subsequent band-pass frequency filtering.

Geometric calculations were applied to locate shots and traces, facilitating the determination of CDPs. Spherical Divergence correction was employed to mitigate amplitude loss caused by wavefront expansion, with an initial velocity correction of 1500 m/s, corresponding to water's P-wave velocity (McQuillin et al., 1979). This correction amplified signal amplitudes at longer times while reducing those at shorter times (Figure 7d). Deconvolution, the inverse process of convolution, was employed to isolate ground-provided signal components, enhancing temporal resolution. Autocorrelation analysis aided in identifying periodic components attributed to the source and non-periodic components stemming from subsurface reflectors (Yilmaz, 1987). Deconvolution was selectively applied to eliminate source reverberations, while multiples were retained as they posed minimal interference with the main signal due to their higher arrival times (Figure 7d).

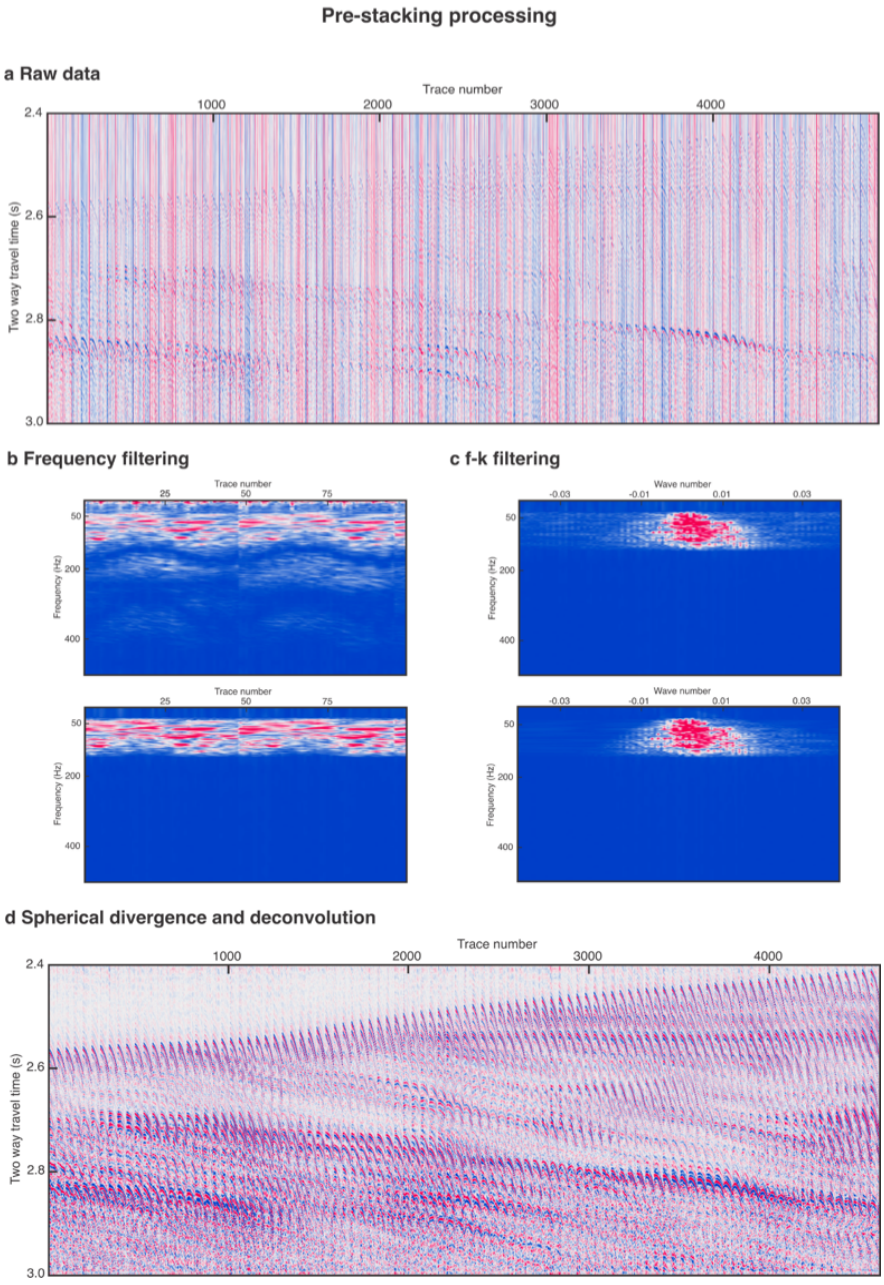

Figure 7. Pre-stacking processing transformed data from SEG-Y to SU format for Seismic Unix compatibility. Of the 52 recorded traces, 48 data channels were retained, and 4 were discarded.. **a)** The seismic reflection profile initially showed chaotic amplitude and frequency distributions. **b)** Spectral analysis identified coherent reflection energy within 30-35 Hz and 135-145 Hz. Noisy frequencies were discarded. **c)** The f-k filter removed linear trend coherent noise, enhancing shallow reflections. **d)** Spherical Divergence correction mitigated amplitude loss, applying an initial velocity correction of 1500 m/s. Deconvolution improved temporal resolution by isolating signal components. Selective deconvolution eliminated source reverberations while retaining multiples due to their minimal interference with the main signal.

I.4.1.2. Stacking processing

This stage aims to enhance signal quality by summing traces with the same reflection point in depth. By the end of this process, non-coherent noise and a significant portion of coherent noise, such as multiples, are attenuated (Figure 8). Traces are initially grouped by CDPs, representing the vertical projection of the Common Mid Point (CMP) in ideal conditions (i.e., horizontal and homogeneous layers; Yilmaz, 1987). All traces within a CDP are reflected at approximately the same points, allowing for their summation to yield a CDP trace with improved signal-to-noise ratio (Figure 8a).

Velocity analysis is employed to identify subsurface velocities that best align traces to zero offset. The semblance spectrum method (Figure 8b) involves cross-correlation of CDP traces across a range of velocity values. The resulting semblance spectrum aids in identifying velocities corresponding to maximum acoustic impedance contrast, while excluding velocities associated with multiples. The NMO describes how reflection times lengthen as the distance between the seismic source and receiver increases. To address this effect, NMO correction is applied using the velocity model derived from velocity analysis (Figure 8b). This correction aims to mimic data acquisition with zero offset, aligning reflectors horizontally in the corrected records. As a result, it becomes easier to combine traces within the same CDP (Figure 8c). Furthermore, this correction helps reduce interference from multiples caused by misalignment (Liner, 2004; Yilmaz, 2001). In the stacking process, traces within the same CDP are summed to amplify coherent signals and reduce non-coherent noise. This summation yields the initial seismic section, representing reflectors with zero offset. Subsequent modifications to processing parameters may be made to optimize the seismic section's quality (Figure 8c).

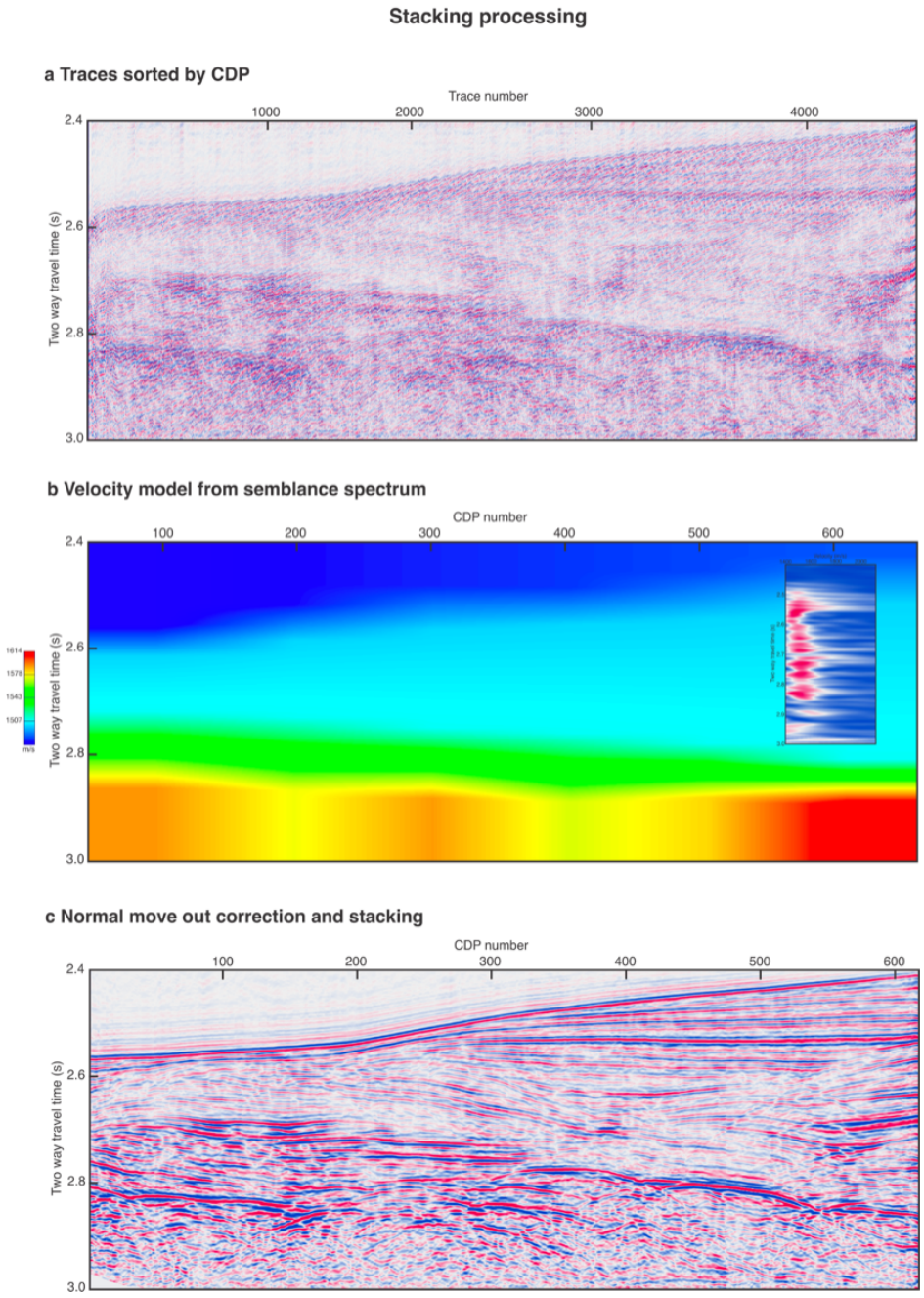

Figure 8. Stacking processing enhances signal quality by summing traces with the same reflection point, attenuating non-coherent noise and significant portions of coherent noise, such as multiples. **a)** Traces are grouped by CDPs, representing the vertical projection of the CMP. Summing these traces improves the signal-to-noise ratio. **b)** Velocity analysis, using the semblance spectrum method, identifies subsurface velocities for NMO correction. **c)** NMO correction aligns traces horizontally, making it easier to combine traces within the same CDP and reducing multiple interference. The stacking process sums traces to amplify coherent signals, yielding the initial seismic section with zero offset reflectors.

I.4.1.3. Post-stacking processing

Post-stack processing represents the final phase of data processing, primarily centered on migration (Figure 9a). Alongside migration, additional techniques aim to enhance image resolution, including predictive deconvolution for retrieving lost high frequencies and suppressing coherent noise. Moreover, amplitude gain methods may be utilized for improved visualization. Migration, the most computationally intensive process, aims to eliminate diffractions and accurately relocate reflectors, challenging the prior assumption of vertical reflection origins. Migration effects include increased horizon dip, shortened length, and upward movement opposite to the dip, as well as syncline narrowing and diffraction hyperbola collapse. Typically, migration employs velocities approximately 10% lower than NMO velocities to avoid over-migration, which can result in "smiles," upward concave-shaped noise artifacts, especially at edges due to energy limitations. This study focuses solely on time migration due to the absence of reliable well data for depth conversion. To address high-frequency noise, processes like top mute are applied to attenuate noise from different parts of the record (Figure 9a).

Before interpreting the resulting seismic reflection profile, understanding the size of detectable features is crucial. This is determined by the vertical and horizontal resolution. Calculated resolution is specific to certain areas, influenced by processing and terrain characteristics, providing a general result overview. Vertical resolution denotes the ability to differentiate close seismic events at different depth levels, which is calculated using the equation R=(T/4)*V, where *T* is the dominant period in seconds, and *V* is the velocity of the medium in meters/seconds. Widess (1973) initially proposed a resolution limit of λ/8, where λ is the dominant wavelength. However, due to noise considerations, a resolution threshold of λ/4

(Sheriff, 1997) is preferred, with extreme cases resorting to λ/2. For instance, with a wavelength of 0.02 s and a velocity of 3000 m/s, a vertical resolution of 30 m is achieved (λ/2). For sedimentary cover with a wavelength of 0.01 s and a velocity of 2000 m/s, the resolution is 20 m. Horizontal resolution refers to the ability to distinguish laterally displaced features as distinct events. For non-migrated data, it is defined by the Fresnel Zone (Yilmaz, 2001) R = (V/2)*sqrt(t0/f), where *T,* is the mean travel time in seconds, *V* is the velocity of the basement or sediment in meters/seconds, *t0*, is the wavefront travel time in seconds, and *f* is the dominant frequency in Hertz. According to Piñero-Lajas (2008), with a mean travel time of 4 s and a velocity to the basement of 3000 m/s, and a frequency of 50Hz, a horizontal resolution of 424 m is achieved. Similarly, for sediment with a double travel time of 2.5 s and a velocity of 2000 m/s, and a frequency of 100 Hz, a resolution of 25 m is attained. After data processing, a comprehensive seismic interpretation can be conducted to analyze the continuity, variability, and internal geometry of reflectors (Figure 9b), enabling the identification of key features such as fault planes, folds, grabens, and sedimentary sequences. Additionally, quantitative parameters including fault length, dip, stratal thicknesses, subsidence, and sequence boundaries can be determined by converting TWTT to depth in meters, assuming mean velocities of 1500 m/s. Finally, a geological interpretation can be derived from the analysis of structural features and stratigraphic sequences, integrating insights from seismic facies analysis, lithological variations, and depositional environments (Figure 9c). The horizontal distance conversion from CDP to meters was calculated based on the midpoint distance between each channel, resulting in 6.25 meters per CDP.

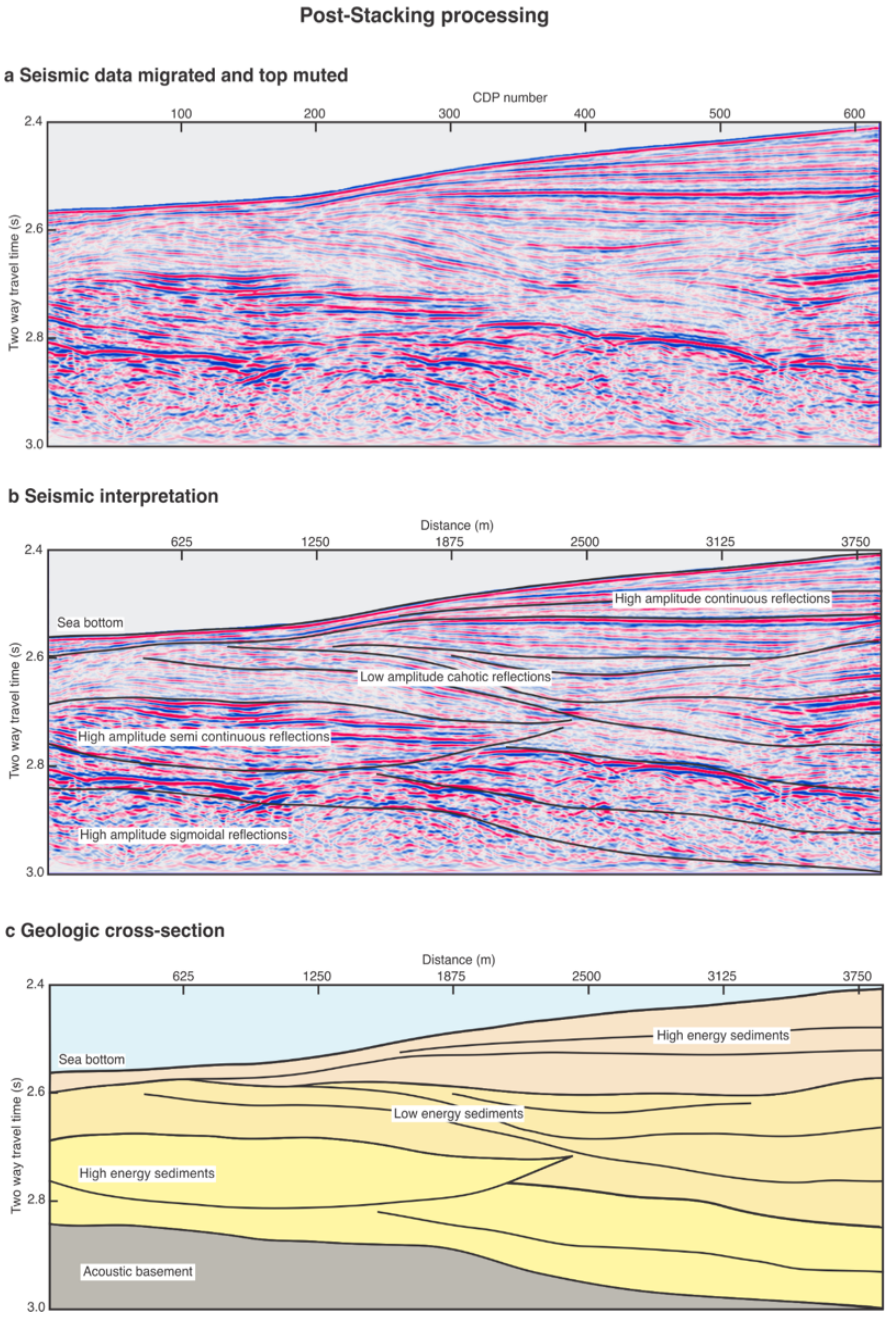

Figure 9. Post-stacking processing represents the final phase of data processing, primarily centered on migration. a) Migration effects include increased horizon dip, shortened length, and upward movement opposite to the dip, as well as syncline narrowing and diffraction hyperbola collapse. Typically, migration uses velocities approximately 10% lower than NMO velocities to avoid over-migration artifacts. b) Vertical resolution is calculated using R=(T/4)*V, while horizontal resolution is defined by the Fresnel Zone formula. c) After processing, seismic interpretation analyzes reflectors' continuity and geometry, identifying features like faults, folds, and sedimentary sequences. Horizontal distance conversion from CDP to meters is based on 6.25 meters per CDP.

II. STRAIN LOCALIZATION INSTABILITIES AND THE GENESIS OF MULTIPLE AXES OF SEAFLOOR SPREADING IN THE CARMEN BASIN, SOUTHERN GULF OF CALIFORNIA

II.1. Introduction

Despite recent progress in understanding the rifting dynamics of the Gulf of California (GC), significant gaps in information still exist due to extensive unexplored regions (Lonsdale, 1989; Aragón-Arreola et al., 2005; González-Fernández et al., 2005; Aragón-Arreola and Martín-Barajas, 2007; Lizarralde et al., 2007; González-Escobar et al., 2010; Contreras-Pérez et al., 2012; Martín-Barajas et al., 2013; Ramírez-Zerpa et al., 2022). This lack of information hinders our ability to establish a comprehensive context for the kinematics responsible for the opening of the GC, especially in the case of the pull-apart basins in the southern GC (Figure 10), where geological data is still missing or has poor spatial/temporal resolution (Sutherland et al., 2012 vs. Martín-Barajas et al., 2013).

It is known that the continental margins of the GC are highly extended and influenced by the development of low-angle master faults. These faults facilitate the isostatic rebound of the tectonically unloaded (ductile) lower plate and the formation of antiformal bulges that migrate in the direction of displacement of the (brittle) upper plate (Buck, 1988; Wernicke and Axen, 1988; Lavier et al., 1999; Fletcher and Spelz, 2009). Local conditions that favor the development of such low-angle structures include a thinned lithosphere and a high extension rate, which result in higher-than-normal heat flow values (Buck, 1988, 1993). Active rifting

across the southwestern margin of the GC (Umhoefer et al., 2020) has also been associated with east-directed low-angle normal faults and simple shear deformation, accommodating significant crustal extension (Fletcher et al., 2000; Fletcher and Munguia, 2000; Fletcher et al., 2003; Bot et al., 2016). In this region, strain results in ~40 km of linear extension toward the continental-oceanic crust transition, across the continental shelf of the Baja California peninsula (Figure 10; Macias-Iñiguez et al., 2019).

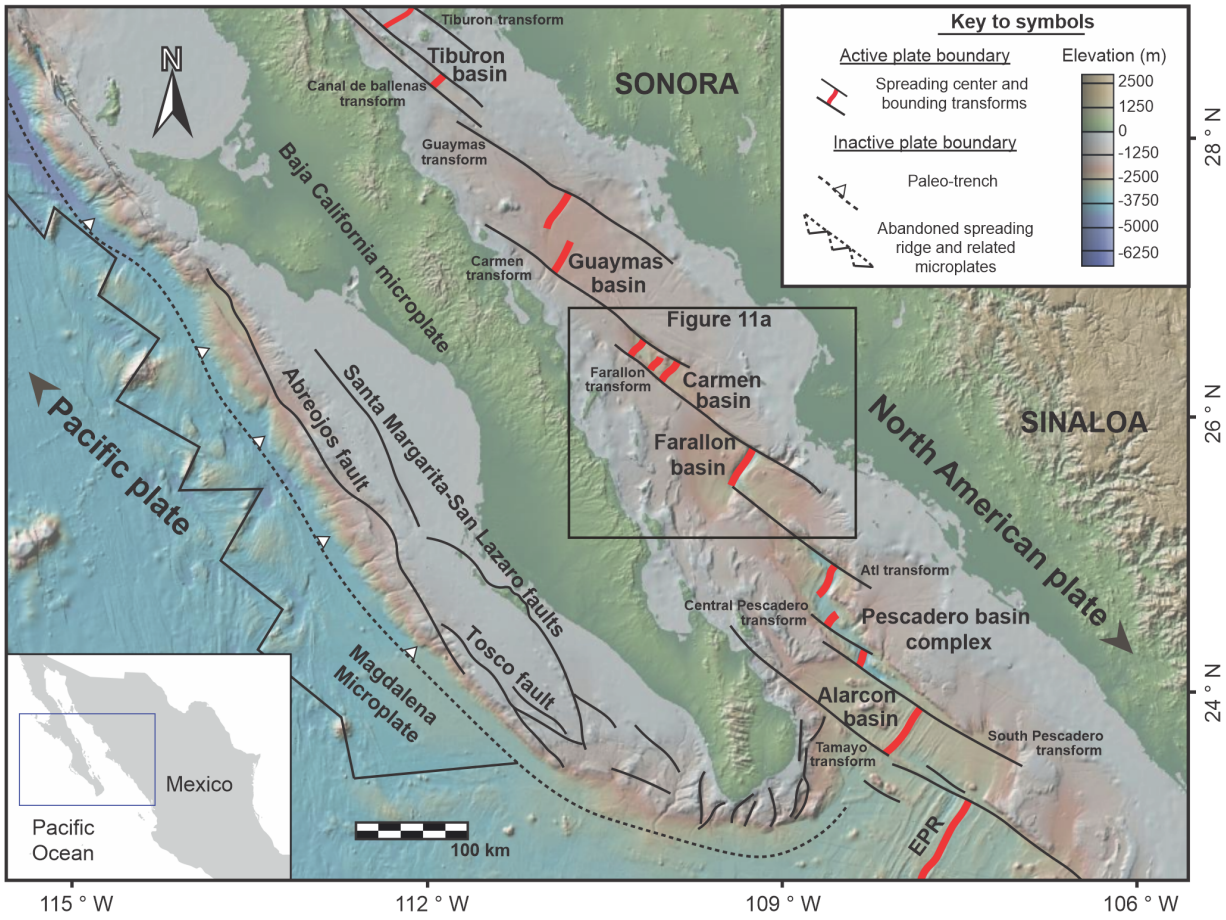

Figure 10. Regional Tectonic map of the southern Gulf of California showing plate motion (black arrows), transform fault system (black lines), pull-apart basins, and spreading centers (red lines). The Carmen Basin is indicated by the black box (Figure 2). The location of the paleo-trench and the partially subducted Magdalena microplate derived from the Farallon plate is marked by a black dashed line along the western margin of the Baja peninsula. The abbreviation EPR is used for the East Pacific Rise. Base map sourced from GeoMapApp (http://www.geomapapp.org).

According to Fornari et al. (1989), intra-transform spreading centers are a specific type of pull-apart basin found on oceanic transform faults, characterized by the development of short spreading centers surrounded by oceanic crust. Thus, oceanic transforms play a crucial role in the geology of mid-oceanic spreading ridges, where tectonic plates laterally move past each other, creating conditions conducive to the formation of intra-transform spreading centers (Gregg et al., 2006). These basins essentially consist of depressed regions between two offset segments of the mid-oceanic ridge, floored by oceanic crust (Mann et al., 2007). Therefore, oceanic transforms at mid-oceanic spreading ridges give rise to pull-apart basins floored by oceanic crust, resembling those observed in the Siqueiros and Garret transform faults on the East Pacific Rise (Pockalny et al., 1997; Gregg et al., 2007).

In this research, we aim to establish a kinematic evolution model of the Carmen basin (CB; Figures 10 and 11) using two-dimensional (2D) seismic reflection profiles and high-resolution bathymetry collected by Centro de Investigación Científica y de Educación Superior de Ensenada, Baja California (CICESE), Scripps Institution of Oceanography at the University of California San Diego (UCSD), and the Schmidt Ocean Institute (SOI) in 2006 and 2021, respectively. Here, we characterize the geometry and structure of the CB to identify: (*i*) different stages of crustal deformation, (*ii*) the basement lithology, (*iii*) the seismic-stratigraphy, and (*iv*) the magmatic events preserved in the stratigraphy of the basin. Additionally, we compare our results against other neighboring basins in the southern GC using geological data (Duque-Trujillo et al., 2014, 2015; Umhoefer et al., 2020), seismic reflection images (Lizarralde et al., 2007; Piñero-Lajas, 2008; Sutherland et al., 2012; Kluesner, 2011; Kluesner et al., 2014; Macias-Iñiguez et al., 2019; Ramírez-Zerpa et al., 2022), mantle tomography data (Wang et al., 2009; Di Luccio et al., 2014; Ferrari et al., 2018), and analog modeling of pull-apart basins (van

Wijk et al., 2017; Wu et al., 2009; Farangitakis et al., 2021) to reconstruct the structural evolution of this segment of the southern GC rift system. Finally, we discuss how the opening of the GC contributes to the formation of new oceanic crust, how the oceanic lithosphere is deformed to accommodate younger spreading centers, and the kinematics of the transform faults that currently make up the boundary between the Pacific and North American plates.

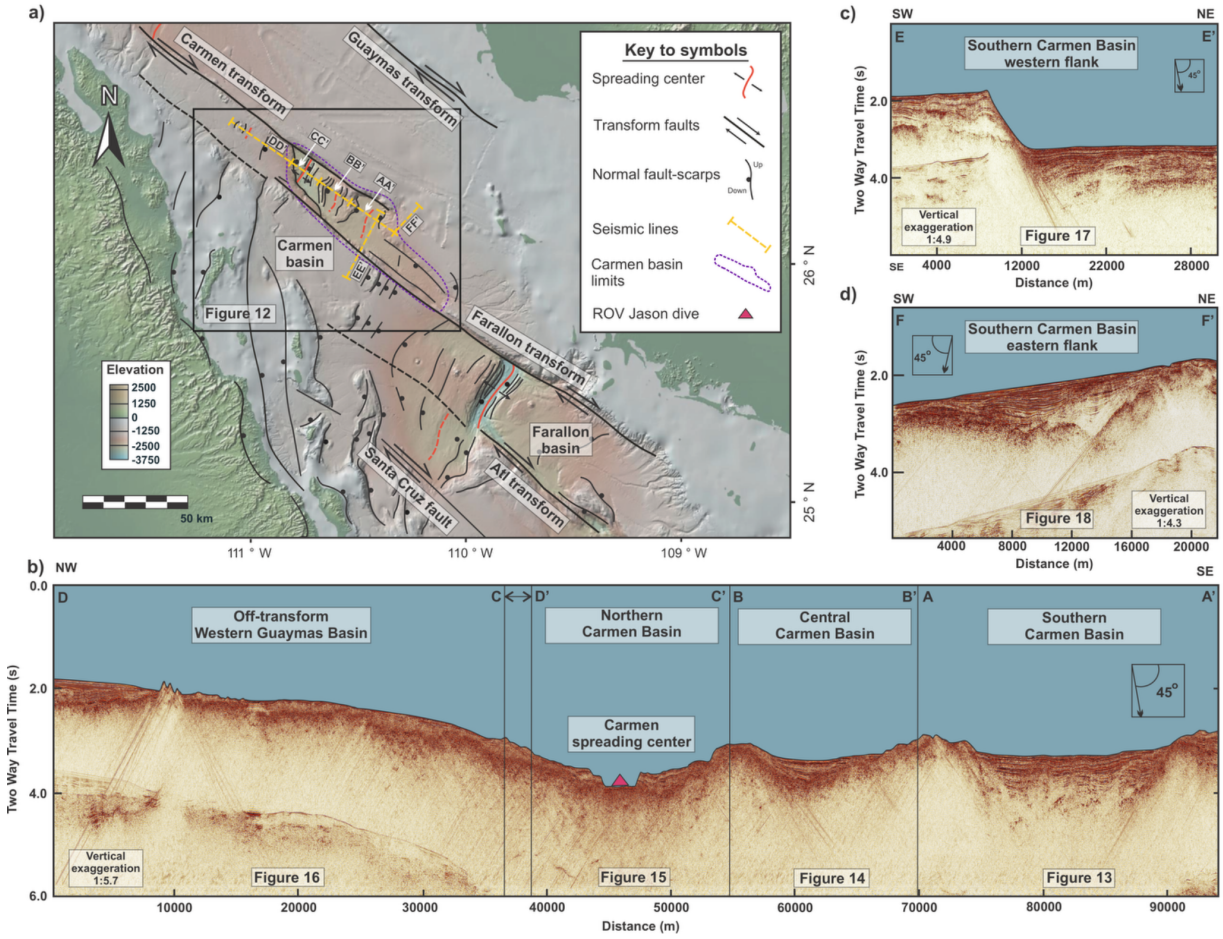

Figure 11. a) Regional tectonic map of the Carmen Basin (CB), with labeled master transform faults (black). Multichannel seismic profiles are indicated by yellow lines. The black box corresponds to the CB shown in Figure 3. Base map sourced from GeoMapApp (http://www.geomapapp.org). **b), c), d)** 2D multichannel seismic reflection data across the CB. Seismic lines are divided by vertical black lines corresponding to Figures 4-9.

II.2. Tectonic evolution of the Gulf of California

The northwestern continental margin of Mexico is a good example of a transition from a convergent plate boundary to an oblique-divergent margin. During the Paleogene, the Farallon oceanic plate subducted beneath North America, and a divergent boundary between the Farallon plate and the approaching Pacific plate existed near the Baja California paleo-trench (Fletcher et al., 2007; Balestrieri et al., 2017). In the Eocene, the Farallon plate was consumed, and part of the East Pacific Rise (Atwater, 1970) neared the paleo-trench. During the Oligocene, the East Pacific Rise directly interacted with the paleo-trench and the North American plate (Atwater, 1989; Stock and Hodges, 1989; Bunge and Grand, 2000; Wright et al., 2016), leading to the breakup of the Farallon plate as the Pacific–Farallon spreading center approached North America (Wright et al., 2016).

The proximity of the Pacific-Farallon divergent margin to the continental borderland marked the end of Neogene subduction, initiating lithospheric extension and dextral shearing along the Magdalena plate boundary derived from the Farallon plate. Intraplate magmatism occurred along the Baja California peninsula due to viscous shearing (i.e., Tosco-Abreojos-Santa Margarita–San Lazaro fault zone; Figure 10; Spencer and Normark, 1979; Atwater and Stock, 1998; Negrete-Aranda et al., 2013). In the early Miocene, the Farallon plate fragmented into several small plates, including the Guadalupe and Magdalena microplates, which, together with a section of the North American plate (i.e., California and Baja California peninsula), became coupled with the Pacific Plate (Wang et al., 2013) and started moving northwestward (Figure 10; Nicholson et al., 1994; Bohannon and Parson, 1995).

Dextral-oblique shearing migrated eastward from the continental margin into the current GC (Umhoefer et al., 2020). Crustal thinning in this region was permitted by a regional east-directed detachment system running along the Baja California peninsula and Sinaloa rifted margins (Ferrari et al., 2018). Eventually, brittle/ductile deformation (McKenzie, 1978) became localized into the present-day GC. Simple-shear tectonics and crustal extension of the upper plate, decoupled from the lower crust, led to isostatic compensation, mantle upwelling, and the intrusion of dykes and sills, facilitating the breakup of the continental crust (Wernicke, 1981). This process, accompanied by increased rift obliquity, facilitated plate boundary localization, marine incursion in the northern GC, and the formation of shallow water basins during the upper Miocene (Bennett et al., 2016; Umhoefer et al., 2018). The current tectonic regime, established in the early Pliocene, involved the East Pacific Rise extending into the GC (Wang et al., 2009, 2013), separating the Baja California peninsula from the North American continent as new oceanic crust surfaced in the southern GC (Lizarralde et al., 2007), permitted by right-lateral, right-stepping transform faults (Fletcher et al., 2007).

II.3. Methods

New high-resolution bathymetry data for the CB were collected during the FK210922 expedition in October 2021 aboard the R/V *Falkor*, operated by the Schmidt Ocean Institute (SOI). The data were acquired using an EM 302 multibeam echo sounder at a 30-kHz frequency, capturing up to 864 soundings with dual swath mode. This enabled detailed seabed mapping along the entire CB basin axis at 40-meter intervals. The survey lines were spaced 5 km apart, running sub-parallel to the master transform faults that bound the basin. Data collection occurred at an average ship speed of 8 knots.

To study the rift evolution of the CB, we analyzed ~160 km of 2D seismic reflection data collected in 2006 aboard the R/V *Francisco de Ulloa* during a collaborative effort involving Centro de Investigación Científica y de Educación Superior de Ensenada, Baja California (CICESE), and Scripps Institution of Oceanography at the University of California, San Diego (UCSD). The seismic data, labeled AA'-FF' (Figure 11) included a 108 km section (AA'-DD') parallel to the CB axis, along with two perpendicular sections, EE' (30 km long) and FF' (22 km long).

The seismic reflection data was processed using the open-source Seismic Unix software (https://wiki.seismic-unix.org/start). We applied a three-stage workflow to generate sub-surface seismic reflection images: pre-stack, stack, and post-stack processing (Sheriff and Geldart, 1995; Yilmaz, 2001). This workflow enabled frequency extraction, multiple mitigation, signal amplitude equalization, noise reduction, precise ray trajectory correction, and spurious effect attenuation (Sheriff and Geldart, 1995; Yilmaz, 2001).

Well-proven criteria, such as the continuity/variability of reflections, seismic character, and internal geometry of reflectors, were used to identify key structural features such as fault planes, folds, grabens, and sedimentary sequences. Quantitative parameters, including fault length and dip, stratal thicknesses, subsidence, and sedimentary sequence boundaries, were also determined (e.g., maximum flooding surfaces, erosion surfaces, and correlatable surfaces). Seismic facies analysis enabled the identification of basement lithology and sedimentary material, including magmatic injections and geothermal fluids, usually in the form of mosaic patterns of highly reflective surfaces (e.g., saucer-shaped sills; Polteau et al., 2008) and low-reflectance surfaces (e.g., dim spots; Chopra and Marfurt, 2007).

II.4. Results

II.4.1. Geomorphology and 2D architecture of the Carmen Basin

The newly collected bathymetric data (Figure 12) reveal that the CB is a narrow, rhomboidal pull-apart basin developed between two dextral transform faults. The basin measures 100 km in length and 20 km in width, yielding a length-to-width ratio of 5:1 (Figure 12). Two sub-parallel, northwest-oriented principal displacement zones control the northeastern and southwestern margins of the CB. The Carmen transform fault extends 150 km, while the Farallon transform in the southwest stretches 200 km. These bounding zones overlap and connect through a transverse system of en-échelon oblique-extensional normal faults, creating three distinct sub-basins. The northernmost graben hosts the current seafloor spreading center measuring ~12 km in length (Figure 12).

The bathymetry of the CB reveals significant footwall uplift of the outer margin along the trace of the transform faults. This nearly vertical uplift is accommodated by an array of en-échelon segmented basin sidewall faults developed on both flanks of the CB (Figure 12). Along these steep faults, gravitational instabilities develop, leading to rapid and episodic slumping and grain flows, forming distinct cliffs with landslide crowns and scarps along the basin's outer margin (Figure 12). Yet, the primary sediment routing system for infilling the CB appears to be a submarine dendritic drainage system originating from the tips of the principal displacement zones (Figure 12).

At a finer scale, Figure 12 reveals a cross-basin fault system that propagates obliquely to the principal displacement zones. This fault system induces a left-stepping arrangement of synthetic Riedel shear faults (Christie-Blick and Biddle, 1985; Wu et al., 2009) that curve into

an elongated sigmoidal shape, connecting the sidewall faults at both sides of the basin. The resulting horst-graben structure divides the CB into three distinct sub-basins with contrasting morphologies (Figure 12): (*i*) the southern CB, (*ii*) the central CB, and (*iii*) the northern CB. Further details on these sub-basins are provided in the following paragraphs.

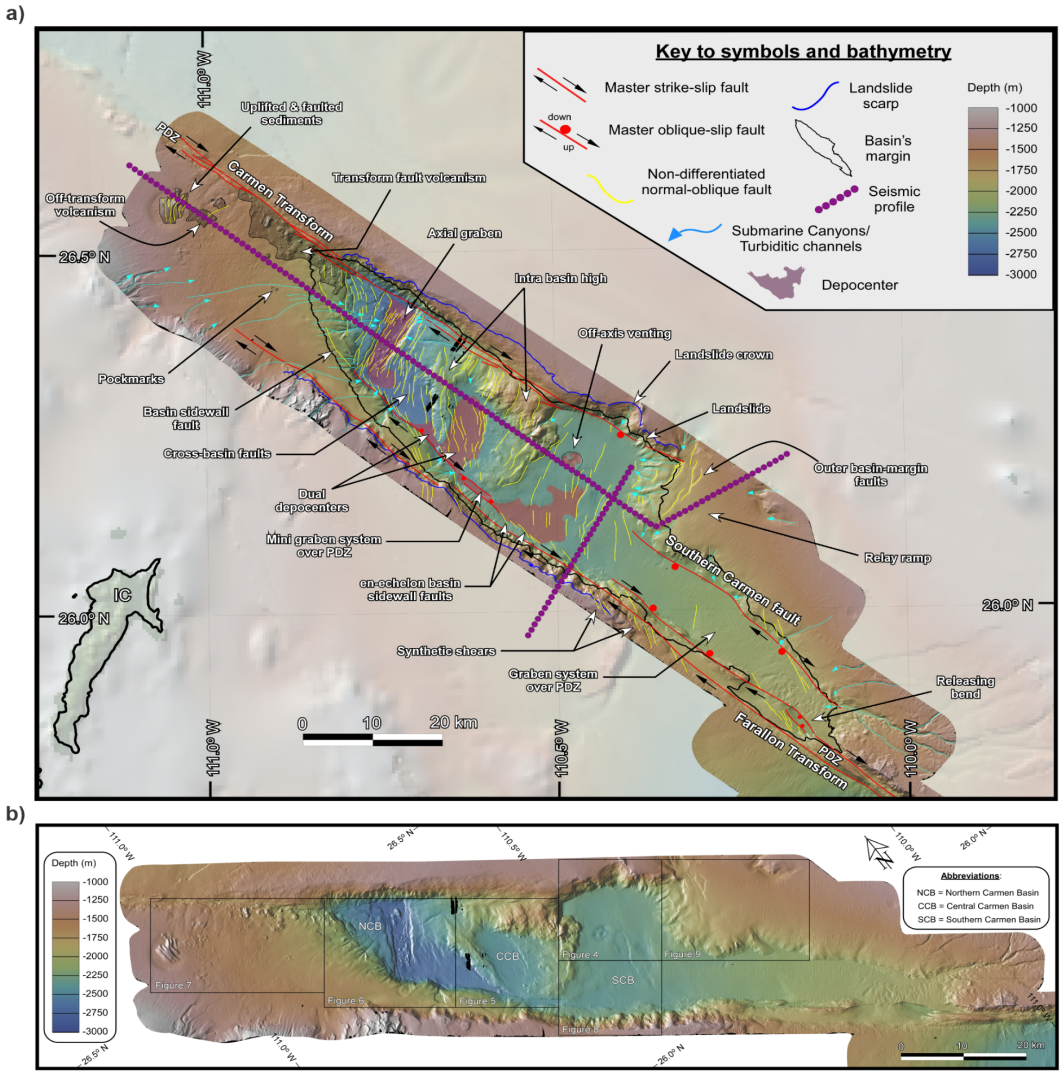

Figure 12. a) Structural map of the Carmen Basin (CB) illustrating the two-dimensional architecture and geometry. High-resolution (40-m) bathymetry is overlaid on faded Global Multi-Resolution Topography (GMRT) bathymetry. The map reveals a series of depocenters within the CB, with increasing depth from south to north. These sub-basins are bounded by two master strike-slip transform faults (red lines), connected by an array of cross-basin faults (yellow lines). The current seafloor spreading center is located in the northern part of the CB. **b)** Raw image displaying the high-resolution bathymetry of the CB, and the locations of other referenced figures.

Southern CB: The sub-basin features the shallowest depocenter (~2200 mbsl) among all the sub-basins. It has a length of ~20 km and a width of ~23 km. The basin is delimited by an array of cross-basin faults, oriented at a high angle to the bounding transform faults (Figure 12). The northern margin is bounded by an uplifted and translated crustal block, while the southern margin is delimited by a strike-slip relay ramp that transfers and accommodates the deformation between the Carmen transform fault and a secondary oblique-slip fault, which we refer to as 'Southern Carmen fault' (Figure 12). The NW-striking Carmen transform fault terminates abruptly against an array of NE-SW striking normal faults developed over the relay ramp on the outer basin-margin of the sub-basin (Figure 12). The relay ramp lies on the footwall of the oblique Southern Carmen fault, which controls a prominent graben system with a length of ~40 km and a width of ~15 km in the southeastern corner of the CB.

The graben system is parallel to the Pacific-North American plate boundary (Figure 10) and occurs along the divergent-wrench principal displacement fault zone associated with the Farallon transform. The graben is heavily sedimented and poorly cut by secondary faults traversing the smooth valley floor. The limited number of cross-basin fault scarps indicates their potential erosion or burial under the relatively thick layer of sediments derived from a dense network of drainages and submarine canyons that convey sediments to the southeastern portion of the basin (Figure 12). However, a small pull-apart basin, resulting from a releasing bend along the Farallon's right-lateral principal displacement zone, indicates ongoing tectonic stresses and the formation of an embryonic graben system in the southern corner of the basin (Figure 12). In the central portion of the southern CB, a circular feature with a diameter of ~3 km is interpreted as an area of off-axis venting a small depression formed as a result of the seepage of fluids and gasses through the seafloor and into the hydrosphere (Teske et al., 2020).

Central CB: The sub-basin is located at a depth of ~2400 mbsl. It has a length of ~20 km and a width of ~18 km. This structure acts as a connection between the northern and the southern CB. It is bordered by two intra-basin highs that have formed in response to a series of cross-basin faults that originate from synthetic Riedel shears (Wu et al., 2009) along the basin's sidewalls, connecting the master transform faults on each side of the CB (Figure 12). These structural highs can be attributed to block translation and rotation during the early stages of basin development. The geometry of the central CB is elongated and oval, with a northern orientation, suggesting that deformation may have ceased in this region, allowing its spreading center to migrate northwestward toward the northern CB (Figure 12). Variations in the topography of the central CB indicate the juxtaposition of different materials, with structural highs representing either a crystalline basement or possibly volcanic activity (Figure 12). Conversely, the subsided depocenter likely consists of sedimentary material derived from local and distant sources, including gravitational mass movements and submarine contour currents (Figure 12).

Northern CB: The sub-basin is located in the deepest part of the entire CB, reaching depths of ~2800 mbsl. It has a length of ~20 km and a width of ~20 km. The basin exhibits a broad nested graben where rocks have undergone downward displacement along an array of cross-basin faults connecting the bounding master faults (Figure 12). The overall geometry and geomorphological features of the northern CB suggest that the basin has evolved due to transtensional deformation (Wu et al., 2009), similar to the Pescadero basin complex located further southeast (Ramírez-Zerpa et al., 2022). The northern CB hosts the current seafloor spreading center, featuring a short and narrow axial graben oriented sub-perpendicular to the principal displacement zones. In 2008, the Woods Hole Oceanographic Institution's ROCA

expedition aboard the R/V *Atlantis* utilized the remotely operated vehicle (ROV) *Jason* to conduct a dive into the CB axial graben (Figure 11). During this dive, pillow basalts (ROCA 9J-10) were sampled within the active axis of CB as reported by Kluesner et al., (2011). Unlike the uplifted ramps that bound the opposite sides of the basin, the median valley floor is poorly sedimented and displays an irregular topography with rounded volcanic mounds (Figure 12). Magmatic activity is conspicuous not only across the spreading center but also along the bounding master faults, as well as in the elevated areas within the sub-basins. Extensive volcanic bodies can also be observed at the northern termination of the Carmen transform fault (Figure 12). Within this area, we identify a distinct feature that emerges on the seafloor, characterized by uplifted and faulted sediments, which in turn are often associated with off-axis magmatism (Teske et al., 2020).

II.4.2. Seismic interpretation of the Carmen Basin

The seismic interpretation of lines AA'-FF' (Figures 13-18) and morphological analysis in Figure 3 reveal the structural evolution of the CB. At a larger scale, the sub-basins exhibit three distinct seismic facies (Figures 13-18). From base to top in the seismic sections, the first seismic facies is interpreted as the acoustic basement, characterized by reflective, ropey-like layers with sigmoidal, semi-continuous reflections and strong lateral coherence. Below this layer, the acoustic basement continues at depth as reflections under which seismic signals are no longer received, thus in the seismic sections, these areas are attenuated (Figures 13-18). These rocks are interpreted as volcanic flows spanning a depth range from 3.87 to 2.27 seconds (s) of Two Way Travel Time (TWTT). Assuming a seismic velocity of the sea bottom reflection of 1500 m s^{-1}, we estimate that the depth of the acoustic basement varies between 2900 m to 1700 m (Figures 13-18). The two seismic facies overlying the acoustic basement represent

sedimentary layers filling the basin. The underlying facies consists of sequences with alternating medium and low-energy chaotic reflections, resembling accumulations of inter-glacial diatomaceous muds (Kluesner, 2011; Kluesner et al., 2014). The overlying facies consists of sequences with alternating medium and high-energy coherence reflections, displaying diatomaceous mud and sand turbidites deposited in a high-energy environment (Kluesner, 2011; Kluesner et al., 2014).

The seismic profile AA' spans 28 km, capturing the southern CB (Figure 13). The section trends NW-SE, parallel to the axis of the CB. The profile reveals a symmetrical horst-graben structure delimited by two high-angle cross-basin faults, resulting in a topographic step of 0.40 s of TWTT, which is ~300 m. These faults created sufficient subsidence for 0.73 s (~550 m) of syn-tectonic sequences (Figure 13). Siliciclastic material appears derived from uplifted areas surrounding the sub-basin and transport systems primarily located at the NW and SE ends of the CB (Figure 12). The basal seismic facies is interpreted as a highly fractured oceanic basement, observed as sigmoidal semi-continuous seismic reflections at a depth of 3.73 s on the southeastern graben flank. The lack of evidence of an active spreading center suggests the southern CB may be an abandoned axial graben. High-amplitude tabular reflections at a depth of 4.15 s indicate the location of the ancient spreading center, accompanied by magmatic intrusions forming sills, causing folding of the upper sedimentary sequences (Figure 13).

The acoustic basement is fully exposed toward the northwest, while the southwestern footwall block is covered by 0.40 s (~300 m) of sediments. In the right-hand part of the seismic section (Figure 13), the strata sequence of the uplifted footwall dips southeast, while the hanging wall slightly dips northwest, onlapping the bounding normal faults. Two sedimentary facies lie unconformably on the acoustic basement. The basal facies 0.33 s thick exhibits low-amplitude

chaotic reflections, indicating low-energy sedimentation. Growth strata change up-section to a seismic facies 0.40 s thick with good coherence and high-amplitude continuous reflections, indicating medium-high energy sedimentation environments (Figure 13).

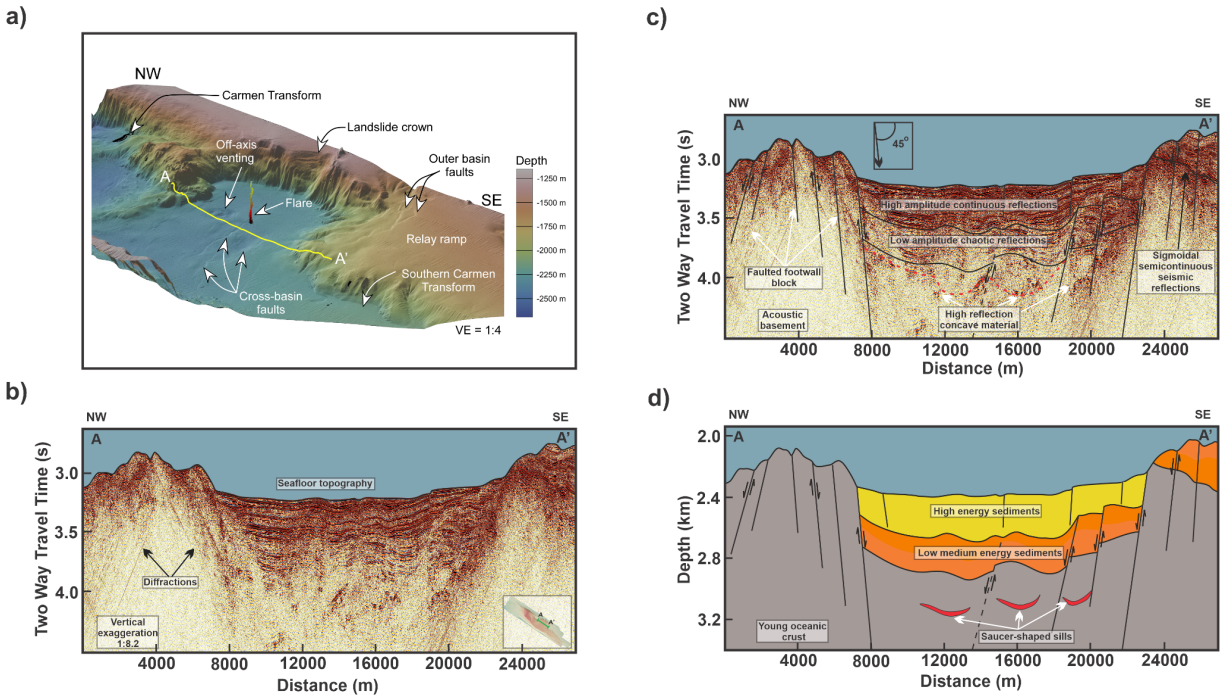

Figure 13. Seismic profile A-A' across the southern Carmen Basin (SCB). **a)** Perspective 3D view of the 40-meter resolution bathymetry of the SCB, generated in Canvas Xgeo (https://www.canvasgfx.com). Abbreviation: VE = vertical exaggeration. The flare (acoustically imaged gas bubble plum) emerging from the seafloor was imaged using the Interactive Visualization Systems (IVS) Fledermaus 8.4.2 software package (www.qps.nl). **b)** Raw seismic image. **c)** Structural and stratigraphic seismic interpretation. **d)** Interpreted geologic cross-section. Depth in panel **d)** was converted from Two Way Travel Time to meters assuming a seismic velocity of 1500 m s^{-1}. The seismic image reveals a wide, symmetrical graben bounded by two primary normal faults, identified as cross-basin structures (Figure 12). The subsidence created by these faults leads to 0.73 s of TWTT (~550 m) of sedimentary sequences deposited above an acoustic basement interpreted as a young oceanic crust. Panel **c** highlights high-amplitude reflections at a depth of 4.15 s, possibly indicating an ancient spreading center near abandoned nested normal faults. The dashed red line shows the location of magmatic intrusion interpreted as saucer-shaped sills. Low-amplitude facies in the seismic data may indicate fluid or gas migration toward the seafloor, as shown in the flare in panel **a**.

Profile BB' spans 20 km across the central CB (Figure 14). This sub-basin reveals an asymmetrical half-graben structure with a domino fault system defining the southern flank. The acoustic basement displays high-amplitude sigmoidal semi-continuous reflections at a depth of 3.73 s (~2800 m) and on both flanks at a depth of 3.20 s (~2400 m). In this basal seismic facies, the curvy reflections are interpreted as a young oceanic crust of volcanic origin (Figure 14), correlating with the basement rocks of the southern CB, located further southeast (Figures 12 and 13). In the middle of the central CB, at a depth of 3.73 s (~2800 mbsl), a 1 km-wide block of highly reflective material stands above the well-defined basement. The seismic expression of this feature resembles the ropey textured reflections seen in the surrounding basement, but it appears much brighter, which we interpret as the axis of an extinct seafloor spreading system that was active before the deposition of the overlying sedimentary sequence (Figure 14).

Above the acoustic basement, there is a syn-tectonic sedimentary package composed of two seismic facies, reaching a thickness of ~300 m (Figure 14). The underlying facies display layers with low-amplitude reflections and chaotic coherence, indicating sedimentation in low-energy environments. Along the NW margin, the basal sedimentary package shows a pronounced tilt toward the SE (Figure 14). The overlying facies exhibit high-amplitude reflections with good lateral coherence, indicating sedimentation in medium to high-energy environments, similar to the southern CB (Figure 13).

Profile CC' crosses the northern CB, spanning 17 km (Figure 15), representing the deepest and narrowest sub-basin. The axial graben is defined by inward-stepping normal faults striking perpendicular to the principal displacement zone (Figure 12), with a throw of 0.27 s along the graben margins. Our interpretation suggests these faults acted as fissures, accommodating the opening, and ~2400 m of young oceanic basement accreted between these

fissure walls at a depth of 3.87 s (~2900 mbsl). This inner graben represents the active spreading axis of the CB. In this area, the high-amplitude tabular reflections represent basaltic rocks collected by the Woods Hole Oceanographic Institution, during the 2008 ROCA 9J-10 dive, using the (ROV) *Jason* aboard the R/V Atlantis.

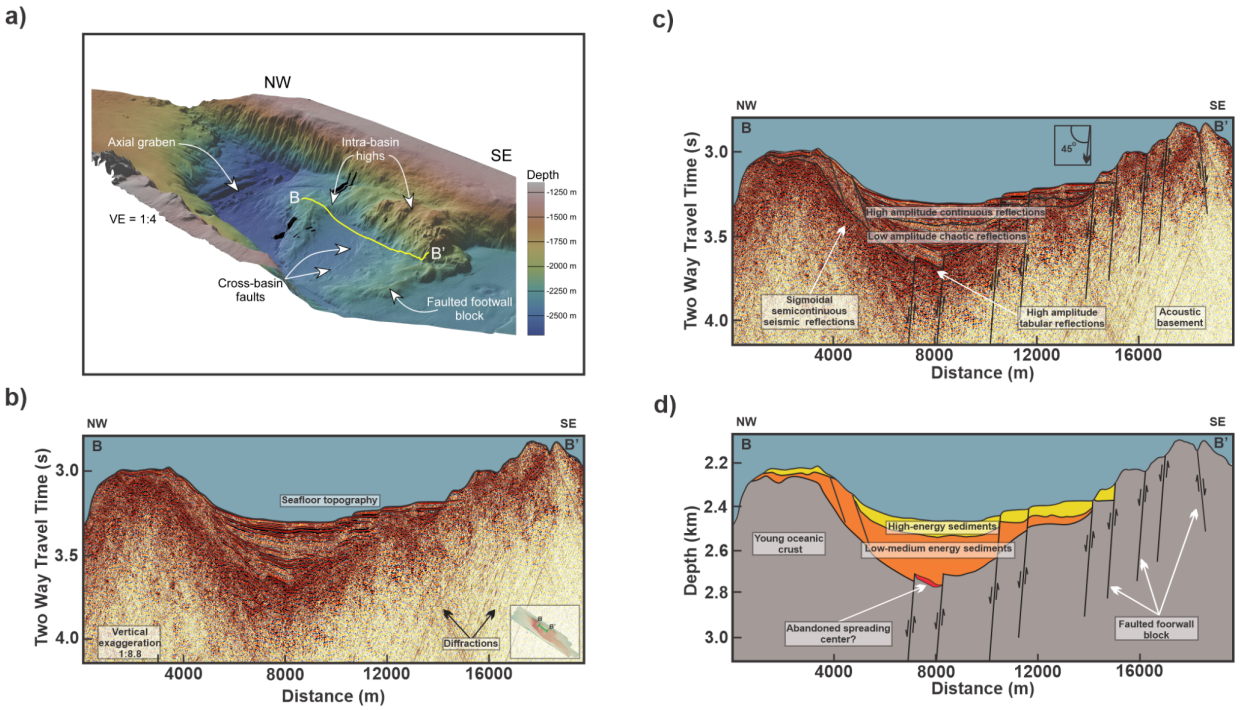

Figure 14. Seismic profile B-B' across the central Carmen Basin (CCB). **a)** Perspective 3D view of the 40-meter resolution bathymetry of the CCB, generated in Canvas Xgeo (https://www.canvasgfx.com). **b)** Raw seismic image. **c)** Structural and stratigraphic seismic interpretation. **d)** Interpreted geologic cross-section. The image reveals an asymmetrical half-graben structure NW-striking normal faults accommodating 0.40 s (~300 m) of syn-tectonic sedimentation. In panel **c)**, at a depth of 3.73 s, tabular high-amplitude reflections suggest the presence of an ancient spreading center, similar to Figure 13.

The sedimentary fill in the northern CB is notably thinner compared to the other Carmen sub-basins, measuring a thickness of 0.24 s (180 m). Observe, there is no sedimentary cover on top of the oceanic basement along the graben in the middle of the basin at a depth of 3.87 s (Figure 15). The two sedimentary seismic facies, characterized by high and low-amplitude

reflection, are correlated on both flanks of the sub-basin and are dissected by the graben (Figure 15). On the southeastern flank of the axial graben, the sigmoidal semi-continuous reflections reach the seafloor topography at a depth of 3.4 s depth, suggesting the young oceanic crust outcrops, whereas on the northwestern flank of the axial graben, the oceanic basement is covered by the two sedimentary units that we have interpreted throughout the CB.

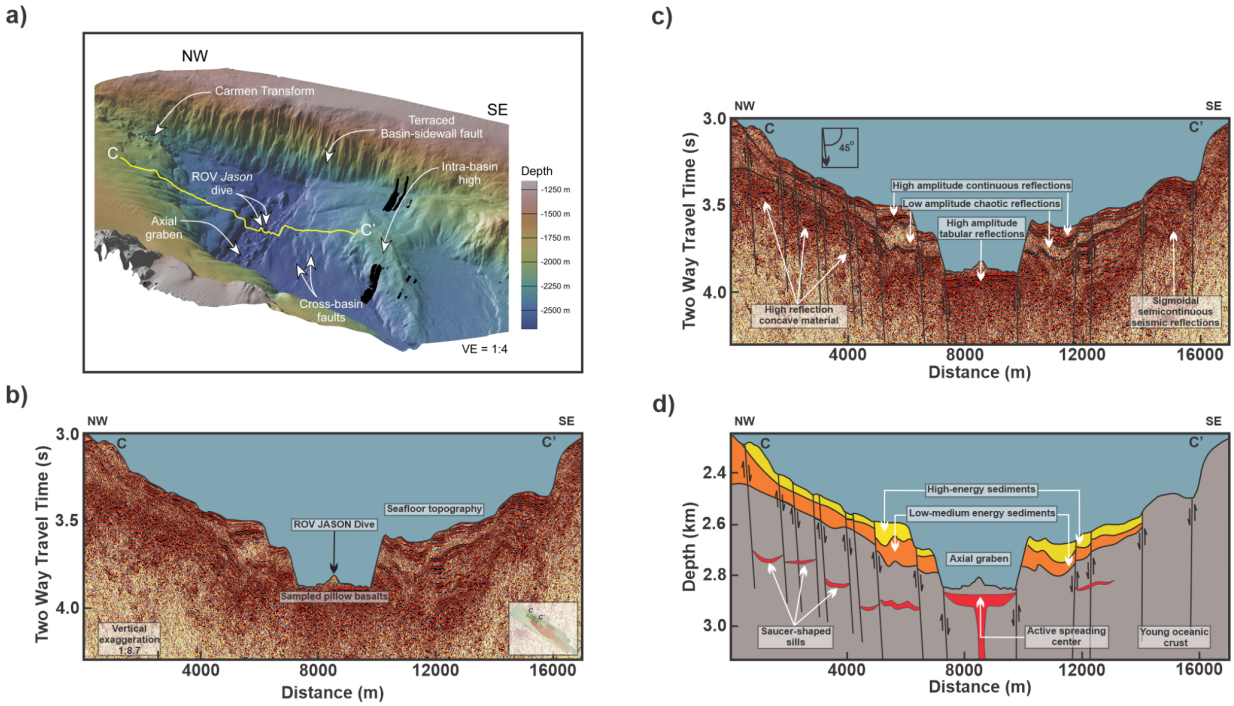

Figure 15. Seismic profile C-C' across the northern Carmen Basin (NCB). **a)** Perspective 3D view of the 40-meter resolution bathymetry of the NCB, generated in Canvas Xgeo (https://www.canvasgfx.com). Abbreviations: ROV = remotely operated vehicle; VE = vertical exaggeration. **b)** Raw seismic image. **c)** Structural and stratigraphic seismic interpretation. **d)** Interpreted geologic cross-section. The profile intersects the axial graben of the northern CB. The spreading center is interpreted as an asthenospheric mantle reaching the seafloor to generate new ocean crust.

Profile DD' spans ~43 km, overlapping ~5.7 km with the seismic profile CC', capturing the northern CB (Figure 16). The seismic image reveals a sloped architecture controlled by a domino normal fault system striking southeast. Beneath the sedimentary cover, well-defined, high-amplitude sigmoidal semi-continuous reflections with a thickness of 0.27 s indicate the

presence of an oceanic basement along the entire image (Figure 16). Toward the SE, a transition zone is interpreted from two main features: 1) a change in the dip of the ropey layer (i.e., tilted to the right of the seismic image and horizontal to the left), and 2) a change in depth of the basement layer (i.e., 3.1s–depth to the right of the seismic image and 2.27 s-depth to the left). This variation in bathymetric relief suggests a contrast in crustal density and across master transforms controlling adjacent basins (Figure 12). The transition zone likely corresponds to a shift from younger oceanic crust in the northern Carmen sub-basin towards the SE to older oceanic crust adjacent to the Guaymas basin (Figure 16). This area stands out for its abrupt seabed morphology, characterized by shallow chaotic reflections and acoustic signal loss, interpreted as uplifted and faulted sediments. This manifestation of off-axis magmatism is attributed to a dense network of sill intrusions throughout the surrounding areas (Teske et al., 2020). The latter interpretation is supported by the observation of off-transform volcanoes located in the northwestern part of the seismic profile, where the bathymetry is quite irregular, with small depressions and peaks reaching a zone of ~5200 m in length (Figure 16).

Profile EE' extends 30 km and provides detailed information on the structure of the western region of the southern CB (Figure 17). The seismic section intersects the Farallon transform fault toward the SW, interpreted as the basin's sidewall. At the hanging wall, the seismic facies sequence of this profile is consistent with the seismic profile AA', where the acoustic basement displays a prominent sigmoidal reflection of high-amplitude at a depth of 3.9 s (~2900 m), underlain by two distinct seismic facies characterized by low-amplitude non-coherence reflections, spanning a thickness of 0.33 s, and high-amplitude continuous reflections with a thickness of 0.4 s toward the uppermost part of the sedimentary sequence (Figures 12 and 17). Note that the footwall of the Farallon transform fault in the SW of the seismic image

displays concave high-reflection features at depths of 2.24 and 2.59 s of TWTT (Figure 17), suggesting the presence of saucer-shaped sill intrusions (Polteau et al., 2008; Kluesner, 2011).

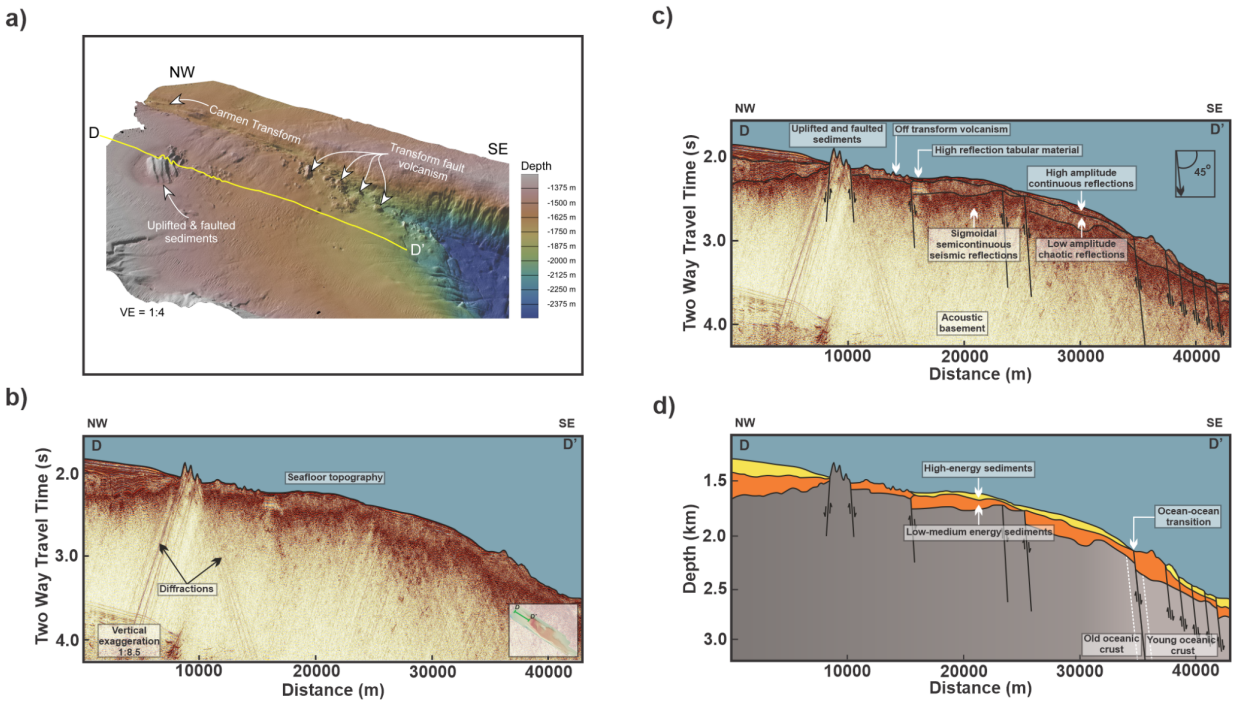

Figure 16. Seismic profile D-D' spans the northernmost part of the Carmen Basin (CB) **a)** Perspective 3D view of the 40-meter resolution bathymetry, generated in Canvas Xgeo (https://www.canvasgfx.com). **b)** Raw seismic image. **c)** Structural and stratigraphic seismic interpretation. **d)** Interpreted geologic cross-section. The seismic data reveals buried faults beneath sediments, indicating their potential older age compared to the normal faults in the CB. The basement extends along the entire seismic profile at depths between 2.27 and 3.1 s of TWTT (~1700 and 2100 mbsl). It is interpreted that this material is of volcanic origin, evident from seismic reflections exhibiting good lateral continuity and ropey-like high-amplitude features. Notably, a significant seismic feature is a submarine hill toward the NW (Figure 12), suggesting it is the youngest feature of the section.

The shallow sills in this area push the overlying sediments, forming forced folds. The dim area observed across the middle seismic facies may suggest fluid saturation due to lateral migration within the sedimentary cover (Figure 17; Kluesner 2011). Additionally, the shallow sills in the footwall block indicate an oceanic basement of different composition, whereas the Farallon transform fault represents a transition zone, similar to the one observed in seismic

profile DD' (Figure 16), where we mark the transition between younger oceanic crust toward the southern CB to older oceanic crust adjacent to the continental shelf of the Baja California peninsula (Figures 10, 11, 12 and 17).

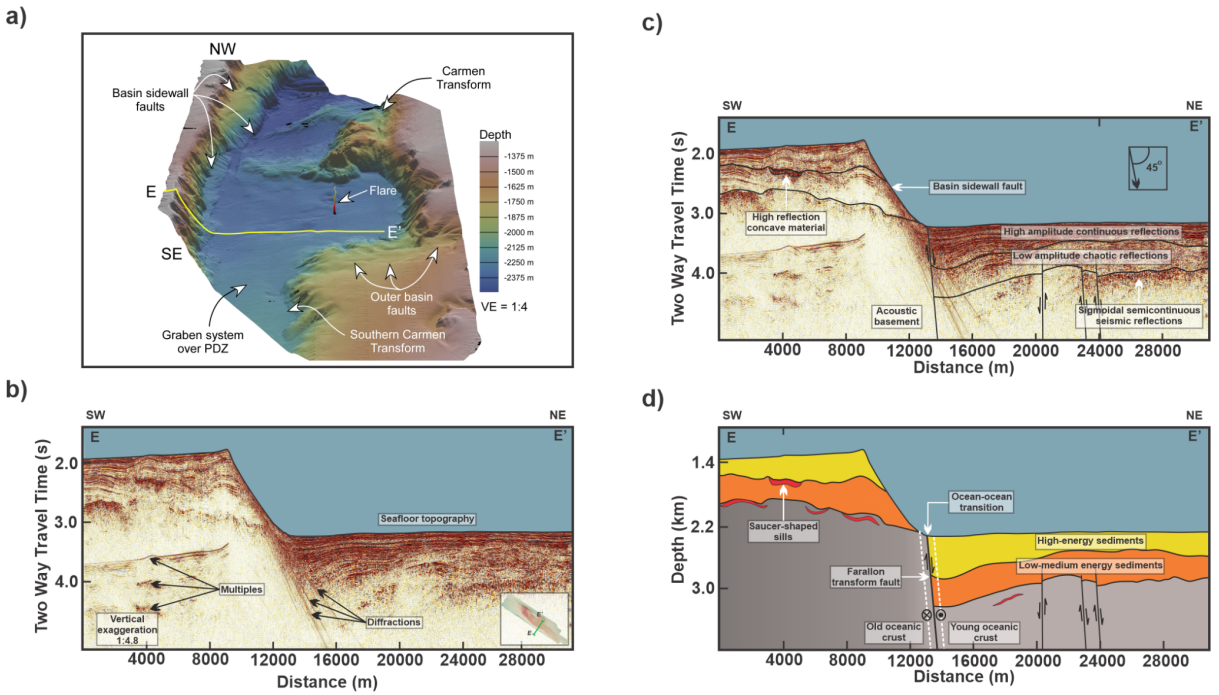

Figure 17. Seismic profile E-E' spans the axial graben of the southern Carmen Basin (SCB). **a)** Perspective 3D view of the 40-meter resolution bathymetry of the SCB, generated in Canvas Xgeo (https://www.canvasgfx.com). Abbreviations: PDZ = principal displacement zone; VE = vertical exaggeration. The flare emerging from the seafloor was imaged using the Interactive Visualization Systems (IVS) Fledermaus 8.4.2 software package (www.qps.nl). **b)** Raw seismic image. **c)** Structural and stratigraphic seismic interpretation. **d)** Interpreted geologic cross-section. The seismic data reveals a steeply dipping Farallon transform fault (Figure 12), which accommodates 0.73 s of syn-tectonic sedimentation. Toward the basin center, sedimentation decreases to 0.67 s-thick (Figure 13). Notably, an uplifted footwall exhibits a tabular-shaped high-amplitude seismic feature spanning ~2 km. This feature is interpreted as a saucer-shaped sill magmatic layer, leading to folding structures within the upper stratigraphic successions (Kluesner, 2011).

Profile FF' is a 22 km-long seismic profile that crosses the southeastern part of the southern CB (Figure 18). It is anticipated that this profile would capture the southeastern extension of the Carmen transform fault. However, the identification of the bounding fault in

this area is challenging and it is unlikely to extend this far to the SE. In map view, the Carmen transform fault bends strongly to the S, forming a releasing bend and splays into a series of normal faults dipping NW that control the SE margin of the southern CB (Figure 12). These faults splay then bend again and become the Southern Carmen fault (Figure 12). Moreover, the overlying seismic stratigraphy in the profile of Figure 18 differs from previous interpretations in other portions of the CB. Here, the seismic stratigraphy is characterized by high-amplitude and laterally continuity reflectors, with cross-bedding structures, indicative of a submarine Gilbert-type fan delta depositional environment (Dorsey et al., 1995).

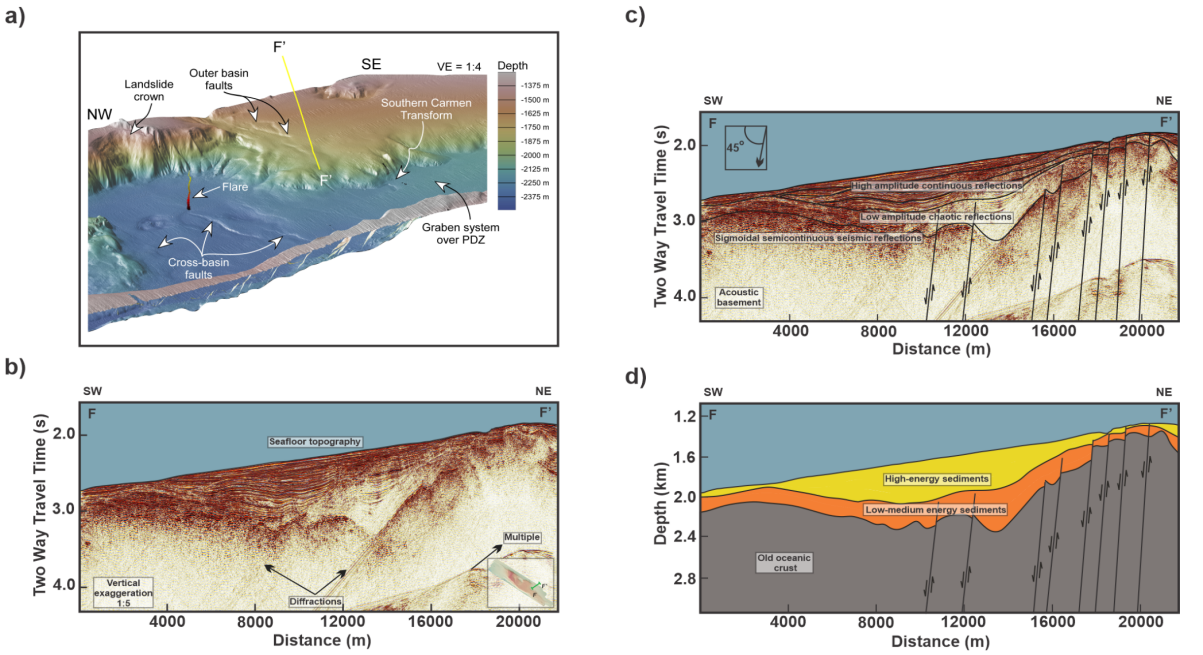

Figure 18. Seismic profile F-F' illustrates the eastern part of the southern Carmen Basin (SCB). **a)** Perspective 3D view of the 40-meter resolution bathymetry of the SCB, generated in Canvas Xgeo (https://www.canvasgfx.com). The flare emerging from the seafloor was imaged using the Interactive Visualization Systems (IVS) Fledermaus 8.4.2 software package (www.qps.nl). **b)** Raw seismic image. **c)** Structural and stratigraphic seismic interpretation. **d)** Interpreted geologic cross-section. The image displays a domino faulting system striking to the SE, accommodating 1.1 s of syn-tectonic strata at the depocenter. In b) and c), the sedimentary pattern reveals distinct seismic facies with inclined cross-bedding and erosion surfaces indicating southeastward deposition. These sedimentary packages potentially represent different facies compared to the sedimentary fills of the Carmen sub-basins, suggesting the presence of submarine fan deposits.

II.5. Discussion

II.5.1. Geometry and timing of rifting in the Carmen Basin

We conducted a comparative analysis between the CB geometry (Figure 12), analog models of pull-apart basins (van Wijk et al., 2017; Wu et al., 2009), and neighboring structures in the southern GC (Figure 19). A first-order observation from Figure 12 is that the CB exhibits a basin morphology controlled by bounding master strike-slip transform fault with a length-to-width ratio of 5:1 According to Mann et al. (1983), rhomboidal-shaped pull-apart basins result from advanced stretching stages, which is more consistent with our observations from the map view analysis presented in Figure 12. Length-to-width ratios increase by this process because the basin width remains fixed, while the extension increases by the offset of the releasing bend.

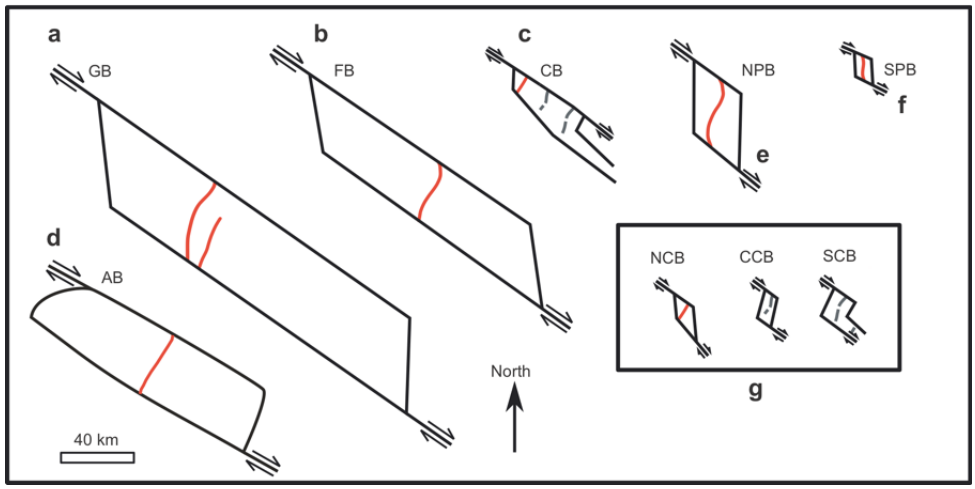

Figure 19. Geometry models of southern basins in the Gulf of California. **a)** Guaymas basin (GB). **b)** Farallon basin (FB). **c)** Carmen Basin (CB). **d)** Alarcon Basin (CB). **e)** Northern Pescadero basin (NPB). **f)** Southern Pescadero basin (SPB). **g)** Northern, Central, and southern sub-basins of the CB. The smaller structures, like the northern CB and NPB, exhibit a rhomboidal geometry, while the larger structures, such as GB and FB, display a rectangular geometry.

Comparing the geometry of the CB (Figure 12) with the neighboring Guaymas and Farallon basins (Figure 19a-c), we observe the latter two basins have a rectangular geometry,

indicating a higher degree of deformation compared to the rhomboidal geometry of the CB (Figure 12; Mann et al., 1983). However, when we compare the geometry of the sub-basins within the CB individually (Figure 10d) with the less evolved Pescadero Basin Complex (Figure 10e-f; Wu et al., 2009; Ramírez-Zerpa et al., 2022), we find that these basins share similar elongated rhomboidal structures with multiple depocenters separated by an intra-basinal highs (Wu et al., 2009; Ramírez-Zerpa et al., 2022; Figure 12). It is worth noting that the boundaries depicted in Figure 19 are speculative and based on limits proposed by multiple authors (Fletcher et al., 2007; Duque-Trujillo et al., 2015; Ferrari et al., 2018; Ramírez-Zerpa et al., 2022). Nevertheless, they provide a reasonable approximation of the geometry for each basin in the southern GC. Similar basin morphologies, such as those observed in the CB and the Pescadero Basin Complex (Ramírez-Zerpa et al., 2022), can also be found in the northern GC basins (Farangitakis et al., 2021), the Vienna basin in Austria, and the Gulf of Eilat in the Red Sea (Wu et al., 2009), where the majority of transtensional deformation occurs along the principal displacement zones.

We now proceed to discuss a simple analysis of the amount of oceanic crust created along the southern GC basins can be derived using basic plate kinematics in relation to the onset of oceanic accretion, assuming a typical spreading rate of 52 mm/yr (Table 2; Figures 19 and 20; DeMets and Dixon, 1999). Basin length is a function of stretching related to strike-slip displacement, and increased displacement leads to an expansion in the width of the fault zone, resulting in broader structures (Gürbüz, 2010). As expected, the larger oceanic basins, such as the Guaymas and Farallon basins, are older than the smaller ones, including the northern CB, central CB, southern CB sub-basins, and the Pescadero Basin Complex (Figure 20). The Guaymas basin exhibits a length-to-width ratio of ~5:1, with a length of ~320 km and a width

of ~65 km. In contrast, the Farallon basin has a length-to-width ratio of 4:1, with a length of ~220 km and a width of ~55 km. The Alarcon basin, on the other hand, shows a similar ratio of ~4:1, with a length of ~187 km, and a width of ~50 km. The length-to-width ratios reported in this work are in good agreement with those reported by Lonsdale (1989). However, they differ slightly from the accretionary oceanic crust lengths reported for the Guaymas (280 km) and Alarcón (135 km) basins by Lizarralde et al. (2007). This deviation may result from a transitional zone between oceanic and continental crust, which appears to be somewhat diffuse. These basins are considered the oldest basins of the entire southern GC, with a timing of rifting between 3.6 and 6.1 Ma (Table 2; Kluesner et al., 2014). In contrast, the northern CB, central CB, southern CB sub-basins, and the Pescadero Basin Complex have length-to-width ratios of ~1:1, with lengths and widths both ~20 km, whereas the axial graben further SW of the southern CB has a length-to-width ratio of ~2:1 (not included in Figure 19 and 20). These sub-basins are regarded as the youngest basins in the southern GC, with ages ranging from 0.4 to 1.3 Ma. In the case of the CB, each sub-basin took 400 Ka to form, while the CB as a whole presents an age of 1.9 Ma (Table 2). Thus, the low length-to-width ratios observed in the CB suggest that these sub-basins are short-lived features within rapidly evolving strike-slip zones (Mann et al., 1983). According to Ferrari et al. (2018), the intra-basin highs (Figures 12 and 14) and the transform fault volcanism (Figures 12, and 16) observed in the CB are interpreted as early Pleistocene seamounts. This interpretation is in good agreement with our estimated timing of faulting and basin formation derived from our analysis in Figures 19, 20, and Table 2.

Table 2. Basin age inferred from length of ocean floor in the southern Gulf of California assuming a spreading rate of 52 mm/yr (DeMets and Dixon, 1999).

Name of the basin	Age (Ma)	Length (km)
Guaymas	6.1	320
Farallon	4.2	220
Carmen	1.9	100
North Pescadero	1.3	70
South Pescadero	0.5	25
Northern Carmen	0.4	20
Central Carmen	0.4	20
Southern Carmen	0.4	20

Moreover, to understand the geologic evolution of the CB, it is also valuable to compare its spreading system with the neighboring Guaymas and Farallon systems. The spreading axes of these systems are wider (2-3 times) than the narrow width (20 km) of the CB (Figures 10-12). Additionally, the adjacent spreading systems have significantly more accreted oceanic crust (320 and 220 km) compared to the CB's 100 km (Table 2). Therefore, for several million years before the existence of the CB, the Guaymas and Farallon spreading systems must have been connected by a segment of the plate margin that was dominated by transform faulting. Based on these relationships, we propose that the CB was created at 1.9 Ma within this transform environment.

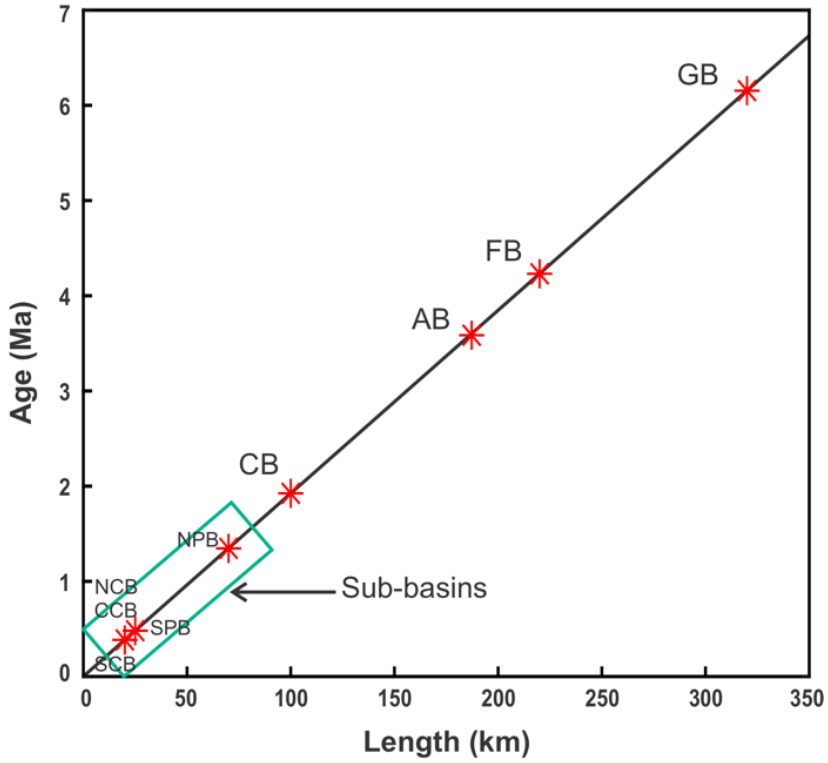

Figure 20. Plot showing the relationship between the onset of seafloor spreading and the length of the accreted ocean crust in different pull-apart basins within the southern Gulf of California (Lizarralde et al., 2007; DeMets et al., 2010; Umhoefer 2011). The plot clearly shows that the time scales linearly correlates to the lenght of the basins (Table 1). Abbreviations: GB = Guaymas basin; FB = Farallon basin; CB = Carmen Basin; NPB = Northern Pescadero Basin; SPB = Southern Pescadero Basin; NCB = Northern Carmen Basin; CCB = Central Carmen Basin; SCB = Southern Carmen Basin.

II.5.2. Crustal lithology and the transition from old to young oceanic crust

In this section, we analyze the lithological composition of the CB basement based on the seismic interpretation derived from Figures 13-18. We further discuss the basin's boundaries to distinguish between old and young oceanic crust and the transition between continental and ocean basement (Figure 21). Our seismic interpretation suggests the CB acoustic basement is composed of highly reflective ropey layers with good lateral continuity, similar to those found in neighboring basins. These layers have been identified as basaltic lava flows and intruded sills

within sedimentary deposits, as found in collected rocks in the axial graben of the northern Carmen basin (Figure 15), and adjacent Farallon and Guaymas basins (Piñero-Lajas, 2008; Lizarralde et al., 2007; Kluesner, 2011). The basement rocks outcrop widely along the three sub-basins of the CB, the spreading center, and the structural highs, forming at least ~80 km of newly formed oceanic crust (Figures 13-18). In Figure 21, we identify three distinct segments of oceanic crust according to their estimated formation age (Figures 19, 20, and Table 2). Two things are noteworthy in Figure 21. (*i*) The eastern transition between continental and oceanic crust is delimited at the Sonora and Sinaloa continental shelf border by a series of en-échelon scarps juxtaposing continental and oceanic crust (Figures 10, 11 and 21). By contrast, the transition along the western and southwestern basin margins is defined by a series of rotated blocks within a low-angle faulting system along the Baja California continental shelf border, as revealed by previous studies (Bot et al., 2016; Macias-Iniguez et al., 2019). And (*ii*), the CB separates the Guaymas and Farallon basins through an oceanic-oceanic crustal boundary. Cross-cutting and structural relations indicate that the Carmen transform fault and Farallon transform fault bounding the CB are younger than the oceanic crust along the inner margins of the Guaymas and Farallon basins (Figures 19, 20 and Table 2).

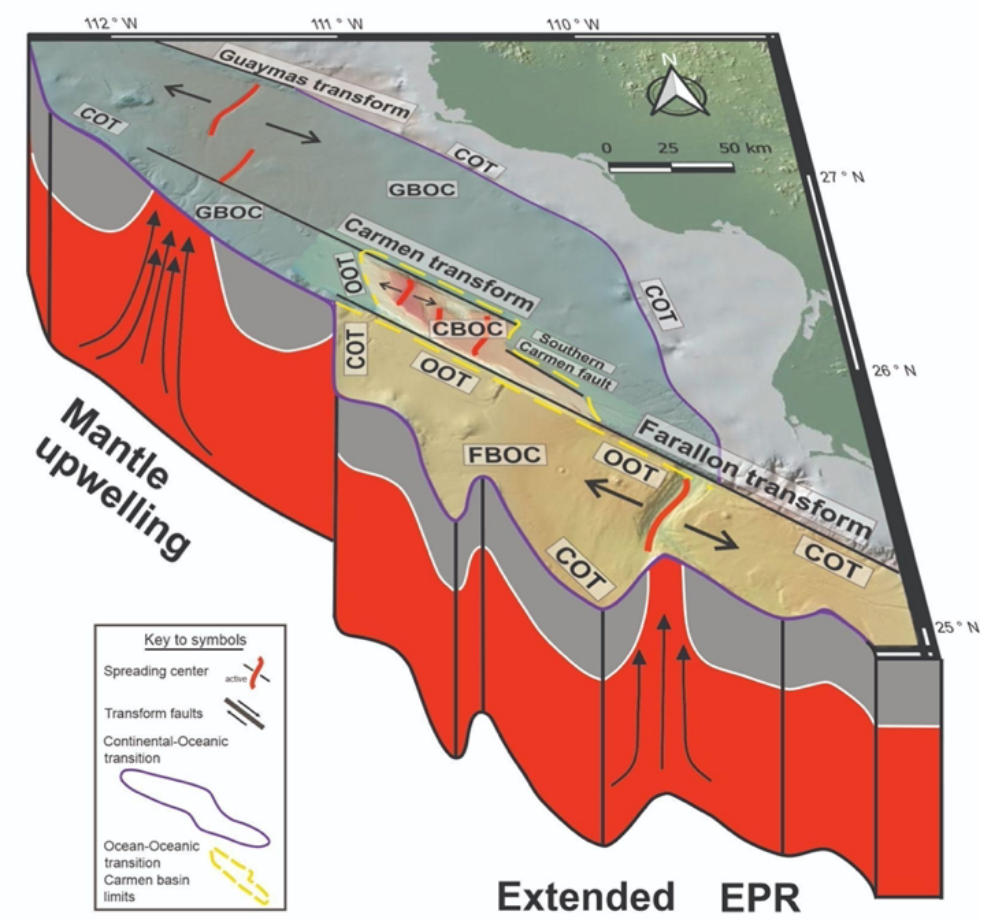

Figure 21. Regional map illustrating the crustal boundaries of the Guaymas, Carmen, and Farallon basins. The oceanic crust of the Guaymas basin is highlighted in light green, while the CB is represented by the bathymetric data from the multi-beam survey (40-m resolution; Figure 3). The Farallon basin is highlighted in light yellow. The dotted yellow line indicates the transition from old oceanic crust (late Miocene for the Guaymas basin and early Pliocene for the Farallon basin; Lizarralde et al., 2007; DeMets et al., 2010; Umhoefer, 2011) to young oceanic crust (early Pleistocene for the Carmen basin; Table 1). The purple line marks the boundary between continental and oceanic crust. Abbreviations: CBOC = Carmen basin oceanic crust; COT = Continental-oceanic transition; FBOC = Farallon basin oceanic crust; GBOC = Guaymas basin oceanic crust; OOT = Oceanic-oceanic transition. The schematic cross-section model is based on interpretations by Gregg et al. (2007), Wang et al. (2009) and Di Luccio et al. (2014). The cartoon depicts the dynamic upwelling of the mantle at the mouth of the Gulf of California as an extension of the East Pacific Rise (EPR), which facilitates the formation of new oceanic floor.

According to Polteau et al., (2008), saucer-shaped intrusions form when a buoyant sheet of rising melt, driven by magmatic pressure from a magma source, exceeds the pressure exerted

by the surrounding sediment. The seismic profiles across the CB reveal concave, high-reflection material interpreted as saucer-shaped igneous sills (Kluesner, 2011). These magmatic intrusions have varying lengths but average diameters of 1-2 km (Figure 17). They are associated with overburden deformations, fluid migration through faults, and potential feeder networks (Kluesner, 2011; Negrete-Aranda et al., 2019, 2021; Sarkar et al., 2022; Figures 13, 15, and 17). These shallow sills are observed within a young oceanic crust, representing sites of magmatic crustal accretion in the actively growing basin (Figures 13 and 15). Kluesner et al. (2011) reported that the sill located southwest of Farallon Transform spans a length of 2 km, with a thickness of 280 m, and features sharply upturned tips buried ~340 m of sediments (Figure 17). Formation of sediment-sill complexes, which involve the intercalations of igneous sills and sedimentary rocks, has been observed in both the central Guaymas basin and southern Farallon basin (Piñero-Lajas, 2008; Kluesner, 2011; Lizarralde et al., 2011; Sarkar et al., 2022). Thus, Kluesner (2011) suggests that the geometry of sills in the Gulf of California, as derived through finite element modeling, is predominantly influenced by factors such as the depth of emplacement, displacement, and deformation of the overlying strata.

II.5.3. Kinematics of transform faults and spreading center instabilities in the Carmen basin

In the southern GC, cross-cutting relations suggest that the formation of the CB occurred after seafloor spreading initiated in the Farallon and Guaymas basins. Kinematic instability of the bounding faults led to the propagation of the Carmen transform fault and the Farallon transform fault, eventually forming the CB (Figures 19, 21, and Table 2). A possible mechanism determining the stability of this family of boundaries is the pooling of erupted lavas observed in topographic lows within the transform fault domain (e.g., Carmen transform fault; Figure 12).

According to Gregg et al. (2007), this *leaky* magmatic accretion results from the presence of intermediate-fast-slipping transform faults, a configuration frequently observed at the East Pacific Rise, where basaltic lavas indicate crustal accretion within the transform fault region, as seen in the Garret and Siqueiros transform faults. Gregg et al. (2006, 2007) also suggest that an intra-transform spreading center is a series of fault lines offset by short ridges. These features facilitate active seafloor spreading, resulting in crustal accretion.

In the case of the CB, our proposed model in Figure 21 is consistent with the interpretations by Gregg et al. (2007); Wang et al. (2009); and Di Luccio et al. (2014). According to this model, the fast rifting in the southern GC is driven by mantle upwelling, leading to the formation of new oceanic spreading centers connected by intermediate-fast slipping transform faults, including the Carmen transform fault and the Farallon transform fault (Figure 12). These observations align with the cross-sectional features presented in Figure 21, which depict the extended East Pacific Rise, as well as mantle upwelling patterns similar to those found in tomography studies by Wang et al. (2009), Zhao (2004), Di Lluccio (2014). According to Wang et al. (2009), the current configuration of the main spreading center system in the Wagner, Delfin, and Guaymas basins is influenced by partially melted mantle pockets spaced ~250 km apart. Furthermore, Di Luccio et al. (2014) have observed slow anomaly asthenosphere upwelling beneath the Pescadero basin and Alarcon basin in the southern GC.

To explain the development of the CB, we also follow the model proposed by Sims et al. (1999). The idea is that transform faults can evolve from strike-slip to normal-oblique, creating a network of sub-basins above a thin, ductile basal décollement. The domino faulting system observed toward the northern CB (Figures 11 and 16) suggests the presence of a SW-directed detachment surface. This configuration allows magma intrusion through crustal

thinning and mantle upwelling, resulting in volcanic and intrusive features along the Farallon transform fault (Figures 11 and 12; Kusznir and Karner, 2007). This process may lead to the development of a hinge zone, northwest of the northern CB, near the structural high interpreted as a young mud volcano in Figure 16, similar to the 20° N Basin along the Owen Fracture Zone in the NW Indian Ocean (Rodriguez et al., 2013). These observations are also consistent with the wide distribution of east and west-directed low-angle normal faults along the GC (González-Fernández et al., 2005; Martín-Barajas et al., 2013; Macias-Iñiguez et al., 2019), where faults are believed to contribute to more efficient stretching and plastic rebound of the underlying lithospheric mantle, leading to the formation of metamorphic core-complexes associated with regional rolling-hinge structures (Fletcher and Spelz, 2009). Comparable structural systems can also be observed in bathymetric data of the Mid-Atlantic Ridge, where core complexes associated with basal detachments and normal faulting parallel to the ridge axis develop (Howell et al., 2019).

The CB consists of three spreading centers within the same plate-margin segment, indicating significant instability in the localization of the spreading process. These spreading centers form sub-basins with increasingly advanced pull-apart geometries from south to north (Figures 13, 14 and 15). Lithospheric strength plays a crucial role in strain localization, and compositional and thermal heterogeneities in the upper mantle are likely to have significantly influenced the positioning of spreading axes. Seismic tomography conducted by Wang et al. (2009) and Di Luccio et al. (2014) revealed areas of robust upwelling with low-shear velocity near the more stable Guaymas and Farallon spreading systems. However, it is worth noting that these mantle anomalies are offset toward the east compared to the surface trace of these spreading systems as shown in mantle tomography studies made by the same authors. Moreover,

Fletcher et al. (2007) proposed that the anomalous upper mantle associated with the paleo East Pacific Rise, west of the Baja California microplate, likely continued to be overridden by western North America following the middle Miocene ridge-trench collision, which marked the onset of rifting in the proto-GC. This would explain why the centers of anomalous mantle are situated east of the Guaymas and Farallon spreading axes, suggesting that the passage of the CB over thermally and compositionally heterogeneous mantle could have contributed to the observed instabilities in strain localization. The middle Miocene ridge-trench collision was also accompanied by the opening of a deep slab window beneath the proto-GC (Fletcher et al., 2007), generating additional compositional and thermal anomalies in the upper mantle.

Another factor that strongly controls strain localization is the distribution of applied tectonic loads along the plate margin. Fletcher et al. (2007) proposed that the Baja California microplate, along with its underplated Farallon-derived microplates, became welded to the Pacific plate across the paleo East Pacific Rise. Consequently, the asthenospheric window beneath the GC continues to widen due to the northwestward drift of the Pacific plate along the trailing edge of the western limit of the Baja California microplate, which has been shown by Di Luiccio et al. (2014) to coincide with the western limit of the Farallon slab at depth. Thus, the northwest migration of the spreading axes that we have documented in the CB may be a function of the northwest migration of applied tectonic loads.

II.6. Conclusions

By examining the seafloor morphology and the seismic structure at depth of the CB, we gain insights into the deformation process at a small scale. The development of three sub-basins with contrasting morphologies suggests progressive strain from the southern CB toward the

northern CB, where the current spreading center is located. This pattern indicates that the sub-basin system formed at different geologic times due to rapid extension, resulting in the abandonment of the southern sub-basins and the establishment of the current spreading center in the northern sub-basin. Our findings also suggest an estimated age of ~1.9 Ma, indicating that, despite being a young structure, the basin has reached a level of maturity similar to those found in oceanic basins. Furthermore, based on our comparative geometric analysis with analog models and other natural examples of pull-apart basins, we propose that the CB is a product of transtensional deformation rather than pure strike-slip extension.

Despite variations in the predicted degree of basin evolution according to different models, the current stage of the CB appears to mark the transition between crustal thinning and the eventual oceanic crust rupture, creating spreading centers and generating new oceanic crust. The seismic interpretation reveals an acoustic basement consisting of volcanic rocks, indicating the development of a new oceanic floor across the CB. Variations in basin bathymetry suggest the juxtaposition of different materials, with structural highs representing either a crystalline basement or indicating late Miocene-to-early Pleistocene volcanic activity. The oceanic crust of the CB is bounded by major basin sidewall faults, exhibiting magmatic activity along the transform faults connecting the Guaymas and Farallon basin oceanic crusts. This magmatic accretion indicates intermediate-fast-slipping fault propagation separated by a segment of intra-transform spreading center, resembling the extensional dynamics of the East Pacific Rise toward the mouth of the GC.

Depositional relations and cross-cutting correlations in the seismic stratigraphy indicate that CB formation began in the southern CB. Sediment thickness decreases systematically from the southern CB to the northern CB, indicating strain localization and spreading center

instabilities within the CB. The extended East Pacific Rise beneath the GC influences the relocation of spreading axes, favoring areas with thinner, fractured crust. This kinematic setting explains the sequential abandonment of sub-basins and their fossil spreading centers in the southern and central CB, ultimately leading to the active spreading center in the northern CB. Further north, near the active volcanism of the Carmen transform fault, the development of mud volcanoes could drive the migration of a future spreading center.

III. CRUSTAL STRUCTURE AND TECTONIC HISTORY OF FARALLON BASIN, SOUTHERN GULF OF CALIFORNIA

III.1. Introduction

In the southern GC (Figure 4 and 10), the Gulf Extensional Province is intimately related to low-angle normal faulting and simple shear domains that accommodate a significant component of crustal extension along the San Juan de Los Cabos and San Juan de Los Planes faults (Fletcher et al., 2000; Fletcher and Munguía, 2000; Fletcher et al., 2003; Bot et al., 2016; Macias-Iñiguez et al., 2019). It is generally thought that deformation at these margins is controlled by a series of master low-angle normal fault systems along which the tectonically unloaded lower plate rebounds isostatically, forming an antiformal bulge that migrates in the direction of displacement of the upper plate (e.g., Buck, 1988; Wernicke and Axen, 1988; Lavier et al., 1999; Fletcher and Spelz, 2009). Moreover, worldwide observations indicate that the spreading rate of a rift zone plays an essential role in the mid-ocean ridge morphology and core-complex accretion (e.g., Buck, 1993). Hence, slow-spreading mid-ocean-ridges segments show buoyant mantle upwelling and melt migration focused beneath the centers of ridge segments, whereas fast-spreading mid-ocean ridges reflect more uniform mantle upwelling beneath the ridge axis (Kuo and Forsyth, 1988; Lin et al., 1990; Escartin and Lin, 1995; Canales et al., 2000, 2003; Gregg et al., 2006, 2007).

Notwithstanding all the recent progress in understanding the rifting dynamics of the northern GC rift basins (e.g., Aragón-Arreola et al., 2005; González- Fernández et al., 2005;

Aragón-Arreola and Martín-Barajas, 2007; Lizarralde et al., 2007; Gonzalez-Escobar et al., 2010; Contreras-Pérez et al., 2012; Martín-Barajas et al., 2013), significant research work is still needed before a detailed evolutionary picture of the entire gulf is produced. It is especially true for the central and southern gulf basins in which data is lacking or has poor spatial/temporal resolution. Thus, our proposal will help to narrow this information gap and bring much needed detail into the geological history of the southern part of the GC.

Our work rests on the conjecture that the early stages of continental rupture are controlled by pure shear deformation resulting in symmetrical basins (McKenzie, 1978) that are subsequently abandoned at the margins of the rift. This gives way to simple shear deformation that led to asymmetrical basins (Figure 22) (Wernicke, 1981, 1985). Tectonic transport along a master detachment fault system (e.g., González-Fernández et al., 2005; Martín-Barajas et al., 2013; Macias-Iñiguez et al., 2019) causes the underlying lithospheric mantle to stretch and rebound plastically, resulting in the formation of metamorphic core complexes associated with regional rolling-hinge structures (e.g., Wernicke and Axen, 1988; Lavier et al., 1999; Fossen, 2010). As the lithosphere continues to thin, the relative proportion of horizontal to vertical deformation in the upper levels of the crust increases, whereas the pressure in the hot asthenosphere below decreases. This decompression causes partial melting, which results in the volcanic activity along the rift. Elevated heat flow, coupled with progressive deformation, causes the lithosphere to break apart, forming spreading ridges and new oceanic crust associated with mantle convection (Watts et al., 2009; Fossen, 2010).

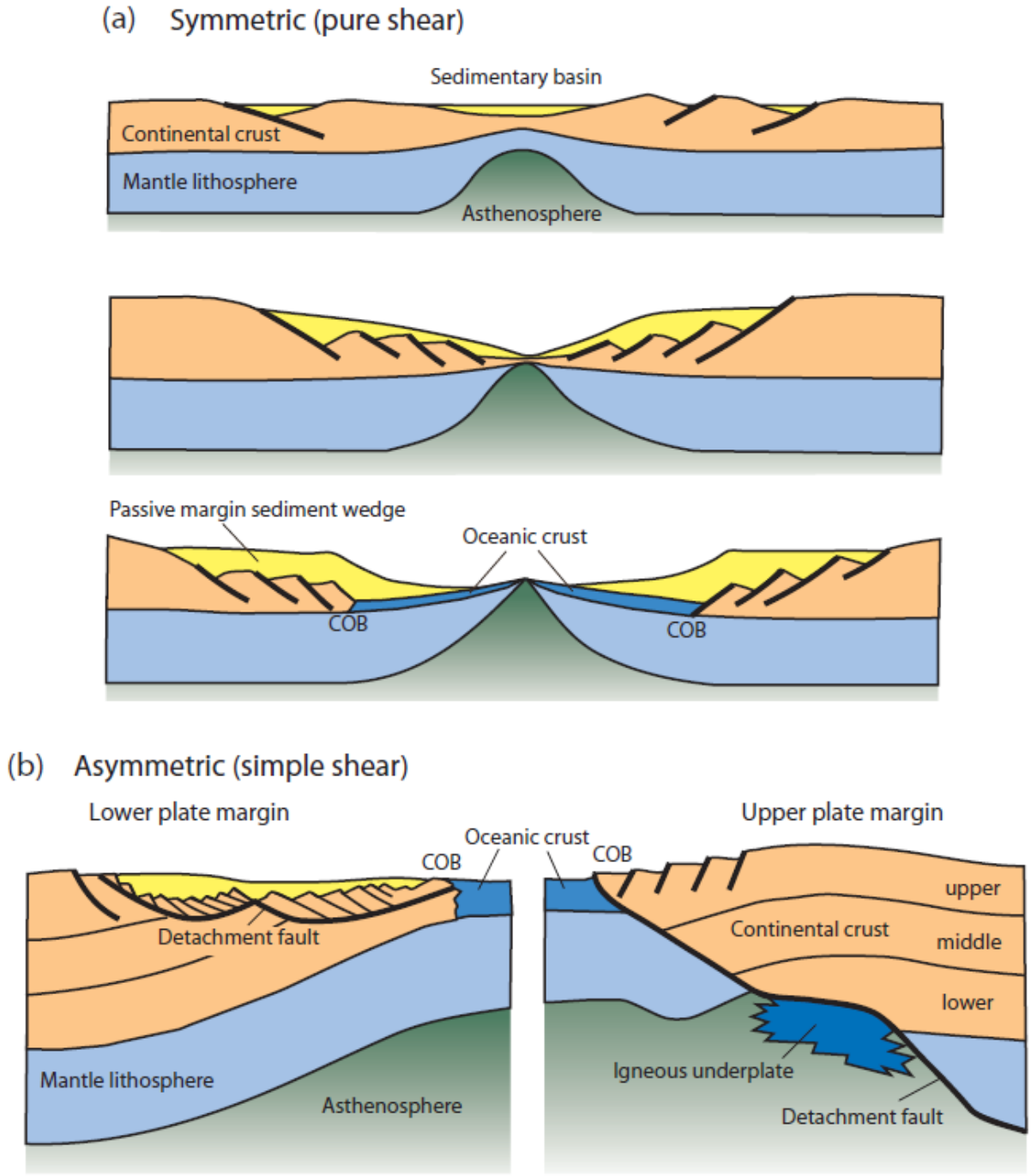

Figure 22. Conjugate margins based on deep seismic data (from Allen and Allen, 2013). a) Symmetric margin (pure shear), and b) asymmetric margin (simple shear) with a lithospheric detachment fault. COB stands for continent-ocean boundary.

The crustal thinning associated with the opening of the GC, coupled with recent volcanic activity and rapid sedimentation, provides ideal conditions for the development of hydrocarbon fields (e.g., Tiburon basin; Figure 4; Contreras-Pérez et al., 2012), and geothermal systems (e.g., Guaymas, Farallon, Pescadero, and Alarcon basins; Figure 10; Neumann et al., 2017; Paduan et al., 2018; Negrete-Aranda et al., 2019, 2021). Moreover, the assessment of the thermal state of the Baja California peninsula, particularly the GC, is strategically important for Mexico since it includes areas with major geothermal anomalies (e.g., Negrete-Aranda et al., 2021; Peña-Dominguez et al., 2022). The thermal state of the southern GC has been documented using recent heat-flow surveys in the pull-apart basins (e.g., Prol-Ledesma et al., 2013; Neumann et al., 2017; Negrete-Aranda et al., 2021; Peña-Domínguez et al., 2022). These surveys have reported anomalously high heat-flow values, in some cases exceeding the average heat flow of the oceanic crust by an order of magnitude (Neumann et al., 2017; Negrete-Aranda et al., 2021 and Peña-Domínguez et al., 2022).

Extensive hydrothermal investigations in the central and southern regions of the GC, including the Guaymas, Farallon, and Pescadero basins (Figure 10), have provided valuable insights through the interpretation of seismic reflection data, heat flow measurements, and the collection of sediment core and rock samples (e.g., Piñero-Lajas, 2008; Kluesner, 2011; Kluesner et al., 2014; Negrete-Aranda et al., 2019; Sarkar et al., 2022). These studies have revealed the presence of hydrocarbon-fluid vents, forming distinctive seafloor structures and subsurface gas hydrates. These features are favorable for extensive methane capture in a solid, ice-like compound known as methane hydrate, which develops in marine organic-rich sediments under high-pressure and low-temperature conditions (e.g., Sarkar et al., 2022). In the southern Farallon basin (Figure 10), a stratigraphy-crosscutting Bottom Simulating Reflection (BSR) has

been interpreted as methane hydrates (Piñero-Lajas, 2008), exhibiting high-amplitude seismic reflections parallel to the seafloor (Berndt et al., 2004; Dewangan et al., 2021). Conversely, Sarkar et al. (2022) observed methane hydrate BSRs with reversed polarity seismic reflections in the Guaymas basin's off-axis regions (Figures 4 and 10), associated with chimneys and pockmarks that serve as conduits for the gas (Lonsdale, 1985). Heat flow measurements conducted by Negrete-Aranda et al. (2019) in the Auka and JaichMaa Ja'ag' hydrothermal vent fields in the southern Pescadero basin (Figure 10) further revealed hydrothermal circulation along graben-bounding faults, characterized by fast vertical flow in fault zones and slow horizontal flow in sedimentary layers. They also identified deep-seated hydrothermal sources ~5 km below the seafloor.

In this study, we construct a regional geological framework of the Farallon basin (Figure 6 and 10), in the southern part of the Gulf of California, from high-resolution bathymetry collected by the Schmidt Ocean Institute in 2021 and 2D seismic reflection data collected by CICESE in 2006 (Figure 6). Here, we characterize the geometry and structure of the Farallon basin to identify the different stages of crustal deformation, interpret the basement lithology, and describe the seismic stratigraphy and the magmatism that might be associated with the formation of geothermal fluids (e.g., Kluesner et al., 2014; Negrete-Aranda et al., 2021). Then, we contrast our results with other pull-apart basin geometries in the southern GC. We further discuss the transition between the continental and oceanic crust and propose the role of strike-slip faulting in a highly oblique-divergent setting associated with crustal thinning, active magmatism and oceanic accretion.

III.2. Geological setting

The GC is the result of an oblique extension process that separated the Baja California peninsula from the northwestern part of Mexico's mainland during the Miocene. The GC structure is characterized by a series of pull-apart basins connected by a right-stepping strike-slip master fault system, which together define the plate boundary between the Pacific and North America in a NW-SE direction. In areas where transform faults overlap, spreading centers are formed orthogonally to the main gulf axis, leading to the accretion of new oceanic lithosphere (e.g., Lonsdale, 1989; Sutherland et al., 2012; Duque-Trujillo et al., 2015).

Different theories have been proposed for the tectonic evolution of the GC (Figure 1). The two-phase kinematic model (e.g., Stock and Hodges, 1989); Henry and Aranda-Gomez, 2000; Aragon-Arreola and Martín-Barajas, 2007), suggests two deformation zones at each side of the Baja California microplate accommodated the relative motion between the Pacific and North American plates at distinct times (~12 to 6 Ma and ~6 to 0 Ma) (Stock and Hodges, 1989; Henry and Aranda-Gómez, 2000; Oskin and Stock, 2003; Aragón-Arreola and Martín-Barajas, 2007; Darin et al., 2016; Balestrieri et al., 2017). In contrast, the single-phase model (e.g., Fletcher et al., 2007) suggests that the two deformation zones simultaneously sheared the Baja California peninsula from western mainland Mexico at ~12 Ma. Despite their wide acceptance, these first-order models fail to explain crustal thinning and magmatic activity in the GC. Hence, it is necessary to incorporate the fundamental concept of strain into these kinematic models (Allen and Allen, 2013). That is, as the extensional strain increases, the injection of magma through the upper crust is facilitated by crustal thinning and upwelling of the mantle forming volcanic and intrusive geometries.

Within this tectonic framework, significant geothermal fields can develop, as exemplified by the Baja California peninsula, which hosts the world's second-largest geothermal field (Cerro Prieto), as well as two of the six major geothermal fields in the country (Cerro Prieto and Tres Vírgenes). It also includes three major geothermal areas on its central portion (Los Volcanes, Santispac and Agua Caliente) (Santoyo-Gutierrez and Torres-Alvarado, 2010).

III.3. Methodology

III.3.1. Seismic Data processing

The processing of seismic data involves applying a series of algorithms to field data, forming a three-stage workflow to produce an image of the subsurface structure: pre-stack, stack, and post-stack (Sheriff and Gerald, 1983; Yilmaz, 2001). This work-flow allows to: (i) extract the frequencies of interest in the seismic data, mitigate multiples and equalize the amplitudes of the signal; (ii) improve the signal-to-noise ratio; and (iii) correct the trajectories of seismic rays, ensuring the signal is accurately positioned, and to attenuate the spurious effects produced during each processing stage. The details about seismic data processing can be found in the methodology chapter of this thesis (Figures 7-9). For this work, we processed ~295 km of seismic data in the Farallon basin, and reinterpreted ~314 km from Piñero-Lajas (2008) (Figure 6).

III.3.2. Seismic Interpretation

The seismic interpretation is defined as the geophysical information derived from seismic reflection profiles, based on the continuity or variability of reflections, the seismic characteristic, and the internal geometry, to identify geological structures, stratigraphic changes,

and the presence of fluids, among other geological features (Badley, 1985). Key features in this work are primary structures such as fault planes, folds, grabens, and semi-grabens. Parameters such as fault length and dip, stratal lengths and thicknesses, and subsidence can be quantified. Another essential aspect is the mapping of seismic reflectors, such as the limits of sedimentary sequences (e.g., maximum flooding surfaces and erosion surfaces, among others). Moreover, from their seismic attributes, it is possible to identify with certainty the likely lithology of the sedimentary material. Magmatic injections associated with geothermal fluids can be interpreted as a mosaic of high-reflectance surfaces (e.g., saucer-shaped sills; Polteau, 2008) and low-reflectance surfaces (e.g., dim spots; Chopra and Martfurt, 2007).

III.4. Results and discussion

III.4.1. Geomorphology and 2D architecture of Farallon Basin

An analysis of 40-meter resolution bathymetry data has provided us with new insights into the geological details and structural descriptions of the entire Farallon basin, revealing the oblique-rifting processes in the southern GC from a three-dimensional perspective (Figure 23). The Farallon basin is located between the Carmen basin in the northwest and the Pescadero basin in the southeast of the GC. The basin measures ~220 kilometers in length, and 50 kilometers in width, resulting in a length-to-width ratio of 4:1, as shown in Figure 23. The structural configuration and architecture of the Farallon basin are governed by the interaction of two right-lateral, right-stepping master fault system with varying extents of separation and overlapping (Figure 23): the Farallon transform fault to the northeast, and the Atl transform fault to the southwest (Figure 23). There are two sub-parallel principal displacement zones oriented to the northwest, influencing the northeastern and southwestern boundaries of the Farallon

basin. The Farallon transform fault in the northeast extends over a distance of 200 km, and the Atl transform fault spans ~130 km propagation towards the southwest (Figure 23). These bounding zones overlap and connect through a transverse system of en-échelon oblique-extensional normal faults, creating one distinct basin with a single depocenter.

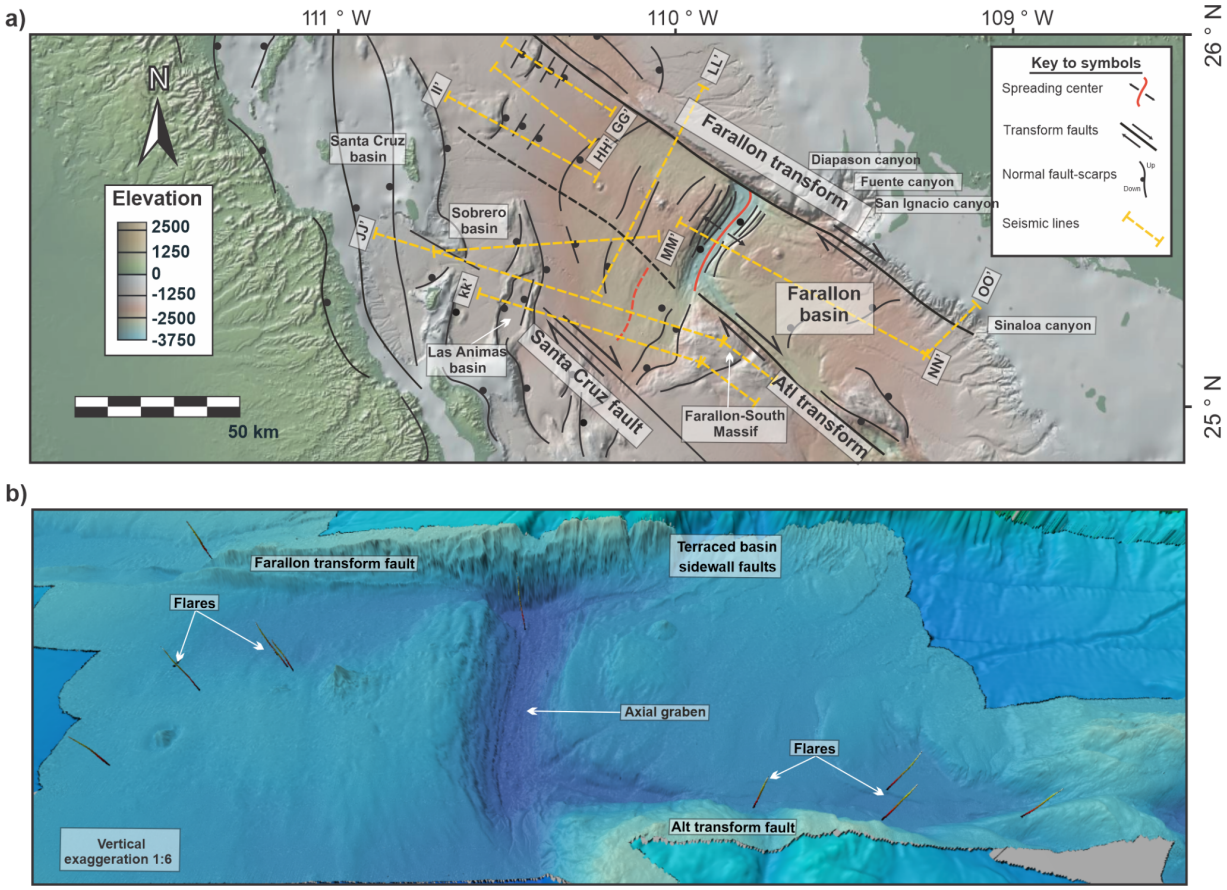

Figure 23. a) Structural map of the Farallon basin illustrating the two-dimensional architecture and geometry (http://www.geomapapp.org). **b)** High-resolution (40-m) bathymetry is imaged using the Interactive Visualization Systems (IVS) Fledermaus 8.4.2 software package (www.qps.nl).

The bathymetric data of the Farallon basin indicates notable uplift of the footwall along the outer margin, particularly along the path of the transform faults. This nearly vertical uplift is managed by a series of segmented, diagonal, basin-sidewall faults that have developed on

both the Farallon transform fault and the Pescadero transform fault, as depicted in Figure 23. The Farallon basin's margins are defined by bathymetric escarpments that face the inside of the basin. These escarpments can be easily identified in seismic profiles, as described below, and correspond to the abrupt shift from highly attenuated continental lithosphere to recently accreted oceanic lithosphere. Along the Farallon transform fault, gravitational instabilities develop, leading to rapid and episodic slumping and grain flows, forming distinct cliffs with landslide crowns and scarps beside this steep transform fault (Figure 23). Yet, the primary sediment routing system for infilling the Farallon basin appears to be a submarine dendritic drainage system originating from the tips of the principal displacement zones and from the western margin of the Sinaloa continental shelf where inputs of sedimentation are observed throughout the submarine canyons (Figure 23).

Figure 23 reveals a cross-basin fault system that propagates obliquely to the principal displacement zones. This fault system induces a left-stepping arrangement of synthetic Riedel shear faults (e.g., Christie-Blick and Biddle, 1985; Wu et al., 2009) that curve into an elongated sigmoidal shape, connecting the sidewall faults at both sides of the basin. The resulting depocenter occurs in the central portion of the basin and is bounded longitudinally by oblique-normal faults segments. This structure acts as a connection between the bounding Farallon transform and the Atl transform faults. The depocenter is the deepest part of the basin located at a depth of ~3,200 m. It has a length of ~36 km and a width of ~13 km. The depocenter hosts the current seafloor spreading center featuring a short and narrow axial graben oriented sub-perpendicular to the principal displacement zones, and it is bounded by escarpments on both the northwestern and southeastern sides (Figure 23). In plan view, the axial graben divides the basin into two zones, one to the northwest and the other to the southeast. The western margin of the

Farallon basin consists of an escarpment over 300 m high that is due to the San Martin fault. The depth to the west of the margin remains above the 1000 m isobath and is characterized by a large number of islands and sub-basins, including Santa Cruz, Sobrero and Las Ánimas (e.g., Piñero-Lajas, 2008). The eastern margin, unlike the western margin, is made up of a much steeper escarpment (over 1000 m) associated with the Farallon transform fault and a series of canyons which begin on the continental platform at the mouth of the Fuerte river. They are the Diapasón, Fuerte, and San Ignacio canyons. The Sinaloa canyon further south has an escarpment of more than 1300 m, where the slope is cut by submarine canyons that act as channels for sediment transport. Also, unlike the western margin, the eastern margin does not host islands or other sub-basins. Towards the center of the basin, in the western zone, there are seamounts above the 1100-meter depth, which are related to the Farallon Sur massif. The abandoned area of the Farallon basin axis, or Farallon Sur axis, with a depth of around 2500 m, is identified as the Farallon-South Massif that delimits the Farallon basin in its western part. It is a volcanic complex, divided into two main mounds (Figure 23) with small eruptive centers on top.

III.4.2. Seismic interpretation of the Farallon Basin

In this section, we present a network of 9 seismic profiles that extend across the Farallon basin and across the submerged continental crust of the Baja California peninsula, for a total of ~609 km of seismic data. Profiles GG', HH' are oriented subparallel to the Farallon transform fault, and profiles II', NN' cross the main axis of Farallon basin, which are subparallel to relative plate motion. MM', JJ' and KK' are oriented northwest, which are obliques to the transform faults and to the relative plate motion. Profiles LL' and OO' are perpendicular to the Farallon transform fault and are oriented northeast, which are sub perpendicular to relative plate motion.

The seismic interpretation of lines GG'-OO' (Figures 24-32), in conjunction with the morphological analysis presented in Figure 23, provide new insights into the structural evolution of the CB. On a broader scale, the Farallon basin displays three distinct seismic facies (Figures 24-32). Proceeding from the bottom to the top of the seismic sections, at a larger scale, the Farallon basin exhibits three distinct seismic facies following the same pattern of Guaymas basin (Kluesner et al., 2014) and Carmen basin (Julià-Miralles et al., 2024). The first seismic facies is interpreted as the acoustic basement, characterized by reflective, ropey-like layers with sigmoidal, semi-continuous reflections and strong lateral coherence. These rocks are interpreted as volcanic flows with a depth range from 2.5 TWTT to 4.5 TWTT. The two seismic facies overlying the acoustic basement represent sedimentary layers filling the basin. The underlying facies consist of sequences with alternating medium and low-energy chaotic reflections, resembling accumulations of inter-glacial diatomaceous muds. The overlying facies consist of sequences with alternating medium and high-energy coherent reflections, displaying diatomaceous mud and sand turbidites deposited in a high-energy environment (Kluesner, 2011; Kluesner et al., 2014).

Profile GG' spans ~45,7 km. It was collected parallel to the Farallon transform fault on the western side of the Farallon basin with a length of 200 km. Furthermore, the profile GG' exhibits a faulted crust that is inclined towards the northwest, identified as oceanic crust, descending from the primary bounding fault escarpment (Figure 24). The back-tilted crust has subsequently been covered by a thick section of low-energy chaotic reflections, resembling accumulations of inter-glacial diatomaceous muds that have filled in and sequences with alternating medium and high-energy coherent reflections, displaying diatomaceous mud and

sand turbidites deposited in a high-energy environment, resulting in a relatively smooth basin floor (Figure 24).

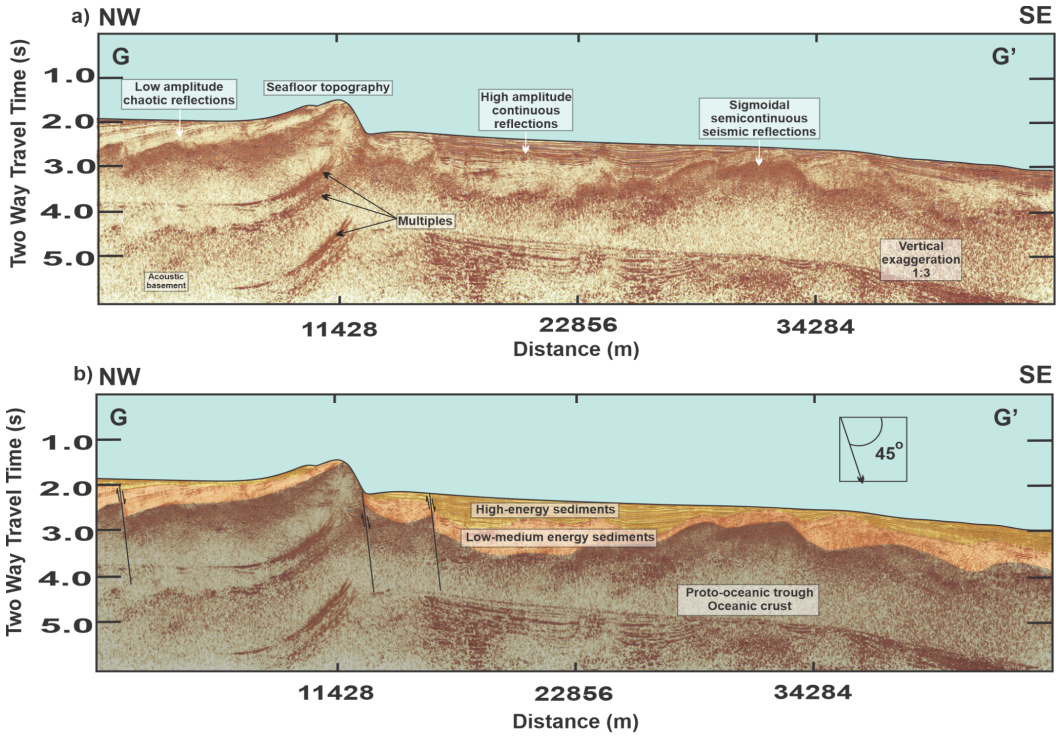

Figure 24. Seismic profile G-G' collected parallel of Farallon Transform fault on the northwestern Farallon basin. **a)** Raw seismic image and structural, stratigraphic seismic interpretation. **b)** Interpreted geologic cross section.

Profile HH' has a length of ~ 45,9 km. It is located west of Profile GG' transects the center of western Farallon basin with a length of and displays similar basin structure of GG' profile, except that high reflections concave material interpreted as sills are more extensive and the lower section of the sediment cover is acoustically dim. Low-amplitudes chaotic reflections are most likely due to gas concentrations within the sediments, whereas high-energy coherent reflections are interpreted as diatomaceous mud and sand turbidites deposited in a high-energy environment covering the seafloor basin (Figure 25).

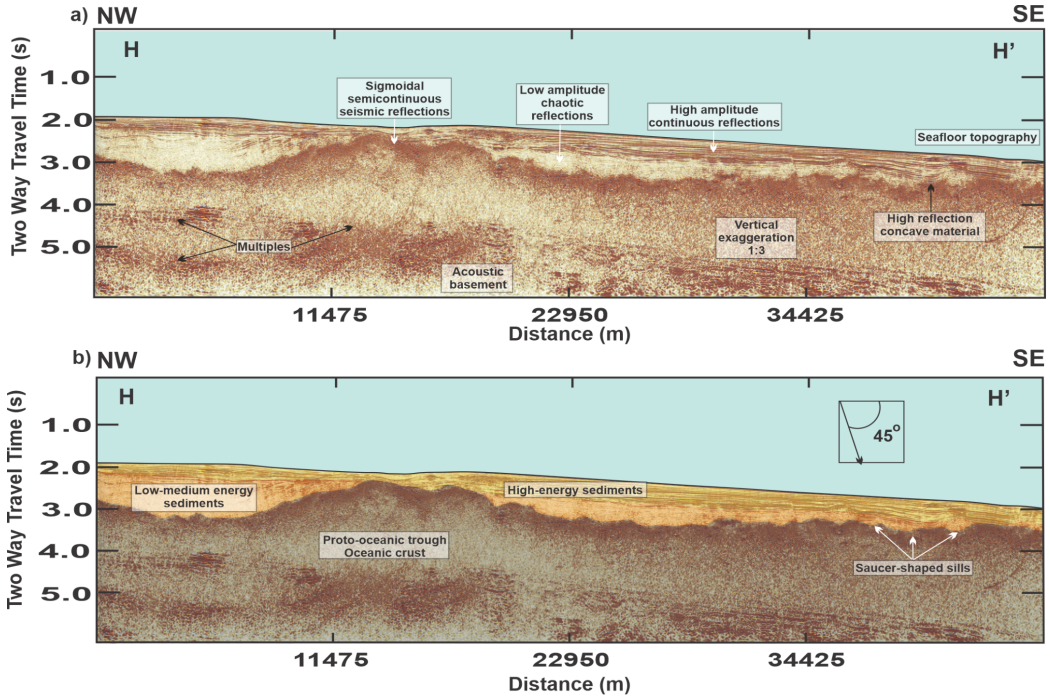

Figure 25. Seismic profile H-H' collected near profile G-G' subparallel of Farallon Transform fault on the northwestern Farallon basin. **a)** Raw seismic image and structural, stratigraphic seismic interpretation. **b)** Interpreted geologic cross section. Profile H-H' illuminates off-axis magmatic intrusions, including saucer-shaped sills.

Profile II' has a length of ~51 km. The seismic section runs parallel to the axis of the Farallon basin that was collected across the central part of western Farallon basin. The acoustic basement is formed by an oceanic basement containing some inactive normal faults. It is divided into two seismostratigraphic units separated by an angular unconformity. The lower unit contains sills emplacement, while the upper unit does not. Moreover, on profile II' just past the break in slope on the seafloor, the emplacement depth of magmatic sills rapidly shoals towards the seafloor and sill structure is much more complex, forming a dense and extensive shallow sills horizon (Figure 26). The high reflection concave material interpreted as sills is more extensive at the lower section of the low-medium energy sediments. Low-amplitudes chaotic reflections are most likely due to gas concentrations within the low-medium energy sediments.

Note the rapid change in sill depth and seismic response southeast of the profile and the observed flares (Figure 23). High-energy coherent reflections represent diatomaceous mud and sand turbidites deposited in a high-energy environment that cover the seafloor basin (Figure 26).

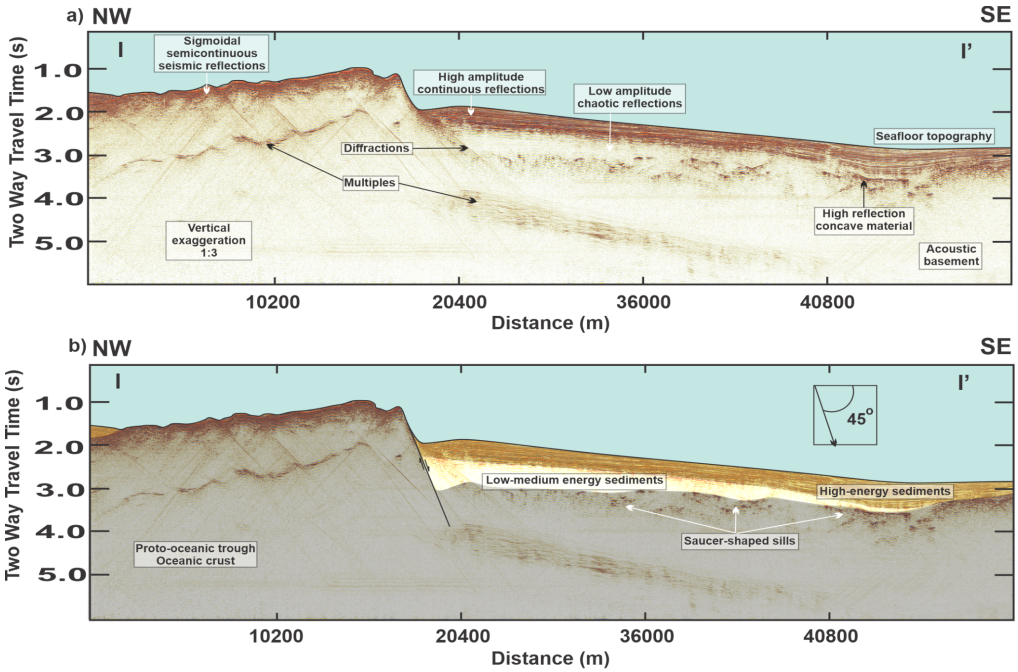

Figure 26. Seismic profile I-I' collected parallel of Farallon transform and subparallel of profiles G-G' and H-H'. **a)** Raw seismic image and structural, stratigraphic seismic interpretation. **b)** Interpreted geologic cross section. Profile I-I' illuminates off-axis magmatic intrusions, including saucer-shaped sills.

Profile JJ' spans ~132,384 m-long. The seismic profile is located at the northwestern side of Farallon basin. The image captures the continental shelf of the Baja California peninsula, the abandoned spreading center of the Farallon basin axis, and the region of the South-Farallon Massif (Figures 23 and 27). The northwestern part of the seismic section images a prominent low-angle normal fault system that extends in a southeast direction. Conversely, in the southeastern portion of the seismic image, we can observe an inactive spreading center located at the center of the seismic section, as well as the seamounts of the South-Farallon Massif at the southeastern part of the seismic profile parallel to the Atl transform. Below the sedimentary

cover, we observe distinct, prominent, and sigmoidal semi-continuous seismic reflections, approximately ~0.5 s of TWTT in thickness. These reflections serve as strong evidence for the existence of an oceanic basement in the central and southeastern regions of the seismic section at the abandoned spreading center (Figure 27).

As we move to the northwestern part of the seismic section, the basement elevated, reaching approximately 2.7 s of TWTT below sea level. This elevation change is associated with distinct seismic facies that suggest the possible transition to continental crust. Within this segment of the seismic profile, the acoustic basement displays disordered, low-amplitude reflections, which we interpret as indicative of crystalline plutonic material. The seismic facies sequence at the abandoned spreading center exhibits a significant change with high reflection concave reflectors interpreted as saucer-shaped sills situated at a depth of ~4.7 s of TWTT. Above this, there are two distinct seismic facies, featuring low-amplitude, non-chaotic reflections that extend over ~1.5 s of TWTT in thickness, and high-amplitude, continuous reflections with a thickness of around ~0.5 s of TWTT in the uppermost part of the sedimentary sequence interpreted as low-medium energy sediments and high-energy sediments respectively (Figure 27).

The low-angle normal faults on the northwestern side of the seismic profile are onlapped by sand turbidites deposited in a high-energy environment. Conversely, on the southeastern side of the seismic image, the South Farallon Massif shows a sigmoidal semicontinuous seismic reflection that extends to the ocean floor surface, revealing a basaltic basement. As a result, we have interpreted a transition zone between the low-angle normal faults and the abandoned spreading center, which exhibits key characteristics defining the shift from continental to oceanic crust along the boundary of the ruptured lithosphere. These characteristics include

alterations in the dip of the normal faults and a noticeable contrast in the seismic properties of the basement rocks, as well as the presence of deep irregular reflections and diffractions. Hence, the plutonic continental basement is located on the western margin of the basin and is recognized by a continuous high amplitude reflector (Figure 27).

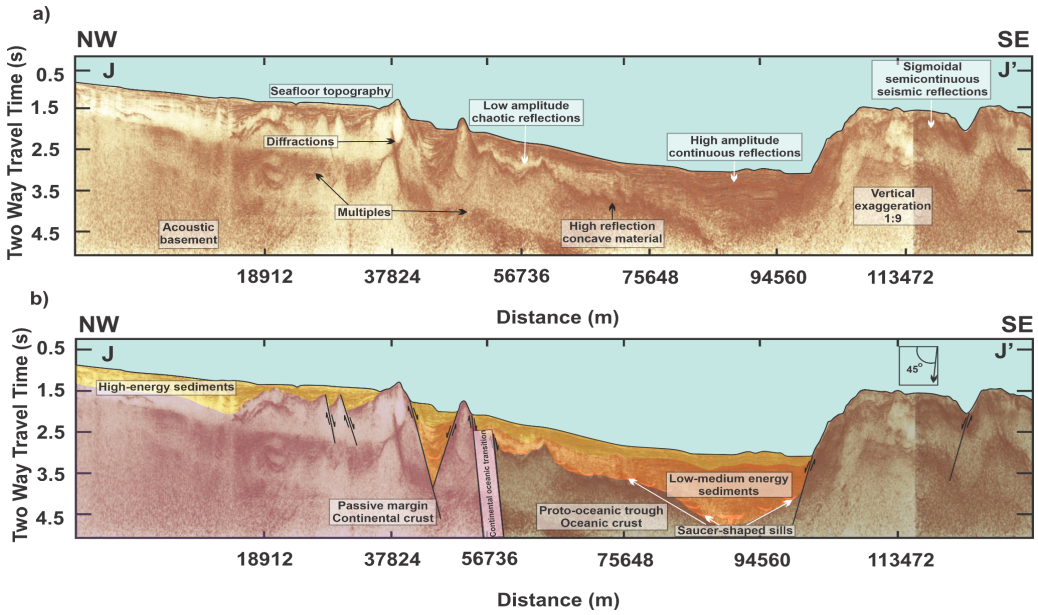

Figure 27. Seismic profile J-J' collected on the northwestern side of Farallon basin across the continental - oceanic transition of BC microplate until Farallon-south Massif at the southeastern side. **a)** Raw seismic image and structural, stratigraphic seismic interpretation. **b)** Interpreted geologic cross section. Profile J-J' illuminates off-axis magmatic intrusions, including saucer-shaped sills. Note, that the acoustic basement exhibits high amplitude continuous layers toward the southeast, while such reflections are absent toward the northwest. This observation may indicate the transition from oceanic to continental crust.

At the abandoned spreading center, the seismic facies sequence of this profile is consistent with the seismic profile JJ', where the acoustic basement is underlain by two distinct seismic facies characterized by low-amplitude non-coherence reflections, spanning a thickness of ~1.7 s of TWTT, and high-amplitude continuous reflections with a thickness of ~0.7 s of TWTT toward the uppermost part of the sedimentary sequence (Figure 28). Moreover, the two distinct seismic facies fill up the valleys between the low angle normal faults on the

northwestern side of the seismic profiles from bottom to the top as low-medium energy sediments and high-energy sediments. Nevertheless, the South-Farallon Massif basement outcrops at the surface of the ocean floor at ~2.4 s of TWTT, which is evident as sigmoidal semicontinuous seismic reflections. Hence, we have interpreted a transition zone between the low angle normal faults and the abandoned spreading center. This zone shows the main features that define the transition between continental and oceanic crust along the edge of the ruptured lithosphere. The valleys between the low-angle normal faults on the northwestern side of the seismic profile contain two distinct seismic facies. Low-energy chaotic reflections resemble inter-glacial diatomaceous muds. Sequences with alternating medium and high-energy coherent reflections indicate diatomaceous mud and sand turbidites deposited in a high-energy environment.

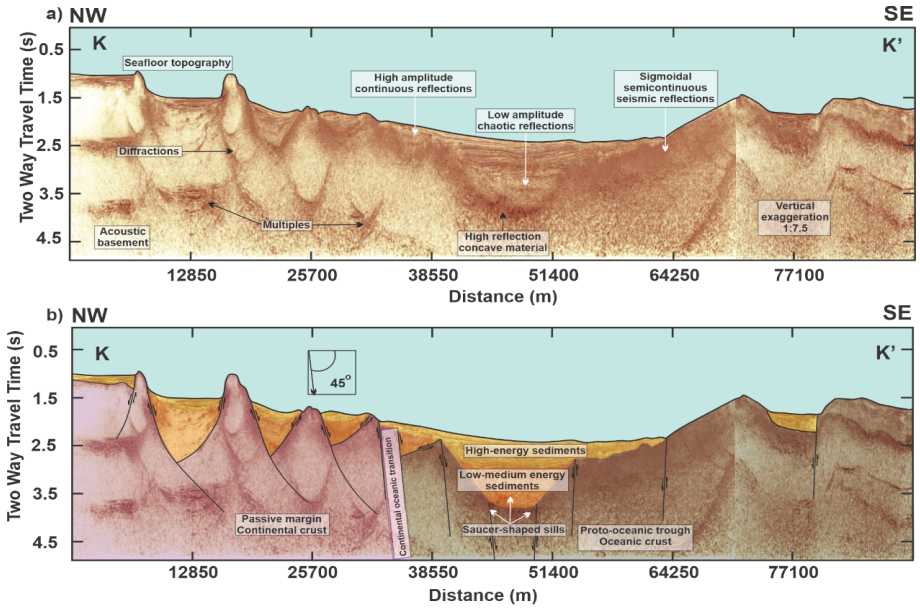

Figure 28. Seismic profile K-K' subparallel of profile J - J', collected on the northwestern side of Farallon basin across the continental - oceanic transition of BC microplate until Farallon-south Massif at the southeastern side. **a)** Raw seismic image and structural, stratigraphic seismic interpretation. **b)** Interpreted geologic cross section. Profile K-K' illuminates off-axis magmatic intrusions, including saucer-shaped sills. Note, that the acoustic basement exhibits high amplitude continuous layers toward the southeast, while such reflections are absent toward the northwest. This observation may indicate the transition from oceanic to continental crust.

The seismic profile LL' extends for ~67,5 km and provides detailed information on the structure of the eastern region of the northern Farallon basin (Figure 29). The seismic section intersects the Farallon transform fault towards the NE, interpreted as the basin's sidewall fault, which is the most important feature in the northeast flank forming a boundary of the basin (Figure 23). The acoustic basement displays prominent sigmoidal semicontinuous seismic reflections between 3.8 and 4.8 s of TWTT, underlain by two distinct seismic facies characterized by low-amplitude chaotic reflections, spanning a thickness of ~0.8 s of TWTT, and high-amplitude continuous reflections with a thickness of ~0.3 s of TWTT toward the uppermost part of the sedimentary sequence (Figure 29). Note that low-amplitude chaotic reflections strata display high-reflection concave material, suggesting the presence of saucer-shaped sill intrusions. They terminate abruptly and can be found in both concordance and discordance with the surrounding reflectors (e.g., Polteau et al., 2008). The magmatic intrusions in this area push up the overlying sediments, raising the acoustic basement and the two seismic facies up to ~2.8 s of TWTT depth at the middle of the seismic profile between 13,514 and 40,542 m length. (Figure 29). Note that in the northeast, approximately at a depth between 4.4 and 3.5 s of TWTT, the hanging wall block displays high reflection concave material suggesting the presence of saucer-shaped sills. Conversely, to the southwest, the basement undergoes a substantial rise to 2.0 s of TWTT, where distinct sigmoidal semi-continuous seismic reflections indicate oceanic crust (Figure 29). Also, note at the southwestern side of the profile MM' at ~70, km length and ~2.5s TWTT where we observe high reflection concave refector that we interpreted as a saucer-shaped sill.

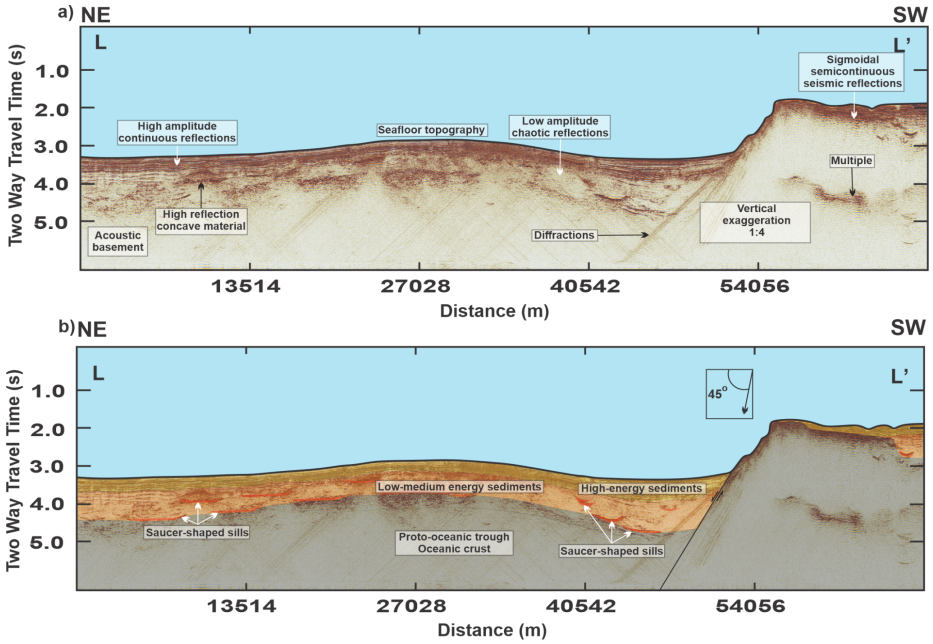

Figure 29. Seismic profile L-L' across northeastern Farallon Basin, crossing Farallon Transform. **a)** Raw seismic image and structural, stratigraphic seismic interpretation. **b)** Interpreted geologic cross section. Profile L-L' illuminates off-axis magmatic intrusions, including saucer-shaped sills.

Profile MM' spans a length of ~70,5 km, and images the western zone that crosses the BC continental shelf and the northwestern Farallon basin (Figure 30). It is anticipated that this profile would capture the seamount feature on the northwestern part. The seismic image exhibits a sloped architecture controlled by a low angle normal fault system striking southeast. In map view, the low angle normal fault bends to the northwest, forming a rotated block that controls the NW margin of the northern Farallon basin (Figure 23). Beneath the sedimentary cover, sigmoidal semi-continuous seismic reflections indicate the presence of oceanic basement along the entire image (Figure 30). On the northwestern side of the profile, a feature interpreted as a seamount rises approximately 1.0 s of TWTT from the seafloor, exhibiting sigmoidal semi-continuous seismic reflections indicative of an outcrop of oceanic crust. This seismic profile shows a symmetrical horst-graben structure delimited by two low-angle normal faults between

the seamount and the rotated block. Alongside with this structural relief, the low-angle normal faults created sufficient subsidence to accommodate the deposition of ~0.5 s of TWTT of one syn-tectonic sedimentary sequence. However, in the middle of the Farallon basin, above the acoustic basement, there is a syn-tectonic sedimentary package composed of two seismic facies, reaching a thickness of ~1.5 s of TWTT (Figure 30). The underlying sedimentary facies display layers with low-amplitude chaotic reflections, indicating sedimentation in low-medium energy environments. The overlying facies exhibit high-amplitude continuous reflections with good lateral coherence, suggesting sedimentation in high-energy environments. These two seismic facies are similar to the southern Farallon basin (see profile NN' in Figure 31). Moreover, notable features of high reflection concave material were observed between a depth of ~3.2 - 3.5s TWTT, indicating the location of magmatic intrusions in the form of sills, which result in the folding of the upper sedimentary sequences (Figure 30).

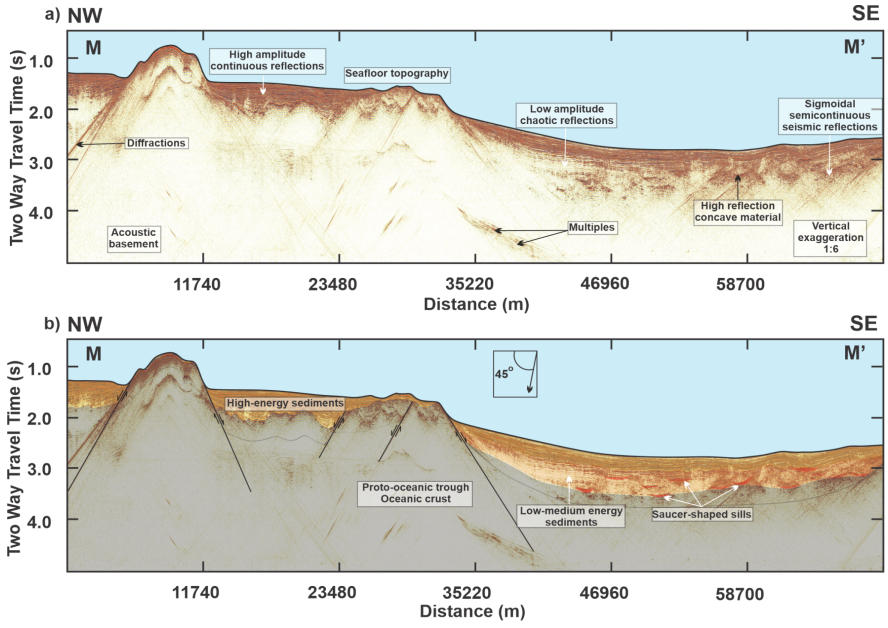

Figure 30. Seismic profile M-M' collected on the northwestern side of Farallon basin across the Sobrero basin (Figure 23). **a)** Raw seismic image and structural, stratigraphic seismic interpretation. **b)** Interpreted geologic cross section. Profile M-M' illuminates off-axis magmatic intrusions, including saucer-shaped sills.

Profile NN' cuts through the southern Farallon basin with a length of ~85 km (Figure 31). This section represents the deepest and narrowest feature within the Farallon basin. The axial graben is bounded by inward-stepping normal faults striking perpendicular to the principal displacement zone (Figure 23). The margins of the central graben are characterized by faults with a throw of approximately 25 km length and 10 km width, that represent the active spreading center of Farallon basin (Figure 31). Our analysis also indicates that these graben bounding faults likely served as fissures to facilitate the opening process, allowing for the accumulation of around 3 km length of recently formed oceanic basement between these two fissure walls at a depth of 2.5 to 4.5 s of TWTT below sea level. This inner graben is the dynamic spreading axis of the Farallon basin.

The most basal seismic facies are interpreted as highly fractured oceanic basement. This material can be observed in the seismic profile as sigmoidal semi-continuous seismic reflections at 2.5 s of TWTT depth on both flanks of the basin (Figure 31). On the northwestern flank of the axial graben, the sigmoidal semi-continuous reflections reach the seafloor topography at a depth of 2.5 s of TWTT, suggesting the young oceanic crust outcrops, whereas on the southeastern flank of the axial graben, the oceanic basement is covered by the two sedimentary units that we have interpreted throughout the Farallon basin from the bottom to the top as low-medium energy and high-energy sediments respectively. Observe, there is no sedimentary cover on top of the oceanic basement along the graben in the middle of the basin at a depth of 4.5 s of TWTT (Figure 31). The two sedimentary seismic facies, characterized by high and low-amplitude reflection, are only on the southeastern flank of the seismic profile and are clearly dissected by the graben (Figure 23). The sedimentary fill in the southeastern flank of the Farallon

basin is homogeneous like the northwestern flank (Figure 30), measuring ~1.3 s of TWTT thick. Therefore, thick sections of low-energy chaotic reflections resemble inter-glacial diatomaceous muds, while sequences with alternating medium and high-energy coherent reflections display diatomaceous mud and sand turbidites deposited in a high-energy environment.

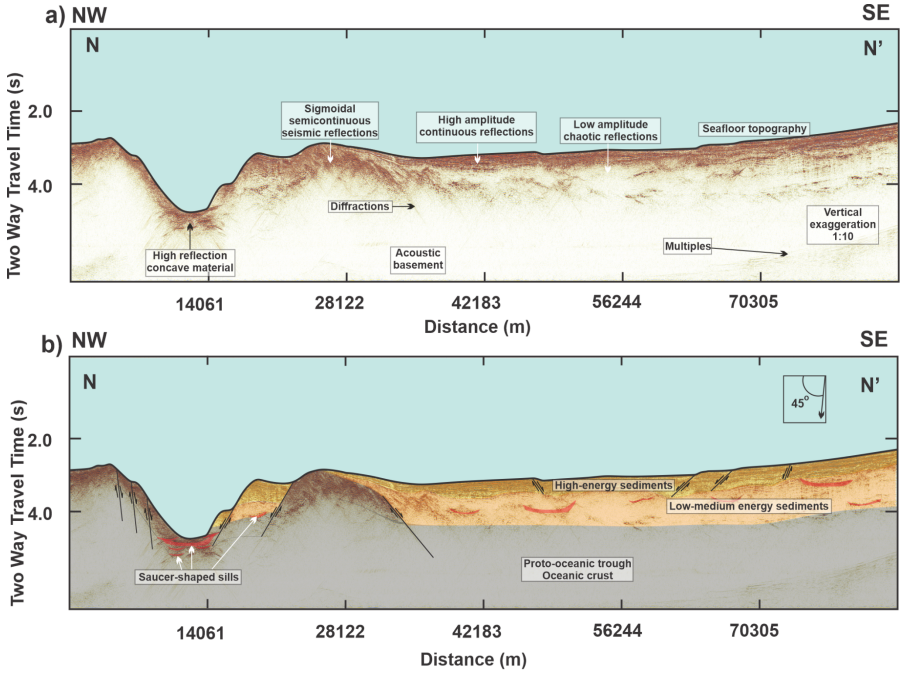

Figure 31. Seismic profile N-N' collected on the southeastern side of Farallon basin across the main axis of Farallon basin. **a)** Raw seismic image and structural, stratigraphic seismic interpretation. **b)** Interpreted geologic cross section. Profile N-N' illuminates Farallon basin axis magmatic intrusions, including saucer-shaped sills.

Profile OO' is a ~22 km long seismic profile that crosses the southeastern part of the southern Farallon basin (Figure 32). It is anticipated that this profile would capture the southeastern extension of the Atl transform fault. The seismic section intersects the Atl transform fault toward the NE, interpreted as the basin's sidewall (Figure 23). At the hanging wall, the acoustic basement displays a prominent sigmoidal semi-continuous seismic reflection at a depth of 2.5 s of TWTT, interpreted as oceanic crust. Profile O-O', only shows one distinct seismic facies characterized by high amplitude continuous reflection, spanning a thickness of

~0-5 TWTT, representing high-energy sediments at the uppermost part of the sedimentary sequence (Figure 32). However, toward the NE, the basement rises dramatically to 0.5s TWTT, where different seismic facies suggest a potential representation of continental crust. Within this segment of the seismic profile, the acoustic basement reveals disordered, weak amplitude reflections, which we interpret as crystalline plutonic material (Infante-Paez and Marfurt, 2017).

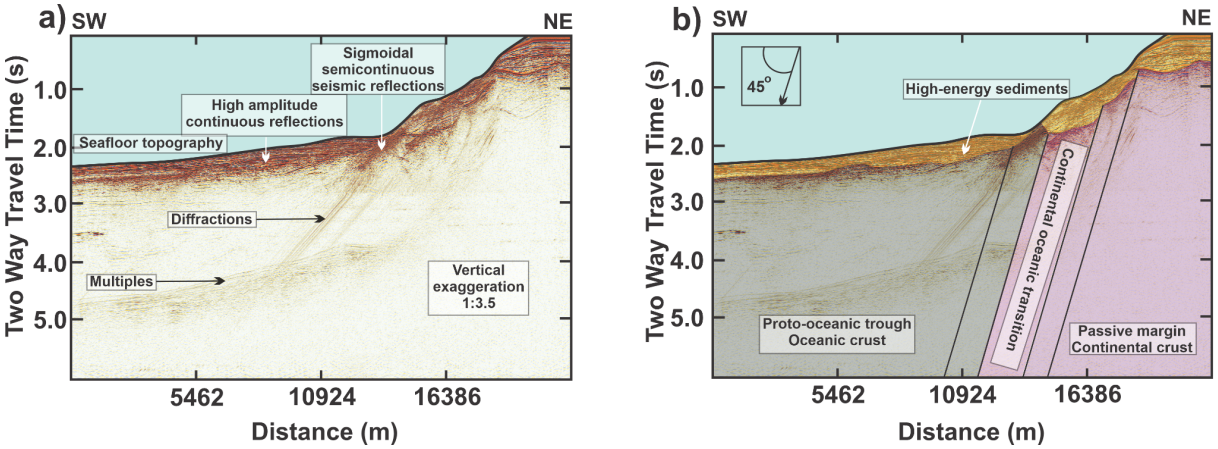

Figure 32. Seismic profile O-O' across Farallon Transform on the southeastern Farallon Basin. **a)** Raw seismic image and structural, stratigraphic seismic interpretation. **b)** Interpreted geologic cross section. Profile O-O' shows the continental - oceanic transition on the Mexico midland continental shelf. Note, that the acoustic basement exhibits high amplitude continuous layers toward the southwest, while such reflections are absent toward the northeast. This observation may indicate the transition from oceanic to continental crust.

III.4.3. Rifted Margins and Continent-Ocean transitions

The boundary between continental and oceanic lithosphere within the Farallon basin is delineated by alterations in seafloor topography, changes in the seismic properties of the upper acoustic basement, and the prevalence of numerous irregular reflections and diffractions observed at greater depths in the seismic profiles. The Farallon basin itself is defined by an inward-facing bathymetric escarpment with several hundred meters of an extended oceanic pull-apart basin with a single depocenter. At the upper and outer edge of the escarpment, the seafloor exhibits a more complex and uneven bathymetry, with numerous faults cutting through it. In

contrast, on the lower and inner side of the escarpment, the seafloor maintains a relatively smooth, low-relief surface located at approximately 3.0 s TWTT meters below sea level with an ocean hill on the northwest side (Figure 23). Each of the seismic profiles that cross the bathymetric escarpment reveals that this geological feature coincides with a pronounced change in the seismic attributes of the upper surface of acoustic basement. On the inner side, beneath the escarpment, the upper surface of the acoustic basement is delineated by a sequence of robust, sub-planar, and consistently continuous reflections exhibiting high amplitude and low frequency. These features are indicative of a significant rise in acoustic impedance. We interpret this rock unit to represent the top of high-density basaltic lava flows of the oceanic crust. Conversely, on the exterior side of the elevated escarpment, the basement is covered by a region of high-energy sediments without the present of highly reflective concave interfaces (Figure 23).

Widespread geophysical evidence of young sill intrusion is evident on multiple high-resolution seismic profiles collected across oceanic basin floors (Figures 24-32) and near transform boundaries (Figure 23), suggesting that melt in the central GC is able to intrude upwards through both highly faulted and thinned oceanic crust and off-axis oceanic crust, injecting into overlying young, unconsolidated sediments. As described earlier, attenuation of seismic energy at the sediment-sill interface results in an acoustic shadow zone below. Identification of the boundary zone between continental and oceanic crust in the Farallon basin using seismic reflection profiling is evidence of the continental-oceanic crustal transition at the limits of Farallon basin where sills are not observed.

Multiple crossings of the continental-oceanic boundary were made at the western flank of Farallon basin with the high-resolution seismic data (Figure 24-32). Multibeam bathymetry

shows major continental crust fault scarps bounding the western part of the basin, with the seafloor gently sloping towards the axial trough down to about 2,000 m depth.

III.4.4. Comparative analysis of basin geomorphology in the southern Gulf of California

The following is a comparison between the geometry of Farallon basin versus Carmen basin, Guaymas basin and Pescadero Basin Complex and the surrounding structures to infer the evolutionary state according to Aydin and Nur (1982); Gürbüz (2010); van Wijk et al. (2017) and references therein. Oceanic transforms separating oceanic crust and offsetting mid-oceanic spreading ridges are one of the five distinctive active strike-slip settings known. Thus, en échelon arrays of pull-apart basins are also observed on active 'leaky' or transtensional oceanic transforms, but restraining bends are rarely observed (Mann, 2007). Oceanic transforms separating mid-oceanic ridges found in ocean-ocean transition crust as a transtensional pull-apart basin with 2 depocenters is observed at the Carmen Basin, northwest of the Farallon basin (Julià-Miralles et al., 2024). However, the Farallon basin is a continent-ocean pull-apart basin bounded by the Farallon transform fault and the Atl transform fault with a single depocenter. The overall geometry and geomorphological features of the Farallon basin suggest that the basin has evolved due to pure strike-slip deformation (e.g., Wu et al., 2009), different to the Carmen basin located further northwest (e.g., Julià-Miralles et al., 2024), and Pescadero basin complex located further southeast (e.g., Ramírez-Zerpa et al., 2022).

Regarding the morphology of the Farallon basin, it has a lazy Z geometry which results in a length-to-width ratio of ~4:1 (~220 km-length, ~50 km-width). Similar to the Guaymas basin and Carmen basin, Farallon basin started to open as two ocean offset ridges, with the southern ridge being abandoned later (Lonsdale, 1989; Duque-Trujillo et al., 2015). The opening started as a pull-apart basin ~6 Ma, but as the velocity of tectonic plate separation increased at

3.5 Ma to 5.4 cm/year, the pull-apart basins evolved to develop spreading centers. This evolution is expressed in the Farallon basin structure where the southern ridge was abandoned, whereas active seafloor formation is located in the northern ridge (Piñero et al., 2008). In the Farallon basin the existence of two types of crust has been defined, the continental crust and oceanic crust known as the "new creation" (Piñero et al., 2008). The continental crust is divided into the plutonic crust, which limits the Farallon basin in its west flank, whereas the volcanic crust is represented most in the Massif Southern-Farallon. The "new creation" oceanic crust is located in the center of Farallon basin and is characterized by the intrusion of mantle-derived melts emplaces as sills. The spreading center area shows the depth of the basement rises to more than 4,000 m. Another small depocenter is found in the area between the Farallon Basin and the Farallon west hills, where the sediment thickness reaches 1,400 m depth and the basement depth is more than 4400 m (Hernández-Maya et al., 2010).

The Guaymas basin exhibits a rhomboidal shape with a length-to-width ratio of ~4:1 (Figure 4; ~250,000 m-long against ~65,500 m-width). The Guaymas basin also shows that a fault zone separates continental and oceanic crusts at the sheared northern margin of Guaymas Basin (Lonsdale 1989). The general features of the axial graben are characterized by 3–5 km-wide, 1500 m deep in the Guaymas basin to 1200 m, whereas in the Farallon basin below, the adjacent basin acts as depocenters for sedimentary turbidity flow (Kluesner et al., 2014). Since approximately 2 Ma, the seafloor spreading across the Northern axial graben of Guaymas basin has been nearly symmetric at a rate of 46 km/Ma (Lonsdale and Kluesner, 2010). The recognition of active sill intrusion into Guaymas sediments allowed Lizarralde et al. (2010) to do the following. Firstly, to predict the existence of widely distributed, methane-hosted seafloor biological communities and secondly, to interpret the oceanic crust is a combination of sills and

sediment that lacks the high permeability of faulted extrusive basalts that makes up normal oceanic crust.

The Pescadero Basin Complex (PBC) has an~4:1 a length-to-width ratio of the basin which is controlled by the amount of fault overlap and separation between the master transforms (Ramírez-Zerpa et al., 2021). Ramírez-Zerpa et al. (2021) separated PBC into three sub basins called *Southern Pescadero basin (SPB), Central Pescadero basin (CPB), Northern Pescadero basin (NPB)*. These three distinctive rhombohedral-shaped pull-apart basins are separated by several tens of kilometers along highly overlapped transform fault segments. Thus, the three associated basins were classified as highly evolved pull-apart basins according to their rhomboidal shape and fault overlap between their bordering transform faults (Ramírez-Zerpa et al., 2021). Moreover, these basins are bounded by an array of oblique-extensional faults (i.e., the basin sidewall faults, BSFs) connected with the master transforms (Ramírez-Zerpa et al., 2021).

III. 5. Conclusions

Hydrothermal and Geothermal Potential: High-resolution seismic data reveal widespread magmatic intrusions and hydrothermal circulation within the Farallon Basin. The presence of saucer-shaped sills observed at the seismics profiles and flares identified during the FK210922 expedition in October 2021 aboard the R/V *Falkor*, suggests significant geothermal energy potential, making the basin an important site for future energy exploration. Based on our analysis, we observe that sills are present in the oceanic crust and perhaps absent in the continental crust within the Farallon Basin. This distinct occurrence suggests that the formation of sills is specific to oceanic crust, likely due to the unique tectonic and magmatic processes

associated with oceanic spreading centers. The presence of an abandoned spreading center near the Southern-Farallon Massif suggests that the Farallon Basin is a transtensional pull-apart basin. This is indicated by the coexistence of both an active and an abandoned spreading center, similar to neighboring basins Carmen and Pescadero in the southern Gulf of California. The different seismic characteristics observed between the continental and oceanic crust in the Farallon Basin delineate the boundaries of the transition between continental and oceanic crust. The low-angle faults observed in the continental crust indicate a passive margin, generating rotated blocks. This seismic variation provides clear evidence of the distinct geological processes and structural changes occurring at the crustal transition zone.

References

Allen, P. A., & Allen, J. R. (2013). Basin analysis: Principles and application to petroleum play assessment. John Wiley & Sons.

Aragón-Arreola, M., Morandi, M., Martín-Barajas, A., Delgado-Argote, L., & González-Fernández, A. (2005). Structure of the rift basins in the central Gulf of California: Kinematic implications for oblique rifting. *Tectonophysics*, *409*(1-4), 19-38. https://doi.org/10.1016/j.tecto.2005.08.002.

Aragón-Arreola, M., & Martín-Barajas, A. (2007). Westward migration of extension in the northern Gulf of California, Mexico. *Geology*, *35*(6), 571-574. https://doi.org/10.1130/G23360A.1.

Atwater, T. (1970). Implications of plate tectonics for the Cenozoic tectonic evolution of western North America. *Geological Society of America Bulletin*, *81*(12), 3513-3536. https://doi.org/10.1130/0016-7606(1970)81[3513:IOPTFT]2.0.CO;2.

Atwater, T. (1989). Plate tectonic history of the northeast Pacific and western North America. The Eastern Pacific Ocean and Hawaii Geology of North America. *Geological Society of America*, Boulder, Colorado, pp. 21–72 (v. N). https://doi.org/10.1130/DNAG-GNA-N.21.

Atwater, T., & Stock, J. (1998). Pacific-North America plate tectonics of the Neogene southwestern United States: an update. *International Geology Review*, *40*(5), 375-402. https://doi.org/10.1080/00206819809465216.

Balestrieri, M. L., Ferrari, L., Bonini, M., Duque-Trujillo, J., Cerca, M., Moratti, G., & Corti, G. (2017). Onshore and offshore apatite fission-track dating from the southern Gulf of California: Insights into the time-space evolution of the rifting: *Tectonophysics, 719*, 148-161. https://doi.org/10.1016/j.tecto.2017.05.012.

Bennett, S. E., Oskin, M. E., Iriondo, A., & Kunk, M. J. (2016). Slip history of the La Cruz fault: Development of a late Miocene transform in response to increased rift obliquity in the northern Gulf of California. *Tectonophysics, 693*, 409-435. https://doi.org/10.1016/j.tecto.2016.06.013.

Bohannon, R. G., & Parsons, T. (1995). Tectonic implications of post–30 Ma Pacific and North American relative plate motions. *Geological Society of America Bulletin*, *107*(8),937-959. https://doi.org/10.1130/0016-7606(1995)107%3C0937:TIOPMP%3E2.3.CO;2.

Bot, A., Geoffroy, L., Authemayou, C., Bellon, H., Graindorge, D., & Pik, R. (2016). Miocene detachment faulting predating EPR propagation: Southern Baja California. *Tectonics*, *35*(5), 1153-1176 https://doi.org/10.1002/2015TC004030.

Buck, W. R. (1993). Effect of lithospheric thickness on the formation of high-and low-angle normal faults. *Geology*, *21*(10), 933-936. https://doi.org/10.1130/0091-7613(1993)021%3C0933:EOLTOT%3E2.3.CO;2.

Buck, W. R. (1988). Flexural rotation of normal faults. *Tectonics*, *7*(5), 959-973. https://doi.org/10.1029/TC007i005p00959.

Bunge, H. P., & Grand, S. P. (2000). Mesozoic plate-motion history below the northeast Pacific Ocean from seismic images of the subducted Farallon slab. *Nature*, *405*(6784), 337-340. https://doi.org/10.1038/35012586.

Chopra, S., & Marfurt, K. J. (2007), Seismic attributes for prospect identification and reservoir characterization. Tulsa, Oklahoma, U.S.A., *Society of Exploration Geophysicists and European Association of Geoscientists and Engineers*, 457 pp. https://doi.org/10.1190/1.9781560801900.

Christie-Blick, N., & Biddle, K. T. (1985). Deformation and basin formation along strike-slip faults. *Society of Economic Paleontologists and Mineralogists Special Publication, 37*, 1–34. https://doi.org/10.2110/pec.85.37.0001.

Contreras-Pérez, J., Ramírez-Zerpa, N., & Negrete-Aranda, R. (2012). Modelos tectonoestratigráficos de las cuencas de Tiburón y Wagner en el norte del Golfo de California. *Revista Mexicana de Ciencias Geológicas*, *29*(1), 140-157. http://www.scielo.org.mx/scielo.php?script=sci_arttext&tnqh_x0026;pid=S1026-87742012000100010.

DeMets, C., & Dixon, T. H. (1999). New kinematic models for Pacific-North America motion from 3 Ma to present, I: Evidence for steady motion and biases in the NUVEL-1A model. *Geophysical Research Letters*, *26*(13), 1921-1924. https://doi.org/10.1029/1999GL900405.

DeMets, C., Gordon, R. G., & Argus, D. F. (2010). Geologically current plate motions. Geophysical journal international, 181(1), 1-80. https://doi.org/10.1111/j.1365-246X.2009.04491.x.

Di Luccio, F., Persaud, P., & Clayton, R. W. (2014). Seismic structure beneath the Gulf of California: a contribution from group velocity measurements. *Geophysical Journal International, 199*(3), 1861-1877. https://doi.org/10.1093/gji/ggu338.

Dorsey, R. J., Umhoefer, P. J., & Renne, P. R. (1995). Rapid subsidence and stacked Gilbert-type fan deltas, Pliocene Loreto basin, Baja California Sur, Mexico. *Sedimentary Geology, 98* (1-4), 181-204. https://doi.org/10.1016/0037-0738(95)00032-4.

Duque-Trujillo, J., Ferrari, L., Norini, G., & López-Martínez, M. (2014). Miocene faulting in the southwestern Sierra Madre Occidental, Nayarit, Mexico: kinematics and segmentation during the initial rifting of the southern Gulf of California. *Revista Mexicana de Ciencias Geológicas, 31*(3), 283-302. URL: http://www.redalyc.org/articulo.oa?id=57232747001.

Duque-Trujillo, J., Ferrari, L., Orozco-Esquivel, T., López-Martínez, M., Lonsdale, P., Bryan, S. E., Kluesner, J., Piñero-Lajas, D., & Solari, L., (2015). Timing of rifting in the southern Gulf of California and its conjugate margins: insights from the plutonic record. *Geological Society of America Bulletin, 127*(5-6), 702-736. https://doi.org/10.1130/B31008.1.

Farangitakis, G. P., McCaffrey, K. J., Willingshofer, E., Allen, M. B., Kalnins, L. M., van Hunen, J., Persaud, P. & Sokoutis, D. (2021). The structural evolution of pull-apart basins in response to changes in plate motion. *Basin Research*, *33*(2), 1603-1625. https://doi.org/10.1111/bre.12528.

Ferrari, L., Orozco-Esquivel, T., Bryan, S. E., Lopez-Martinez, M., & Silva-Fragoso, A. (2018). Cenozoic magmatism and extension in western Mexico: Linking the Sierra Madre Occidental silicic large igneous province and the Comondú Group with the Gulf of California rift. *Earth-Science Reviews*, *183*, 115-152. https://doi.org/10.1016/j.earscirev.2017.04.006.

Fletcher, J. M., & Munguia, L. (2000). Active continental rifting in southern Baja California, Mexico: Implications for plate motion partitioning and the transition to seafloor spreading in the Gulf of California. *Tectonics*, *19*(6), 1107-1123. https://doi.org/10.1029/1999TC001131.

Fletcher, J. M., Kohn, B. P., Foster, D. A., & Gleadow, A. J. (2000). Heterogeneous Neogene cooling and exhumation of the Los Cabos block, southern Baja California: Evidence from fission-track thermochronology. *Geology*, *28*(2), 107-110. https://doi.org/10.1130/0091-7613(2000)28%3C107:HNCAEO%3E2.0.CO;2.

Fletcher, J. M., Pérez-Venzor, J. A., González-Barba, G., & Aranda-Gomez, J. J. (2003). Ridge-trench interactions and the ongoing capture of the Baja California microplate—New from the southern Gulf extensional province. *In Geologic transects across the Cordilleran Mexico, Guidebook for field trips of the 99th Annual meeting of the Cordilleran Section of the Geological Society of America*, Volume Publicacion Especial 1: Mexico, D.F., Universidad Nacional Autónoma de México, Instituto de Geología, p. 13–31.

Fletcher, J. M., Grove, M., Kimbrough, D., Lovera, O., & Gehrels, G. E. (2007). Ridge-trench interactions and the Neogene tectonic evolution of the Magdalena shelf and southern Gulf of California: Insights from detrital zircon U-Pb ages from the Magdalena fan and

adjacent areas. *Geological Society of America Bulletin*, *119*(11-12), 1313-1336. https://doi.org/10.1130/B26067.1.

Fletcher, J. M., & Spelz, R. M. (2009). Patterns of Quaternary deformation and rupture propagation associated with an active low-angle normal fault, Laguna Salada, Mexico: Evidence of a rolling hinge? *Geosphere*, *5*(4), 385-407. https://doi.org/10.1130/GES00206.1.

Fornari, D. J., Gallo, D. G., Edwards, M. H., Madsen, J. A., Perfit, M. R., & Shor, A. N. (1989). Structure and topography of the Siqueiros transform fault system: Evidence for the development of intra-transform spreading centers. Marine Geophysical Researches, 11, 263-299. https://doi.org/10.1007/BF00282579

Fossen, H., 2010, Structural Geology, in Cambridge Univ. Press: Cambridge, U. K, 463 pp.

González-Escobar, M., Suárez-Vidal, F., Hernández-Pérez, J. A., & Martín-Barajas, A. (2010). Seismic reflection-based evidence of a transfer zone between the Wagner and Consag basins: implications for defining the structural geometry of the northern Gulf of California. *Geo-Marine Letters, 30*(6), 575-584. https://doi.org/10.1007/s00367-010-0204-0.

González-Fernández, A., Dañobeitia, J. J., Delgado-Argote, L. A., Michaud, F., Córdoba, D., & Bartolomé, R. (2005). Mode of extension and rifting history of upper Tiburón and upper Delfín basins, northern Gulf of California. *Journal of Geophysical Research: Solid Earth*, *110*(B1). https://doi.org/10.1029/2003JB002941.

Gregg, P. M., Lin, J., & Smith, D. K. (2006). Segmentation of transform systems on the East Pacific Rise: Implications for earthquake processes at fast-slipping oceanic transform faults. *Geology*, *34*(4), 289-292. https://doi.org/10.1130/G22212.1.

Gregg, P. M., Lin, J., Behn, M. D., & Montési, L. G. (2007). Spreading rate dependence of gravity anomalies along oceanic transform faults. *Nature*, *448*(7150), 183-187. https://doi.org/10.1038/nature05962.

Gürbüz, A. (2010). Geometric characteristics of pull-apart basins. *Lithosphere*, *2*(3), pp.199-206. https://doi.org/10.1130/L36.1.

Howell, S. M., Olive, J. A., Ito, G., Behn, M. D., Escartin, J., & Kaus, B. (2019). Seafloor expression of oceanic detachment faulting reflects gradients in mid-ocean ridge magma supply. *Earth and Planetary Science Letters*, *516*, 176-189. https://doi.org/10.1016/j.epsl.2019.04.001.

Infante-Paez, L., & Marfurt, K. J. (2017). Seismic expression and geomorphology of igneous bodies: A Taranaki Basin, New Zealand, case study. *Interpretation, 5*(3), SK121-SK140. https://doi.org/10.1190/INT-2016-0244.1

Kluesner, J. W. (2011). *Marine geophysical study of cyclic sedimentation and shallow sill intrusion in the floor of the Central Gulf of California*. University of California, San Diego (Ph.D. Thesis, 231 pp). URL: https://www.proquest.com/openview/10ac7f482ea0c51dbd43afd312e6e8fc/1?pq-origsite=gscholar&cbl=18750.

Kluesner, J., Lonsdale, P., & González-Fernández, A. (2014). Late Pleistocene cyclicity of sedimentation and spreading-center structure in the Central Gulf of California. *Marine Geology*, *347*, 58-68. https://doi.org/10.1016/j.margeo.2013.11.001.

Kusznir, N. J., & Karner, G. D. (2007). Continental lithospheric thinning and breakup in response to upwelling divergent mantle flow: application to the Woodlark, Newfoundland and Iberia margins. *Geological Society, London, Special Publications*, *282*(1), 389-419. https://doi.org/10.1144/SP282.16.

Mann, P. (2007). Global catalogue, classification and tectonic origins of restraining-and releasing bends on active and ancient strike-slip fault systems. Geological Society, London, Special Publications, 290(1), 13-142. https://doi.org/10.1144/sp290.2

Lavier, L. L., Roger Buck, W., & Poliakov, A. N. (1999). Self-consistent rolling-hinge model for the evolution of large-offset low-angle normal faults. *Geology*, *27*(12), 1127-1130. https://doi.org/10.1130/0091-7613(1999)027%3C1127:SCRHMF%3E2.3.CO;2.

Liner, C. L. (2016). Elements of 3D seismology. Society of exploration geophysicists. https://doi.org/10.1190/1.9781560803386.ref.

Lizarralde, D., Axen, G. J., Brown, H. E., Fletcher, J. M., González-Fernández, A., Harding, A. J., Holbrook, W.S., Kent, G.M., Paramo, P., Sutherland, F., & Umhoefer, P. J. (2007). Variation in styles of rifting in the Gulf of California. *Nature*, *448*(7152), 466-469. https://doi.org/10.1038/nature06035.

Lizarralde, D., Soule, S. A., Seewald, J. S., & Proskurowski, G. (2011). Carbon release by off-axis magmatism in a young sedimented spreading centre. *Nature Geoscience*, *4*(1), 50-54. https://doi.org/10.1038/ngeo1006.

Lonsdale, P. (1989). Geology and tectonic history of the Gulf of California. In: Hussong, D., Winterer, E.L., Decker, R.W. (Eds.), *The Eastern Pacific Ocean and Hawaii, The Geology of North America, N. Geological Society of America*, Boulder, Colorado, pp. 499–521. https://doi.org/10.1130/dnag-gna-n.499.

Macias-Iñiguez, I., Yarbuh, I., Spelz-Madero, R., González-Fernández, A., Fletcher, J. M., Contreras, J., Ramírez-Zerpa, N., Santa Rosa-del Río, M. A., & Guardado-France, R. (2019). Modo de extensión de la corteza y formación del Sistema Extensional de Cerralvo, sur del Golfo de California, a partir de datos de reflexión sísmica en 2D.

Revista Mexicana de Ciencias Geológicas, 36(3), 334-347. https://doi.org/10.22201/cgeo.20072902e.2019.3.1352.

Mann, P., Hempton, M. R., Bradley, D. C., & Burke, K. (1983). Development of pull-apart basins. *Journal of Geology, 91*(5), 529–554. https://doi.org/10.1086/628803.

Martín-Barajas, A., González-Escobar, M., Fletcher, J. M., Pacheco, M., Oskin, M., & Dorsey, R. (2013). Thick deltaic sedimentation and detachment faulting delay the onset of continental rupture in the Northern Gulf of California: Analysis of seismic reflection profiles. *Tectonics*, *32*(5), 1294-1311. https://doi.org/10.1002/tect.20063.

McKenzie, D. (1978). Active tectonics of the Alpine—Himalayan belt: the Aegean Sea and surrounding regions. *Geophysical Journal International*, *55*(1), 217-254. https://doi.org/10.1111/j.1365-246X.1978.tb04759.x.

McQuillin, R., Bacon, M., & Barclay, W. (1985). An introduction to seismic interpretation. Journal of Sedimentary Research, 55(6), 940-941. https://doi.org/10.2110/jsr.940.

Negrete-Aranda, R., Contreras, J., & Spelz, R. M. (2013). Viscous dissipation, slab melting, and post-subduction volcanism in south-central Baja California, Mexico. *Geosphere*, *9*(6), 1714-1728. https://doi.org/10.1130/GES00901.1.

Negrete-Aranda, R., Neumann, F., Harris, R. N., Contreras, J., Zierenberg, R. A., & Caress, D. W. (2019). First Heat Flow Measurements in the Auka and JaichMaa'ja'ag vent fields Pescadero Basin, Southern Gulf of California. In *AGU Fall Meeting Abstracts* (Vol. 2019, pp. V13D-0187). URL: https://ui.adsabs.harvard.edu/abs/2019AGUFM.V13D0187N/abstract

Negrete-Aranda, R., Neumann, F., Contreras, J., Harris, R. N., Spelz, R. M., Zierenberg, R., & Caress, D. W. (2021). Transport of Heat by Hydrothermal Circulation in a Young Rift Setting: Observations from the Auka and JaichMaa ja' ag' vent Fields in the Pescadero Basin, Southern Gulf of California. *Journal of Geophysical Research: Solid Earth, 126*(8), e2021JB022300. https://doi.org/10.1029/2021JB022300.

Nicholson, C., Sorlien, C. C., Atwater, T., Crowell, J. C., & Luyendyk, B. P. (1994). Microplate capture, rotation of the western Transverse Ranges, and initiation of the San Andreas transform as a low-angle fault system. *Geology*, *22*(6), 491-495. https://doi.org/10.1130/0091-7613(1994)022%3C0491:MCROTW%3E2.3.CO;2.

Piñero-Lajas, D. (2008). *Seismic reflection and 40Ar-39Ar dating of continental basement in the western margin of Farallon basin (southern Gulf of California, Mexico)*. CICESE, Ensenada, Baja California, México (M.Sc. thesis in Earth Science. 155 pp). URL: https://biblioteca.cicese.mx/catalogo/tesis/ficha.php?id=17932.

Polteau, S., Ferré, E. C., Planke, S., Neumann, E. R., & Chevallier, L. (2008). How are saucer-shaped sills emplaced? Constraints from the Golden Valley Sill, South Africa. *Journal of Geophysical Research: Solid Earth*, *113*(B12). https://doi.org/10.1029/2008JB005620.

Pockalny, R. A., Fox, P. J., Fornari, D. J., Macdonald, K. C., & Perfit, M. R. (1997). Tectonic reconstruction of the Clipperton and Siqueiros Fracture Zones: Evidence and consequences of plate motion change for the last 3 Myr. Journal of Geophysical Research: Solid Earth, 102(B2), 3167-3181. https://doi.org/10.1029/96JB03391.

Ramírez-Zerpa, N., Spelz, R. M., Yarbuh, I., Negrete-Aranda, R., Contreras, J., Clague, D. A., Neumann, F., Caress, D. W., Zierenberg, R. A., & González-Fernández, A. (2022). Architecture and tectonostratigraphic evolution of the Pescadero Basin Complex, southern Gulf of California: Analysis of high-resolution bathymetry data and seismic reflection profiles. *Journal of South American Earth Sciences*, 103678. https://doi.org/10.1016/j.jsames.2021.103678.

Rodriguez, M., Chamot-Rooke, N., Fournier, M., Huchon, P., & Delescluse, M. (2013). Mode of opening of an oceanic pull-apart: The 20° N Basin along the Owen Fracture Zone (NW Indian Ocean). *Tectonics*, *32*(5), 1343-1357. https://doi.org/10.1002/tect.20083.

Sarkar, S., Moser, M., Berndt, C., Doll, M., Böttner, C., Chi, W. C., Klaeschen, D., Galerne, C., Karstens, J., Geilert, S., Mortera-Gutierrez, C., & Hensen, C. (2022). Thermal state of the Guaymas Basin derived from gas hydrate bottom simulating reflections and heat flow measurements. *Journal of Geophysical Research: Solid Earth*, *127*(8). https://doi.org/10.1029/2021JB023909.

Sheriff, R. E., & Geldart, L. P., 1995. Exploration Seismology Volume I: History, Theory and Data Acquisition: Cambridge University Press, Cambridge, 559 pp. https://doi.org/10.1017/CBO9781139168359.

Sheriff, R. E. (1997). Seismic resolution a key element. AAPG Explorer, 18(10), 44-51. URL: https://www.searchanddiscovery.com/pdfz/documents/sheriff02/images/sheriff02.pdf.html.

Sims, D., Ferrill, D. A., & Stamatakos, J. A. (1999). Role of a ductile decollement in the development of pull-apart basins: Experimental results and natural examples. *Journal of Structural Geology*, *21*(5), 533-554. https://doi.org/10.1016/S0191-8141(99)00010-3.

Spencer, J. E., & Normark, W. R. (1979). Tosco-Abreojos fault zone: A Neogene transform plate boundary within the Pacific margin of southern Baja California, Mexico. *Geology*,

7(11), 554-557. https://doi.org/10.1130/0091-7613(1979)7%3C554:TFZANT%3E2.0.CO;2.

Stock, J. M., & Hodges, K. V. (1989). Pre-Pliocene extension around the Gulf of California and the transfer of Baja California to the Pacific plate. *Tectonics*, *8*(1), 99-115. https://doi.org/10.1029/TC008i001p00099.

Sutherland, F. H., Kent, G. M., Harding, A. J., Umhoefer, P .J., Driscoll, N. W., Lizarralde, D., & Fletcher, J. M., Axen, J. G., Holbrook, W. S., González-Fernández, A., Lonsdale, P. (2012). Middle Miocene to early Pliocene oblique extension in the southern Gulf of California. *Geosphere, 8*(4), 752–770. https://doi.org/10.1130/GES00770.1.

Teske, A. P., Lizarralde, D., Höfig, T. W., Aiello, I. W., Ash, J. L., Bojanova, D. P., ... & Zhuang, G. (2020). Expedition 385 Preliminary Report: Guaymas Basin Tectonics and Biosphere. IODP Preliminary Report. https://doi.org/10.14379/iodp.pr.385.2020.

Umhoefer, P. J. (2011). Why did the Southern Gulf of California rupture so rapidly?—Oblique divergence across hot, weak lithosphere along a tectonically active margin. *Geological Society of America (GSA) Today, 21*(11), 4-10. https://doi.org/10.1130/G133A.1.

Umhoefer, P. J., Darin, M. H., Bennett, S.E., Skinner, L.A., Dorsey, R. J., & Oskin, M. E. (2018). Breaching of strike-slip faults and successive flooding of pull-apart basins to form the Gulf of California seaway from ca. 8–6 Ma. *Geology*, *46*(8), 695-698. https://doi.org/10.1130/G40242.1.

Umhoefer, P. J., Plattner, C., & Malservisi, R. (2020). Quantifying rates of "rifting while drifting" in the southern Gulf of California: The role of the southern Baja California microplate and its eastern boundary zone: *Lithosphere, 12*(1), 122–132. https://doi.org/10.1130/L1132.1.

van Wijk, J., Axen, G., & Abera, R. (2017). Initiation, evolution and extinction of pull-apart basins: Implications for opening of the Gulf of California. *Tectonophysics*, *719*, 37-50. https://doi.org/10.1016/j.tecto.2017.04.019.

Watts, A. B. (Ed.). (2009).Crust and Lithosphere Dynamics: Treatise on Geophysics. 614 University of Oxford, Oxford, UK, Elsevier, 44 pp.

Wang, Y., Forsyth, D. W., & Savage, B. (2009). Convective upwelling in the mantle beneath the Gulf of California. *Nature*, *462*(7272), 499-501. https://doi.org/10.1038/nature08552.

Wang, Y., Forsyth, D. W., Rau, C. J., Carriero, N., Schmandt, B., Gaherty, J. B., & Savage, B. (2013). Fossil slabs attached to unsubducted fragments of the Farallon

plate. *Proceedings of the National Academy of Sciences*, *110*(14), 5342-5346. https://doi.org/10.1073/pnas.1214880110.

Wernicke, B. (1981). Low-angle normal faults in the Basin and Range Province: nappe tectonics in an extending orogen. *Nature*, *291*(5817), 645-648. https://doi.org/10.1038/291645a0.

Wernicke, B., & Axen, G. J. (1988). On the role of isostasy in the evolution of normal fault systems. *Geology*, *16*(9), 848-851. https://doi.org/10.1130/0091-7613(1988)016%3C0848:OTROII%3E2.3.CO;2.

Widess, M. B. (1973). How thin is a thin bed?. Geophysics, 38(6), 1176-1180. https://doi.org/10.1190/1.1440403.

Wright, N. M., Seton, M., Williams, S. E., & Mueller, R. D. (2016). The Late Cretaceous to recent tectonic history of the Pacific Ocean basin. *Earth-Science Reviews*, *154*, 138-173. https://doi.org/10.1016/j.earscirev.2015.11.015.

Wu, J. E., McClay, K., Whitehouse, P., & Dooley, T. (2009), 4D analogue modelling of transtensional pull-apart basins: *Marine and Petroleum Geology, 26*(8), 1608–1623. https://doi.org/10.1016/j.marpetgeo.2008.06.007.

Yilmaz, Ö. (2001). Seismic data analysis: Processing, inversion, and interpretation of seismic data. Society of exploration geophysicists. https://doi.org/10.1190/1.9781560801580.

Yilmaz, O. 1987. Seismic data processing. Society of Exploration Geophysicists. Primera edición. Tulsa, Oklahoma. 526 p.

Zhao, D. (2004). Global tomographic images of mantle plumes and subducting slabs: insight into deep Earth dynamics. *Physics of the Earth and Planetary Interiors*, *146*(1-2), 3-34. https://doi.org/10.1016/j.pepi.2003.07.032.